

# A Stringent Upper Limit on Dark Matter Self-Interaction Cross Section from Cluster Strong Lensing

Kevin E. Andrade<sup>1</sup>★, Jackson Fuson<sup>1</sup>, Sophia Gad-Nasr<sup>1</sup>, Demao Kong<sup>1</sup>,  
Quinn Minor,<sup>2,3</sup> M. Grant Roberts<sup>1</sup> and Manoj Kaplinghat<sup>1</sup>

<sup>1</sup>University of California, Irvine, Irvine, CA 92697, USA

<sup>2</sup>Department of Science, Borough of Manhattan Community College, City University of New York, New York, NY 10007, USA

<sup>3</sup>Department of Astrophysics, American Museum of Natural History, New York, NY 10024, USA

1 April 2022

## ABSTRACT

We analyze strongly lensed images in 8 galaxy clusters to measure their dark matter density profiles in the radial region between 10 kpc and 100 kpc, and use this to constrain the self-interaction cross section of dark matter (DM) particles. We infer the mass profiles of the central DM halos, bright central galaxies, key member galaxies, and DM subhalos for the member galaxies for all 8 clusters using the QLens code. The inferred DM halo surface densities are fit to a self-interacting dark matter (SIDM) model, which allows us to constrain the self-interaction cross section. When our full method is applied to mock data generated from two clusters in the Illustris-TNG simulation, we find results consistent with no dark matter self-interactions as expected. For the eight observed clusters with maximum circular velocities in the range of 1400 to 2000 km/s, we find that the upper limit for the self-interaction cross section per unit mass of dark matter is  $0.065 \text{ cm}^2/\text{g}$  at the 95% confidence level.

**Key words:** dark matter – gravitational lensing: strong

## 1 INTRODUCTION

The currently-favored theory of the formation of galaxies in the Universe, dark energy plus cold dark matter or  $\Lambda$ CDM, is remarkably successful in explaining many of the observations of large-scale structures (Vogelsberger et al. 2014; Schaye et al. 2015). Dark-matter-only simulations show that structures form in a hierarchical manner, and result in dark matter (DM) halos that are well-approximated by a Navarro-Frenk-White (NFW) density profile (Navarro et al. 1996; Gao et al. 2012). Statistically significant departures from the NFW halo profile have been reported for galaxy clusters (Sand et al. 2008; Pontzen & Governato 2012; Martizzi et al. 2013; Newman et al. 2013a,b; Del Popolo 2012, 2014; Annunziatella et al. 2017), which provides a fertile ground for the exploration of DM physics. For galaxy clusters, there are a number of studies that point to the existence of DM cores in some galaxy clusters (Sand et al. 2008; Newman et al. 2013a,b; Del Popolo 2012, 2014; Annunziatella et al. 2017). One frequently proposed explanation for galaxy clusters with cores is that of Active Galactic Nuclei (AGN) feedback, where a black hole accreting gas can cause mass blowout and heating via gravitational interactions, leading to cores (Dubois et al. 2010; Teyssier et al. 2011; Ragone-Figueroa et al. 2012; Martizzi et al. 2012; Martizzi et al. 2013; Peirani et al. 2017).

In Martizzi et al. (2013), they show that AGN feedback can potentially cause cores in their simulated halo of mass  $1.42 \times 10^{13} M_{\odot}$ . On the other hand, Schaller et al. (2015) used the hydrodynamical EAGLE simulations of six galaxy clusters with  $m_{200} > 10^{14} M_{\odot}$ , which employ weaker AGN feedback, and found instead that feedback does not produce cores. Numerical cosmological simulations have advanced steadily in resolution and accuracy over the past two decades, but there is still no consensus about the presence of cores in large clusters of galaxies (Schaller et al. 2015; Martizzi et al. 2012; Martizzi et al. 2013).

Self-interacting dark matter (SIDM), in which DM has a nonzero self-interaction cross section, is another possible explanation for cored halos. SIDM has been discussed extensively in astro/particle physics literature as another possible model that can produce cores (Spergel & Steinhardt 2000; Randall et al. 2008; Vogelsberger et al. 2012; Rocha et al. 2013a; Kaplinghat et al. 2016; Ren et al. 2019, as key examples). The basic mechanism of core formation in SIDM is that self-interactions between DM particles in regions with high density cause the DM to thermalize, which results in the transfer of energy to the high density inner region of a halo, thus lowering the core density. One frequently employed measure of self-interaction strength is the scattering cross-section per unit mass,  $\sigma/m$ , although that does not account for the dependence of scattering cross-section on particle velocity. Constant cross-section SIDM models cannot simultaneously have apprecia-

★ E-mail: kandrad1@uci.edu

ble effects in dwarf galaxies, while being consistent with densities measured in clusters of galaxies (Zavala et al. 2013; Ren et al. 2019; Kaplinghat et al. 2016). A more complete model that accounts for the velocity-dependence of cross section is necessary because of the larger range of velocities probed in going from dwarf galaxies to clusters of galaxies (about 50 to 2000 km/s).

In this work, we analyze 8 observed galaxy clusters and two simulated clusters in three distinct analysis stages: (1) strong lensing, to determine DM and baryonic density profiles, (2) SIDM halo matching, to determine SIDM cross sections and relative particle speeds for each cluster, and (3) cross section upper limit modeling, to finally infer the upper limit on cross section. Our analysis pipeline is shown schematically in Figure 1. In the first stage we extend the strong lensing analysis of Andrade et al. (2019), in which one cluster (Abell 611) was examined, to include 8 relaxed clusters. The clusters we examine here are in the range of  $4 \times 10^{14} M_{\odot}$  to  $2 \times 10^{15} M_{\odot}$ . These are the among largest bound structures in the universe (Desai 2004). Their centers have dense concentrations of DM, and if such particles self-interact, cores with densities less than that predicted by  $\Lambda$ CDM could form. Our aim is to put a stronger constraint on the SIDM self-interaction cross-section by inferring the inner distribution of DM in these 8 clusters, using strong lensing alone. In cluster strong lensing, images typically appear near the Einstein radii of the clusters, which usually range from 20 to 100 kpc, well within the scale radii of the clusters (Richard et al. 2010). The DM density profile is constrained with highest accuracy near these image locations. This is also the region where SIDM thermalization would be expected to occur (Kaplinghat et al. 2016). Baryonic effects are also strong in this region, as the brightest cluster galaxy (BCG) is located there, with high baryonic mass. It is therefore important to accurately characterize the BCG's contribution to the total mass profile in the region of interest. We use photometry to measure cluster member characteristics such as radius, position, ellipticity, orientation angle and luminosity, but leave the stellar mass-to-light ratio as a parameter to be fit for each cluster.

Other techniques that could be employed to determine cluster DM profiles include weak lensing, x-ray temperature analysis and stellar kinematics (Miralda-Escude 1995; Natarajan & Kneib 1996; Sand et al. 2002; Kneib et al. 2003; Sand et al. 2004; Broadhurst et al. 2005; Mandelbaum et al. 2006; Okabe et al. 2010; Newman et al. 2011; Umetsu et al. 2011; Coe et al. 2012; Newman et al. 2013a,b). Strong lensing directly probes the profiles at the radii at which we are interested, while weak lensing and x-ray analysis probe much larger radii, where the ellipticity and profile may be significantly different than that of the inner region. Stellar kinematics of the BCG stars can help significantly in constraining the BCG mass and the slope of the dark matter density profile in the center (Newman et al. 2013b, as an example). This measurement depends on having the correct priors for radial variation of the stellar velocity dispersion anisotropy (Schaller et al. 2015) in spherical or axisymmetric Jeans analysis.

He et al. (2020) examined the ability of stellar kinematics, strong and weak lensing data sets to predict dark matter densities in the inner regions of simulated clusters, and found them to be accurate. This validates the approach undertaken by Newman et al. (2013a,b) in combining these three data sets to constrain the dark matter density profile of clusters. While adding other data sets is well motivated, it is of interest to ask what constraints are possible with just one data set given that biases may creep in because of the assumption of a common density profile with a fixed ellipticity that is inherent in a joint analysis. Somewhat surprisingly, we find that it is possible to infer strong constraints on the SIDM cross section

with just strong lensing data. In this paper, we develop the method to infer the SIDM cross section using strong lensing data, and leave the analysis including other data sets to future work. He et al. (2020) also discussed possible ways to reconcile the differences between the inferred dark matter density profile slopes in Newman et al. (2013b) and their simulated clusters in CDM cosmology, and highlighted a possible role for bias resulting from degeneracy with  $r_s$ , which is constrained in part by the weak lensing data. We will discuss the inference of  $r_s$  from strong lensing data, and argue that our results are consistent with expectations from simulations.

Armed with DM profiles and the aforementioned cluster member data, we employ a fitting process to match an NFW-like outer halo with an SIDM thermalized inner halo, following the process described in Kaplinghat et al. (2016). The resulting fit yields posterior chains for various parameters, including those for cross section per unit mass and average particle speed, for each cluster. In the third analysis stage, we synthesize the results of the the prior stages into an overall distribution for SIDM cross section to obtain an upper limit on self-interaction cross section.

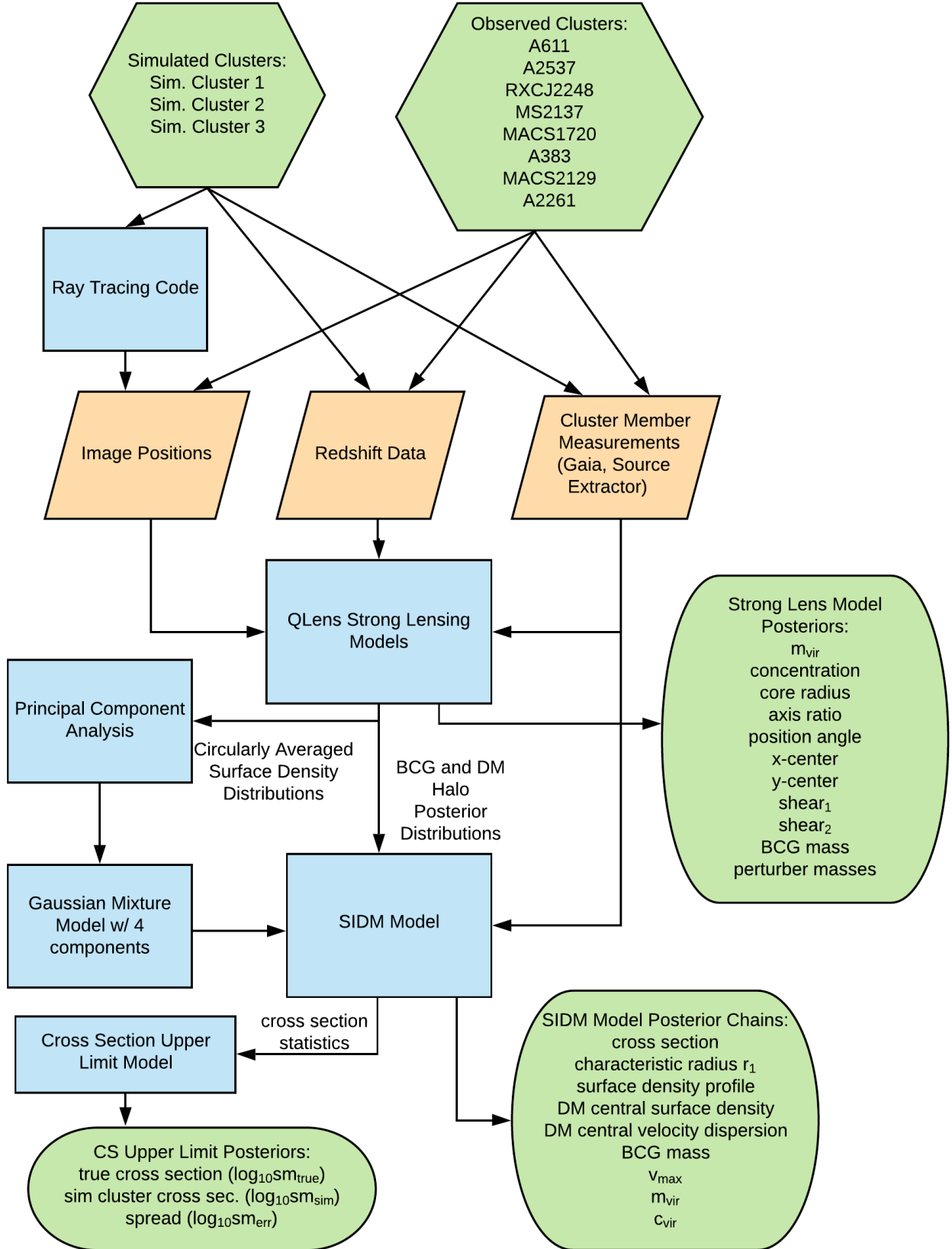
In this work we adopt a flat cosmology with  $\Omega_{\Lambda} = 0.7$ ,  $\Omega_m = 0.3$ , and  $H_0 = 70 \text{ km s}^{-1} \text{ Mpc}^{-1}$ . We define halo mass as  $M_{200}$ , the mass enclosed by a sphere of radius  $R_{200}$ , which we define in turn as the radius at which the halo density is 200 times the critical density of the universe at the redshift of the halo.

This paper is organized as follows. In Section 2, we describe our approach to the strong lens modeling analysis. In Section 3 we detail the strong lens models for the simulated clusters, and do the same for the observed clusters in Section 4. The results of the strong lensing models for the observed clusters are presented in Section 5. In Section 6 we describe our SIDM halo matching model and its results, and also describe the cross section upper limit model and its resulting inference of SIDM cross section. We summarize our findings in Section 7.

## 2 STRONG LENS MODELING METHODS

Our first step is to use strong lens modeling to determine the surface density profiles for a sample of galaxy clusters. For the cluster lensing models, we use previously reduced data in the form of (1) coordinates for multiple images and (2) source redshift data. The availability of multiple image coordinate data was a requirement for all the clusters in our sample. The positional error is assumed to be  $0''.5$  in each dimension. We construct mass models of the important features of each cluster: the (potentially cored) DM halo, BCG, important member galaxies ("perturbers"), and the DM subhalos associated with the perturbers. Many lensing analyses do not disentangle the DM subhalos from the luminous part, but doing so allows us to model the perturbers in a manner that is more consistent with cosmological simulations. The obvious challenge for creating accurate mass models is that the majority of the mass is in the form of invisible dark matter, the distribution of which must be inferred indirectly via lensing or by assuming some correlation with the luminous matter. We have designed a systematic approach that we first test on simulated galaxy clusters from the Illustris TNG simulation (Nelson et al. 2018; Springel et al. 2018; Pillepich et al. 2017; Nelson et al. 2017; Naiman et al. 2018; Marinacci et al. 2018) as described in section 3 of this work, allowing us to verify the accuracy of the models in reproducing cluster properties. We then apply this approach to actual galaxy clusters as described in section 4. For each cluster, we obtain a Markov Chain Monte Carlo (MCMC) chain for the model parameters, from which we can estimate param-

**Figure 1.** Schematic diagram of the analysis pipeline. Data sources are at the top. The final results are the parameter posteriors shown at the bottom.



eter posteriors and also infer posterior distribution in other derived parameters. We use the `MultiNest` sampler to create the MCMC chain (Feroz et al. 2009).

In brief, we construct mass models for clusters in the following way.

- Starting with a CCD image of the cluster (or a simulated image in the case of Illustris clusters), the coordinates, shapes and fluxes of the BCG and key member galaxies are measured, using one or both of the Starlink Gaia software package (Currie et al. 2014) or a proprietary 2D fitting code. A coordinate system is created with its origin at the center of the BCG.
- The main DM halo is modeled using a cNFW profile, the parameters of which are mass, scale radius, core radius, position angle, axis ratio, and (x, y) center offset coordinates. All are allowed to vary within ranges defined by wide, uninformative priors.
- The stellar baryonic component of selected significant member galaxies (referred to as “perturbors”) and the BCG are modeled using dPIE profiles. The mass parameter of each is allowed to vary (with perturbors typically tied together via a mass-follows-light scaling relation), while the scale radius, center coordinates, position angle and axis ratio are fixed by photometric measurement.
- For the perturbors, each is given an isothermal DM subhalo with a mass related to their baryonic mass via a power law. The scale radii of these DM subhalos are determined by their mass according to another power law, both described in Section 2.5. The center coordinates used are the same as those of the underlying baryonic model.
- To account for the effects of other masses along the line of sight that are not specifically included in the model, external shear is modeled, requiring two additional varying parameters,  $\gamma_1$  and  $\gamma_2$  (for a derivation of these, see Voigt & Bridle (2010)).

## 2.1 Lens Profiles

Our goal in this analysis is to construct mass models of galaxy clusters that accurately infer the surface density profile in the inner  $\sim 200$  kpc, and subsequently infer SIDM properties. To model the point images and infer the halo density profile, we use the `QLens` software package, as in Andrade et al. (2019).<sup>1</sup>

We employ the cored NFW lens profile (cNFW) as the primary model for the cluster halos. The spherically symmetric form for the cNFW density profile is defined as:

$$\rho = \frac{\rho_s r_s^3}{(r_c + r)(r_s + r)^2}. \quad (1)$$

This profile reduces to the canonical NFW form for  $r \gg r_c$ . Other authors have used this profile to fit cored DM halos in both hydrodynamical simulations (Peñarrubia et al. 2012) and actual cluster lenses (Newman et al. 2013a,b; Andrade et al. 2019). Analytic formulas for the projected density profile and deflection of the corresponding spherical model are given in Appendix A.

The BCG and member galaxy baryonic components, as well as galaxy member DM subhalos are modeled with a dual pseudo-isothermal ellipsoid (dPIE) profile (Elíasdóttir et al. 2007), also known as a “Pseudo-Jaffe” profile. The spherical version of this

profile is

$$\rho = \frac{\rho_{\text{cut}} r_{\text{cut}}^4}{(r^2 + r_{\text{core}}^2)^2 (r^2 + r_{\text{cut}}^2)^2}, \quad (2)$$

where  $\rho_{\text{cut}}$  is the density at the scale radius,  $r_{\text{cut}}$  is the scale (or tidal break) radius, and  $r_{\text{core}}$  is the core radius.

We model elliptical lens profiles by making the replacement  $R^2 \rightarrow qx^2 + y^2/q$  in the projected density profiles. The deflection and Hessian of the lens mapping must be calculated by numerical integration (see Schramm 1990; Keeton 2001), which can be computationally expensive. However, by using Gauss-Patterson quadrature for integration (Davis & Rabinowitz 2007), `QLens` is able to compute such integrals in a reasonable time. This approach avoids using the pseudo-elliptical approximation, in which the lensing *potential* is assumed to be elliptical rather than the mass profile. Using the pseudo-elliptical approximation can lead to inaccurate inferences of the density profile in cases of high ellipticity (e.g.,  $q < 0.5$ , see Andrade et al. (2019)).

## 2.2 Photometric Measurement

We use the Starlink Gaia software package (Currie et al. 2014), and the integrated version of Source Extractor (Bertin & Arnouts 1996) to measure the key photometric properties of the BCG and perturbors in each cluster: the coordinates, flux, axis ratio and position angle. We first select the HST image from the available object images that gives a target rest-frame wavelength in center of the visual band, based on the redshift of the lens. For background modeling, we use mesh-based RMS background detection. The projected half-light radii are measured using Source Extractor’s “flux radius” feature by setting the flux fraction to 0.5. Fluxes are converted to magnitudes, and then corrected for galactic extinction using the tool at <https://ned.ipac.caltech.edu>.

## 2.3 Central DM Halo

The main DM halo is modeled using a cNFW profile, the parameters of which are mass, concentration, core radius, position angle, axis ratio, and (x, y) center offset coordinates. Flat log-priors were used on the mass and core radius parameters, while flat priors were used on position angle, axis ratio and center offset.

Merten et al. (2015) studied the mass-concentration relation for cluster halos in 19 X-ray clusters from the CLASH sample. They observed an average concentration of 3.7, with a standard deviation of 0.65, and a negative correlation of concentration with halo mass. Since several of the clusters in this work are CLASH clusters, we might expect concentration to be in a similar range. However, we note that there are inherent biases in modeling concentration in strong lensing clusters, as outlined in Appendix C. Also, Fielder et al. (2020) found that concentration will be higher for a DM halo when its associated subhalos are excluded from the calculation. Therefore we opt for a weak Gaussian prior on concentration, with a mean of 6.0 and standard deviation of 1.5. Thus the  $2\sigma$  range is from 3.0 to 9.0, accommodating these anticipated biases if present.

## 2.4 BCG and Luminous Contribution of Member Galaxies

The BCG and perturbors for each cluster were modeled with a dPIE profile, with mass as a free parameter and other parameters set by observed photometry. The core radii of galaxies ( $r_{\text{core}}$ ) in the

<sup>1</sup> For more information on `QLens` contact Quinn Minor: qminor@bmcc.cuny.edu.



observed clusters are difficult to measure with high certainty. For our purposes, we are not particularly interested in the core sizes of the member galaxies, as structure at that scale will not have a significant impact on our results. Other authors have assumed a constant core radius for cluster member galaxies, typically in the range of 100 pc to 300 pc (Limousin et al. 2007a,b), or alternatively 0.1'' (Limousin et al. 2004), which for our clusters is approximately 300 pc to 600 pc. We adopt a core radius of 300 pc in each member galaxy in our observed clusters. For the Illustris clusters, we fit their two dimensional shapes from the simulated image to a dPIE profile, and use those parameters in our QLens model. The measured core radii range from 0 kpc to 2.3 kpc.

We tie together the masses of most of the perturbers in a given cluster and employ a mass-follows-light approach for scaling them. This is a reasonable approach, given that we have separate mass models for the DM subhalos. The perturber masses scale with the observed luminosity of each perturber, resulting in one free mass parameter describing the set of perturbers. One perturber is selected as the anchor, and the others are tied to it. We do this in order to limit the proliferation of model parameters. However, there are some perturbers that are quite close to images and that strongly affect them, in some cases even causing splitting of images into multiple images. For these perturbers, their mass is allowed to vary separately from the group, at the cost of including another degree of freedom in the model.

## 2.5 DM Subhalos

In many strong lensing analyses, the baryonic and dark components of perturbers are modeled as one object, often based solely upon the photometry of the stellar component. This has potential for bias, since the DM component is likely to be strongly dominant in both mass and size. To guard against this, we model the DM subhalos of each perturbing galaxy.

Infalling galaxies and their DM halos will be partially stripped of their DM by tidal forces due to the massive cluster. To quantify this for the simulated clusters, we looked directly at the stellar-mass to halo-mass (SMHM) relation in Illustris TNG. We selected all subhalos within a 400 kpc radius of the center of the host halos, and with a stellar mass range similar to those of perturbers in the real cluster sample, i.e., between  $1 \times 10^{10} M_{\odot}$  and  $5 \times 10^{12} M_{\odot}$ . These are well fit by a power relation of the form

$$M_{\text{halo}} = k M_{*}^{\alpha}, \quad (3)$$

with  $k = 1.115$  and  $\alpha = 1.024$ . We used this relation to generate DM subhalo masses in the models of the simulated clusters.

For the observed clusters, we turned to Niemiec et al. (2017), where they examine the stellar mass-halo mass relation for cluster galaxies. We fit a power law to their data (see Figure B1 in Appendix B). The resulting power law (in the same form as Equation 3) gives  $k = 1.157$  and  $\alpha = 1.1171$ , which is similar to that found for Illustris. As can be seen by the error bars in the figure, this relation has significant uncertainty in the lower bound. We therefore use it as an upper bound only, and explore departures from this upper bound by trying normalizations at 100%, 50%, 25% and 12.5% of the parameter  $k$ , as noted in the individual cluster models.

We modeled the dark matter profile of cluster galaxies with a dPIE profile with the core radius set to zero. We set the half-mass radius of the dPIE profile equal to that of a NFW density profile with the median concentration in Diemer & Joyce (2019), as implemented in Colossus package (Diemer 2018). Neglecting the mild redshift dependence in the concentration mass-relation for

the relevant lens redshift range (about 0.2 to 0.6), we obtain the half-mass radius  $= 0.0019 M_{\text{halo}}^{0.37}$ .

We find that in Illustris TNG, the position angles of dark matter halos of cluster galaxies are usually quite similar to that of the associated stellar mass, but the dark matter halos are rounder on average.

We fix the position angle to be the same as that of the stellar spheroid and choose an axis ratio for the DM subhalos equal to  $\sqrt{q_{*}}$ , i.e., the geometric mean between the stellar axis ratio and unity. We ran tests on the effect of this assumption, comparing it to using  $q = q_{*}$  and  $q = 1$  for three representative clusters, A611, A2537 and MACS2129. The impact on the inferred BCG mass and halo mass was well within one standard deviation for all three clusters.

## 2.6 Use of Spectroscopic Redshift Data

The data for each model is in the form of multiple image point locations, together with the redshift of each. Both spectroscopic and photometric redshift data are used, as noted in for each individual cluster. Where photometric data with significant confidence intervals was used, we adopted a redshift  $z_a$  for each source that minimized  $\chi^2 = \sum_{i=1}^n \frac{(z_i - z_a)^2}{\sigma_i^2}$ ,

where  $n$  is the number of images in the image group,  $z_i$  is the quoted median redshift of the image and  $\sigma_i$  is the 68% uncertainty interval for the measured redshift. In the case that the error in redshift is not given as a single value but in the form  $z_{-}^{\text{hi}} \sigma_{\text{low}}$ , we use  $\sigma_{\text{hi}}$  as the error when the trial value is above the median and  $\sigma_{\text{low}}$  when it is below.

## 2.7 Use of Central Images

Gravitationally lensed objects can produce positive-parity "central" images that are typically demagnified and near the center of the lens, and as a result are often obscured by bright objects in the central region of the field. When they are visible, they are helpful in constraining the lens parameters. Central images occur in five of the eight clusters in our sample: A2537, RXCJ2248, MS2137, A2261 and MACS1720. The QLens software can be configured to look for central images and produce model central images for a given cluster, but the setting is the same for all sources in the cluster, even if only one source has a central image. As a result, for the five clusters with central images, our models produce some images in the central region that do not have a corresponding "observed" match in the data. These predicted images might be present but difficult to observe due to their inherently low magnification and/or proximity to the bright objects usually present in the center of clusters.

## 3 MODELS OF SIMULATED CLUSTERS

To test the validity of our methods, we use data from the IllustrisTNG simulation (Nelson et al. 2018; Springel et al. 2018; Pillepich et al. 2017; Nelson et al. 2017; Naiman et al. 2018; Marinacci et al. 2018) to simulate strong lensing in three massive TNG galaxy clusters. Their characteristics are summarized in Table 1.

### 3.1 Selection of Simulated Cluster Halos

To find analogues of our real cluster sample, we used the largest volume simulation available at a box length of 300 Mpc, in the highest resolution for that suite of simulations, TNG300-1. While

**Figure 2.** Image plane plots for each cluster showing the data image positions (red) and modeling image positions (cyan). The points appear purple where they overlap. Critical curves are shown for a source redshift of 2.0. Redshift values for each family of points are indicated in the box to the right of each plot. North is up, East is to the left. Axes scales are in arc seconds.

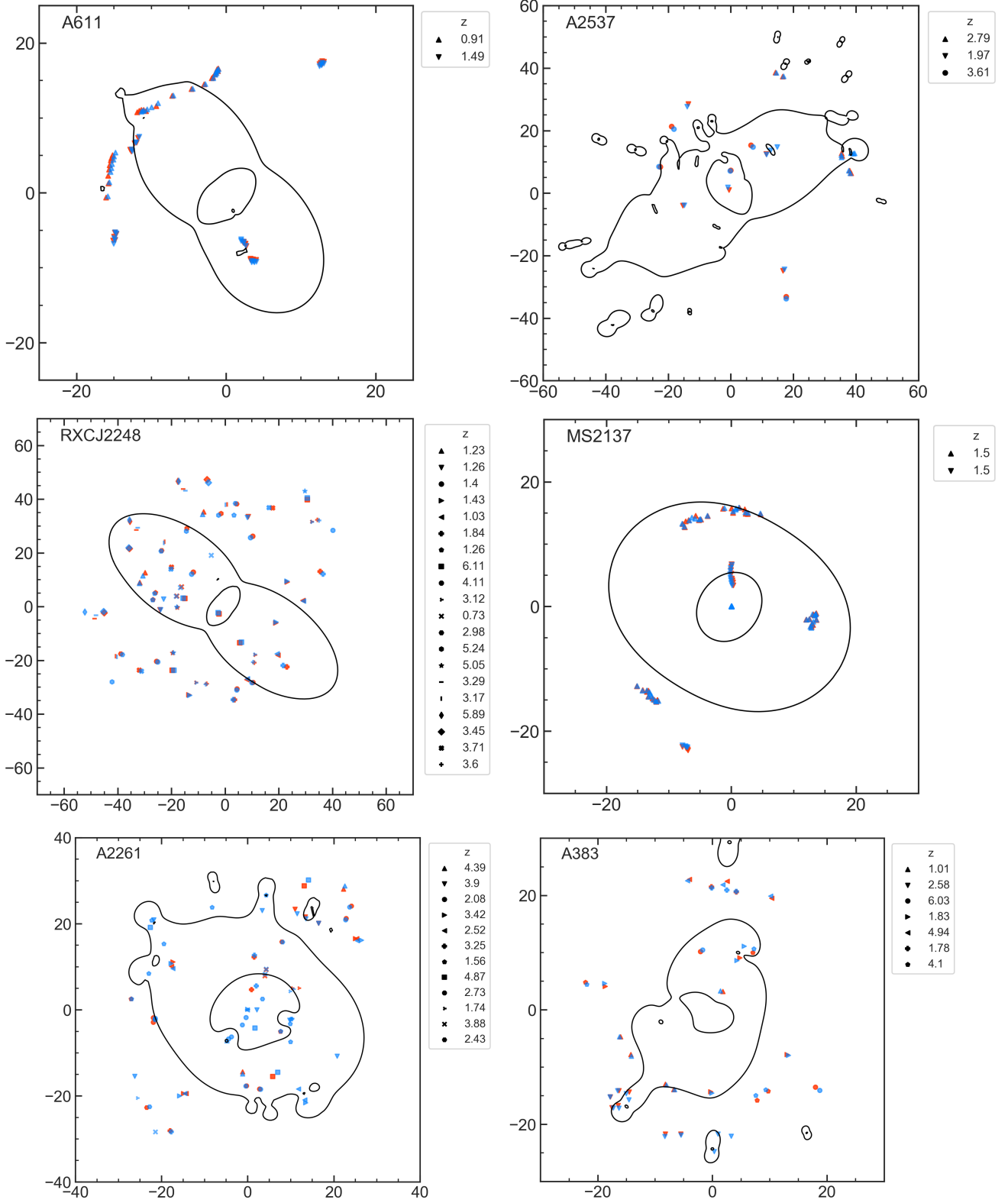
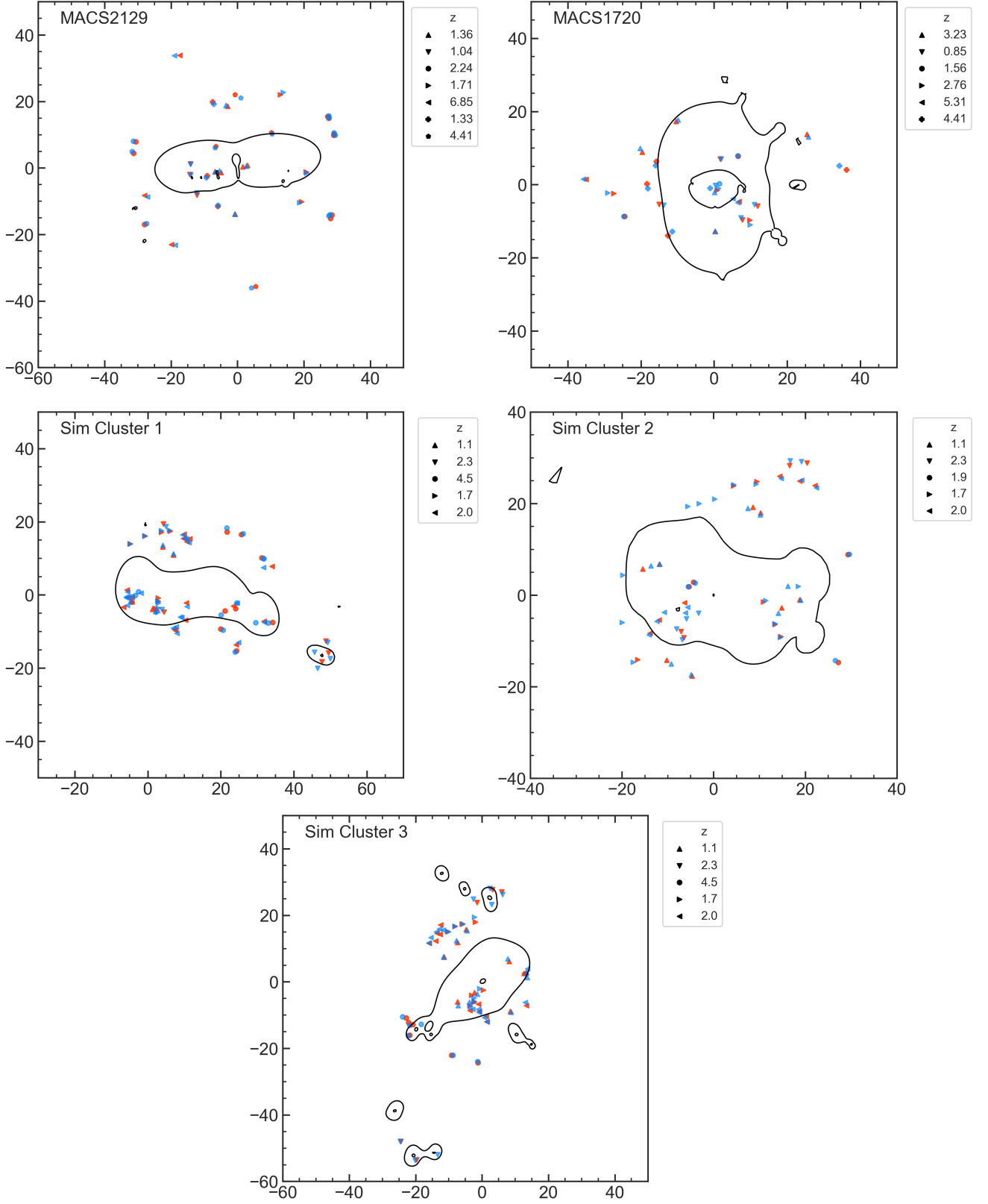


Figure 2., continued.



**Table 1.** Key cluster halo parameters of simulated lensing clusters from Illustris and fitted values from strong lensing models. All simulated clusters were given a redshift of 0.3. The Illustris parameters are from 3D fits using Colossus. We were not able to obtain a meaningful strong lensing fit with Cluster 1 due to its unrelaxed nature. The strong lensing fit  $m_{200}$  and concentration values are for the main DM halo only and do not include that in subhalos. RMS position error is for the x and y coordinates, combined in quadrature.

Cluster Name	Relaxed?	Illustris 3D Fit			Strong Lensing Fit				RMS Position Error (arc sec)
		ID	$m_{200}$ ( $10^{14} M_{\odot}$ )	Concentration	$m_{200}$ ( $10^{14} M_{\odot}$ )	Concentration	Image Points	Source Points	
Cluster 1	no	5941	8.13	4.49	N/A	N/A	42	16	1.01
Cluster 2	yes	10359	5.25	7.21	$4.41^{+1.20}_{-0.83}$	$8.52^{+1.02}_{-0.95}$	28	12	0.82
Cluster 3	yes	19512	3.39	6.80	$4.79^{+0.87}_{-0.69}$	$7.83^{+0.91}_{-0.83}$	41	16	0.89

the large box size comes at the expense of resolution for dark matter particle mass ( $5.9 \times 10^8 M_{\odot}$ ), the TNG300-1 suite are the ideal choice among the TNG simulations for studying large scales. We used the gravo-magnetohydrodynamical suite of simulations which includes baryons, to account for the effects of baryonic matter on the DM in these halos.

To match the general range of redshifts in our real cluster sample, we selected three of the most massive host halos as our simulated clusters from the TNG300-1 snapshot corresponding to a redshift of  $z = 0.3$ . All three clusters have masses  $10^{14} M_{\odot} < m_{200} < 10^{15} M_{\odot}$ . For each, the bright galaxy at the center of the potential in the central subhalo was identified as the BCG. Of the three simulated clusters, two appear relaxed and have a clearly dominant BCG, while one (Sim. Cluster 1) appears to be merging, as evidenced by a second major galaxy nearly comparable in size to the BCG and located only  $\sim 120$  kpc away from it. We chose to keep this cluster in our analysis to examine its impact on our inferences. The remaining two hosts have only one BCG.

Cluster strong lensing is subject to selection bias dependent upon the line of sight (LOS), because mass concentrations along specific LOS can increase the surface density and lensing strength for subhalos that depart from spherical symmetry (Sereno et al. 2015, and see also Appendix C for a discussion of concentration bias). To simulate this effect and to ensure strong lensing occurs, we shot 10 random lines of sight through each halo and used the LOS with largest central surface density. We then obtained 3D fits of each simulated halo, using the Colossus software package (Diemer 2018). The resulting fitted values for  $m_{200}$  and concentration, are listed in Table 1. Note that the LOS that produced the highest central surface density for a given cluster halo also yielded the highest concentration for that cluster halo, suggesting our simulated cluster analogs are affected by selection bias.

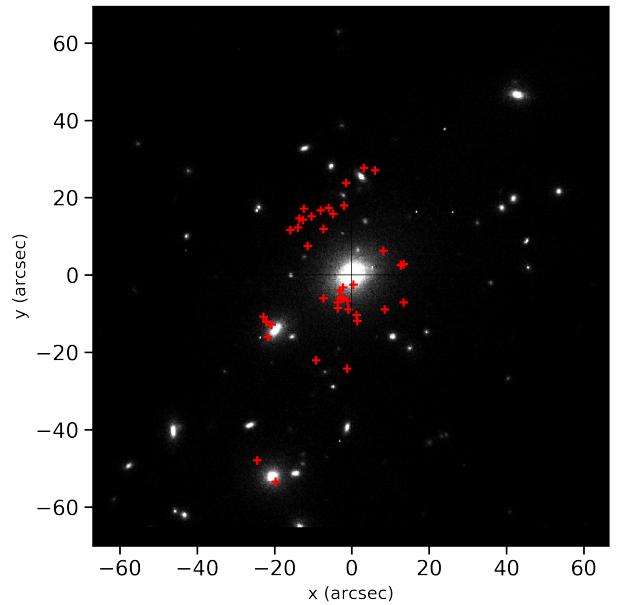
### 3.2 Simulated Image Production

After choosing the LOS, we then created a surface density map of the stars, gas, and DM, at a resolution of 1.25 kpc per pixel. From the surface density map we calculate the scaled lensing potential:

$$\psi(\vec{\theta}) = \frac{1}{\pi} \int d^2\theta' \kappa(\vec{\theta}') \ln |\vec{\theta} - \vec{\theta}'|, \quad (4)$$

where  $\psi$  is the scaled potential,  $\vec{\theta}$  is the deflection angle, and  $\kappa$  is the convergence. The reduced deflection angle  $\vec{\alpha}$  can be found by taking the gradient of the scaled potential, i.e.,  $\vec{\alpha} = \nabla_{\theta} \psi = D_L \vec{\nabla} \psi$ , where  $D_L$  is the distance from the observer to the lens. This, together with the lens equation  $\vec{\alpha} = \vec{\beta} - \vec{\theta}$ , allows us to solve for image positions for any given angular position  $\vec{\beta}$  of a source object.

**Figure 3.** An example image of a simulated cluster (Sim. Cluster 3). The BCG is centered, and the red markers indicate 41 simulated point images from 16 source points.



For each cluster, from 12 to 16 point sources were created, each generating 3 or 5 images, resulting in 28 to 41 images. There were 5 unique redshift groups for each cluster, ranging from  $z = 1.1$  to  $z = 4.5$ , which represent a typical range of source redshifts found in actual clusters. Random Gaussian errors with a standard deviation of  $0''.5$  were added to each x and y coordinate of the images, resulting in a mean position error of  $0''.71$ . An example of a mock image for Simulated Cluster 3 is shown in Figure 3.

### 3.3 Model Details for Simulated Clusters

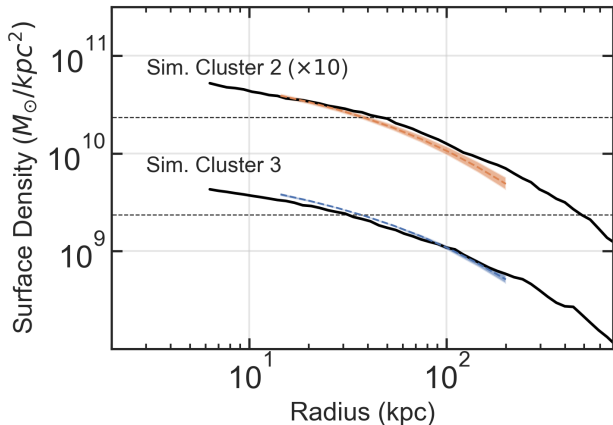
The models for each of the three simulated clusters are discussed below. Key model results are summarized in Table 1. Image plane plots are shown in Figure 2, showing data image locations, modeled image locations and critical curves.

#### 3.3.1 Cluster 1

Cluster 1 appears to be a merging cluster, with two large central galaxies separated by approximately 120 kpc. The unrelaxed DM profile proved problematic to model. The data set had 16 source



**Figure 4.** Plots of spherically averaged DM surface density of the cNFW main halo versus radius for the relaxed simulated clusters. Sim. Cluster 2 is offset by one decade for display purposes. The width of the colored band represents the 68% confidence interval. The dotted horizontal lines show the critical surface density for each cluster. The actual DM surface density is shown as a black line, which includes DM from the main halo and subhalos.



points and 42 images, and we identified 9 perturbers in addition to the two large central galaxies. We attempted several approaches; treating the smaller of the two central galaxies as an ordinary perturber did not work well, nor did using two blended cNFW halos. While we were able to reproduce many of the simulated images, there is not enough freedom in the model to accurately reproduce the DM distribution, which is crucial for accurate inference of SIDM cross section. The modeled images had a root-mean-square (RMS) position error of  $1''.01$  (x and y combined).

### 3.3.2 Cluster 2

Cluster 2 is a relaxed cluster, and the simulated data set had 12 source points and 28 images. From the created HST-like image, we determined the photometric parameters (luminosity, center coordinates, dPIE radii, position angles and axis ratios) of the BCG and perturbers. We identified 13 perturbing galaxies, choosing those  $\leq 60$  arcsec of the BCG and with a mass  $\geq 10^{10} M_{\odot}$ . All but one of the perturbers were "anchored" together so that their masses scaled as one group. We individually optimized one perturber that was close to several images. All data images were reproduced by the model, however there were 10 extra images. The modeled images had an RMS position error of  $0''.82$ . The surface density was reproduced with an mean accuracy of 0.05 dex over the radius range where images are located (i.e., from 23 kpc to 157 kpc from the BCG).

### 3.3.3 Cluster 3

Cluster 3 is a relaxed cluster with 16 source points and 41 images in the simulated data set. Using the created HST-like image, we reduced photometric measurements of perturbers and selected 10 perturbers, based on their proximity to the center and luminosity. Of these, 9 were anchored together so that their mass was varied as one, and one perturber was optimized individually. To achieve better fitting and image reproduction, we reduced the perturbers' DM halo mass normalization by 50%. All data images were reproduced by the model, with one extra magnified image. The RMS position error of the modeled images was  $0''.89$ . The surface density was reproduced

with an mean accuracy of 0.04 dex over the radius range where images are located (i.e., from 11 kpc to 254 kpc from the BCG).

## 3.4 Summary of Lessons from Simulated Clusters

We used ray tracing to simulate strongly lensed images for three Illustris clusters, and tested our strong lensing analysis pipeline on those clusters. Our key findings for those models are summarized here.

- We were able to successfully recover halo mass and BCG mass for the two relaxed clusters.
- We measured the size of the BCGs with a 2-D fitting code, assuming an elliptical dPIE model (see Section 2.1). The measured scale radii values were quite small and compact, with scale radii of 0.5 kpc and 2 kpc respectively for Sim. Clusters 2 and 3. We note that these values are much smaller than the half-light radii quoted in the Illustris catalog, 66 kpc and 76 kpc, respectively. This difference could be due to the extended light distribution in the cluster. As a check, we reran the strong lensing models using the larger BCG radii. In each case, there were modest differences in some parameter posteriors, but in all cases the preferred halo core size was very small, i.e., consistent with no core.
- The merging cluster, Sim. Cluster 1, proved difficult to model, as the mass distribution is complex and is not well characterized by a potentially cored NFW halo with additional perturbing bodies. We were not able to recover meaningful parameter values for that cluster. This highlights the importance of choosing clusters that are not major mergers for our analysis. We have been cognizant of this restriction in choosing the sample of observed clusters to model.
- We were able to reproduce the surface density profile for the relaxed clusters with very good accuracy. The model matched the actual profile within 0.05 dex over the range of radii from the position of the innermost image to that of the outermost image, as shown in Figure 4.
- Concentrations were biased high compared to the expected concentration for spherically-averaged halos in both the relaxed clusters. This would make sense if the LOS is preferentially oriented along the major axis of the cluster halos, as is expected in the observation of observed clusters; see Appendix C for more discussion. Another plausible contributing factor is that the concentration will be higher for a DM halo when mass from its associated subhalos are excluded, as discussed in Fielder et al. (2020). This is at least partially true in our models, as we model the subhalos of the largest perturbers individually.
- Extra modeled images appeared in the relaxed cluster models, ten in the case of Sim. Cluster 2 and one in the case of Sim. Cluster 3. However this did not appear to impact the accuracy of the surface density reproduction or the parameter inference.

## 4 MODELS OF OBSERVED CLUSTERS

We began by selecting a subset of galaxy clusters, based on the following criteria:

- a generally relaxed shape, with a dominant main halo and the absence of vigorous current merger activity, based on either X-ray or optical observation;
- the presence of strong lensing, resulting in several multiple-image systems
- existing multiple image data, including redshifts,

(iv) ideally, the availability of galaxy member data, to determine likely lensing perturbers, although in many cases we reduced our own perturber information from HST data.

We targeted a sample size of approximately 8 to 10 halos, so as to enable us to draw cogent general conclusions from the sample. The resulting sample set of 8 clusters is listed in Table 2.

Figure 2 shows plots of the image plane for the cluster models, showing the data image positions, their modeled counterparts, and representative critical curves for a redshift of 2.0.

#### 4.1 Abell 611

In [Andrade et al. \(2019\)](#) this cluster was modeled in detail, using image position and galaxy member data from [Donnarumma et al. \(2011\)](#), but with redshift corrections indicated in [Newman et al. \(2013a\)](#); [Belli et al. \(2013\)](#). The redshift data is spectroscopic. In [Andrade et al. \(2019\)](#), both cNFW and Corecusp halo models were explored, which gave similar results, with the cNFW model being the preferred model.

In this work, our approach is similar, except that we model DM halos for each of the perturbers, as described in Section 2.5. The BCG, the seven perturbing galaxy members and their associated DM halos were modeled with dPIE profiles. The BCG mass parameter was a varied parameter, while the other BCG parameters were fixed based on the photometry from [Newman et al. \(2013a\)](#). The mass parameters for the perturbing members were varied in three groups, one each for perturbers 1 and 2, and one group for perturbers 3 through 7. The normalization of the stellar-halo mass relation (i.e., parameter "k" in Equation 3) was reduced by 75%, to allow for the lowest  $\chi^2$  while still matching all data and model images. The resulting model reproduced all data images, with no extra images.

#### 4.2 Abell 2537

Abell 2537 is an efficient gravitational lens that has been studied by several others, including [Newman et al. \(2013a,b\)](#); [Cerny et al. \(2018\)](#). It appears relaxed and uniform in X-ray images ([Schmidt & Allen 2007](#)). [Newman et al. \(2013a\)](#) describes the cluster as likely disturbed, perhaps along the line-of-sight, but we nevertheless were able to construct a satisfactory model that explains the image positions with reasonably good fidelity. The stellar-halo mass normalization "k" was reduced to 12.5% of its nominal value, to minimize the image position  $\chi^2$ .

Image positions, spectroscopic redshift and BCG photometry data from [Newman et al. \(2013a\)](#) were used in the model. Perturbing galaxy data from [Cerny et al. \(2018\)](#) was also utilized. Only those perturbers with V-band luminosity greater than  $5 \times 10^{10} L_{\odot}$  and located less than  $60''$  from the BCG were included in the model, resulting in 32 perturbers. The BCG mass and one anchor galaxy mass (to which the other 31 perturbers are anchored) were varied parameters. There were three extra images in the model with  $|\text{magnification}| > 1$ . Those images are in the vicinity of a bright perturbers and could be present but washed out in the perturber light.

#### 4.3 RXC J2248.7-4431

Also known as Abell 1063S, this cluster has been previously modeled in some detail by [Caminha et al. \(2016\)](#) and [Bonamigo et al. \(2018\)](#). It appears relaxed and uniform in X-ray images ([Schmidt & Allen 2007](#)). We used data from [Bonamigo et al. \(2018\)](#) for the image positions, redshifts and perturbers. We included only those

perturbers with V-band luminosity greater than  $2 \times 10^{10} L_{\odot}$  and a distance from the BCG less than  $60''$ , resulting in 13 perturbers. The mass of the BCG and one anchor galaxy (to which the other 12 perturbers were anchored) were varied. The best-fit models for this cluster produced 7 extra images with  $|\text{magnification}|$  exceeding 1.0. Examination of the HST image ([Postman et al. 2012](#)) revealed what may be image candidates at most of the predicted locations, but without spectroscopic data we cannot confirm them.

#### 4.4 MS 2137.3-2353

MS2137 appears very relaxed and uniform in X-ray images ([Schmidt & Allen 2007](#)). We adopt the image positions and redshift data from [Donnarumma et al. \(2009\)](#). The point image locations follow two great arcs at nearly identical spectroscopic redshifts. BCG photometry from [Newman et al. \(2013a\)](#) was used. There is one prominent perturber, the position and photometry data of which we reduced using HST data ([Postman et al. 2012](#)). The mass of the BCG and perturber were allowed to vary, while the other parameters were fixed, based on photometric measurements. The stellar-halo mass normalization parameter "k" was reduced by 50% to achieve better fitting and image reproduction. All data images were reproduced, with no extras.

#### 4.5 Abell 383

Abell 383 is a relaxed cluster with 9 lensed sources for a total of 27 images. Following [Monna et al. \(2015\)](#), we also adopt 19 perturbers for this cluster. For the BCG and all other cluster members, the photometric parameters were reduced from the HST F814W filter ([Postman et al. 2012](#)) using SourceExtractor provided in the Gaia software package. As in [Monna et al. \(2015\)](#) we use the GR galaxy as our reference galaxy and anchor all other perturber masses to the GR galaxy for optimization. Due to localized radial arcs near the G1 and G2 perturbers, we individually optimize these perturbers in addition to the BCG and GR. The stellar-halo mass normalization "k" was reduced to 25% of its nominal value, to minimize the image position  $\chi^2$ . The model reproduced all data images but yielded 6 extra images with  $|\text{magnification}| > 1$ . Examination of the HST image for potential new images at their predicted locations was inconclusive due to noise in the image.

#### 4.6 Abell 2261

Abell 2261 is a borderline relaxed cluster with 12 strongly lensed sources for a total 30 images (see Table 3 of [Coe et al. \(2012\)](#)). Our search of past work on this cluster did not yield data on potential perturber membership in the cluster. We therefore adopted 12 perturbers by choosing the galaxies which distort critical curves in Figure 1 of [Coe et al. \(2012\)](#). We measured effective radius, axis ratio, luminosity and position angle from the HST F775W filter ([Postman et al. 2012](#)) using SourceExtractor provided in the Gaia software package for the BCG and perturbers. We individually optimized 4 perturbers which are located in close proximity to images; the others were grouped and optimized as one. The stellar-halo mass normalization "k" was reduced to 50% of its nominal value, to minimize the image position  $\chi^2$ . The model was able to match all data images with an RMS position error of  $0''.83$ , however 8 extra non-central images with  $|\text{magnification}| > 1$  were produced.

**Table 2.** Summary of the observed cluster sample.

Cluster Name	Adopted Redshift	kpc per arcsec	$t_{\text{age}}$ (Gyr)	Relaxed?	Image and Galaxy Data Sources	Image Points	Source Points
Abell 611	0.288	4.33	10.2	yes	Donnarumma et al. (2011); Newman et al. (2011)	49	13
Abell 2537	0.294	4.39	10.1	yes*	Newman et al. (2013a); Cerny et al. (2018); this work	16	4
RXC J2248.7-4431	0.348	4.92	9.7	yes	Bonamigo et al. (2018); this work	55	20
MS 2137.3-2353	0.314	4.60	9.9	yes	Donnarumma et al. (2009); Newman et al. (2013a); this work	50	14
Abell 383	0.189	3.16	11.1	yes	Monna et al. (2015); this work	27	9
Abell 2261	0.225	3.61	10.8	yes*	Coe et al. (2012); this work	30	12
MACS 2129.4-0741	0.589	6.63	7.8	yes*	Monna et al. (2017); this work	31	9*
MACS 1720.3+3536	0.387	5.27	9.3	yes	Zitrin et al. (2013); this work	19	6

\* but see discussion in the relevant paragraph of Section 4

#### 4.7 MACS 2129.4-0741

MACS2129 is described by Mann & Ebeling (2012) as a recent but well separated merger, although it appears relaxed. It has 8 lensed sources and a total of 31 images according to Monna et al. (2017) (see Table 3 there). However, system 4 is much better characterized as a system of two images being lensed rather than one image being lensed, thus we use 9 sources as in Monna et al. (2017), where they also make a distinction between the two images in system 4. We adopt 10 perturbing galaxies, two of which are clear strong lensing sources that impact image positions significantly. The masses of those two were optimized individually. The masses of the other perturbers were anchored to a reference galaxy, the mass of which was varied and optimized. The stellar-halo mass normalization "k" was reduced to 12.5% of its nominal value, to minimize the image position  $\chi^2$ . The model reproduced 30 out of 31 data images, with no extra images. The model matched data images with an RMS position error of  $0''.79$ . The radii, position angle, and axis ratio of all cluster members were measured from the HST F814W filter (Ebeling et al. 2007).

#### 4.8 MACS 1720.3+3536

MACS1720 also appears relaxed and uniform in X-ray images (Schmidt & Allen 2007). We use the image position and photometric redshift data of Zitrin et al. (2015). A single redshift value for each image group was selected by the photo-z optimization process described in Section 2.6. Image set 7 from Zitrin et al. (2015), a 3-image set in the far southern part of the image, was problematic to model. It contains a pair of images within close proximity to one another, but no apparent perturbing bodies nearby. In addition, the photometric redshift of this source has a high uncertainty. We therefore excluded that source point. Interestingly, we were able to accurately produce the three images in Image set 7 if we included a perturbing subhalo of mass  $\sim 2 \times 10^{12} M_{\odot}$  at coordinates of (12.5, -25.5) arcsec relative to the BCG. However, inspection of the HST images does not reveal any significant luminous body at that location.

BCG photometry and perturber data were reduced from HST images (Postman et al. 2012). We included only those perturbers with F814W luminosity greater than  $5 \times 10^9 L_{\odot}$  and a distance from the BCG less than  $30''$ , resulting in 13 perturbers. The masses of these 13 were varied as a group. The resulting model had one extra image with |magnification|  $> 1.0$ , a magnification 2.7 image located at (4.2, -3.5) arcsec relative to the BCG. Examination of the HST reveals a good candidate object near that location, although we cannot confirm it absent redshift measurement.

### 5 STRONG LENSING RESULTS

Using the methods described in Section 2, we constructed mass models for each cluster that reproduced the observed image positions. We used separate lens elements for the baryonic and dark mass components of member galaxies, which is not a common approach in cluster lensing analysis. The strong lensing models were able to reproduce the image position data with good accuracy. We assumed measurement error of  $0''.5$  in each of the x and y coordinates of the data image positions. The models recovered the data image positions with root-mean-square position errors (combining the x and y components) ranging from  $0''.32$  to  $1''.07$ , with a median of  $0''.66$ , as shown in Table 3. The reduced image plane  $\chi^2$  for the fits ranged from 0.36 to 5.79. All data images were reproduced except one. Occasionally, extra images were produced by the models, as noted in the relevant paragraphs of Section 4.

Strong lensing parameter inferences are summarized in Table 3. Figure 5 shows histograms for the 2-dimensional BCG offset, mass-to-light ratio, and Core Radius. Below we discuss the parameter inferences for each cluster for these key parameters: DM halo mass (i.e.,  $m_{200}$ ), BCG mass, and core radius ( $r_c$ ).

#### 5.1 Abell 611

Our inference of the mass of the central DM halo is  $8.77^{+3.34}_{-2.30} \times 10^{14} M_{\odot}$ . In Newman et al. (2009) they infer a value of  $6.2^{+0.7}_{-0.5} \times 10^{14} M_{\odot}$  using a combination of weak lensing, strong lensing and kinematic data and employing a generalized NFW profile. In a subsequent work, Newman et al. (2013a) found  $m_{200}$  of  $8.31^{+1.46}_{-1.23} \times 10^{14} M_{\odot}$  using weak and strong lensing. In Donnarumma et al. (2011) they use an NFW profile for the DM halo and infer strong lensing  $m_{200}$  values of  $4.68 \pm 0.31 \times 10^{14} M_{\odot}$  using a dPIE profile for the BCG, and  $6.32^{+0.51}_{-0.23} \times 10^{14} M_{\odot}$  using a Sersic profile for the BCG. They arrive at an  $m_{200}$  of  $9.32 \pm 1.39 \times 10^{14} M_{\odot}$  using X-ray gas temperature techniques. Our inference is consistent with all of these.

Our inferred BCG mass is  $1.21^{+2.74}_{-0.88} \times 10^{12} M_{\odot}$ . In Newman et al. (2009) they infer a BCG mass of  $1.01^{+0.24}_{-0.29} \times 10^{12} M_{\odot}$ , while in Donnarumma et al. (2009) they infer  $6.17^{+1.32}_{-1.79} \times 10^{12} M_{\odot}$  for their case 6, which is the most comparable to our configuration. Our inference falls in the middle, and is consistent with the Newman et al. (2009) result but in mild tension with the Donnarumma et al. (2009) result.

We infer a cNFW core radius of  $0.52^{+6.48}_{-0.48}$  kpc, which is consistent with the findings of Newman et al. (2013b), in which they infer a core size of  $2.95^{+4.29}_{-2.01}$  kpc.

**Figure 5.** Histograms for 2-dimensional BCG offset, BCG mass-to-light ratio and DM halo core radius posteriors. The histograms are normalized to unity area, and have been smoothed slightly with a Gaussian kernel for display purposes.

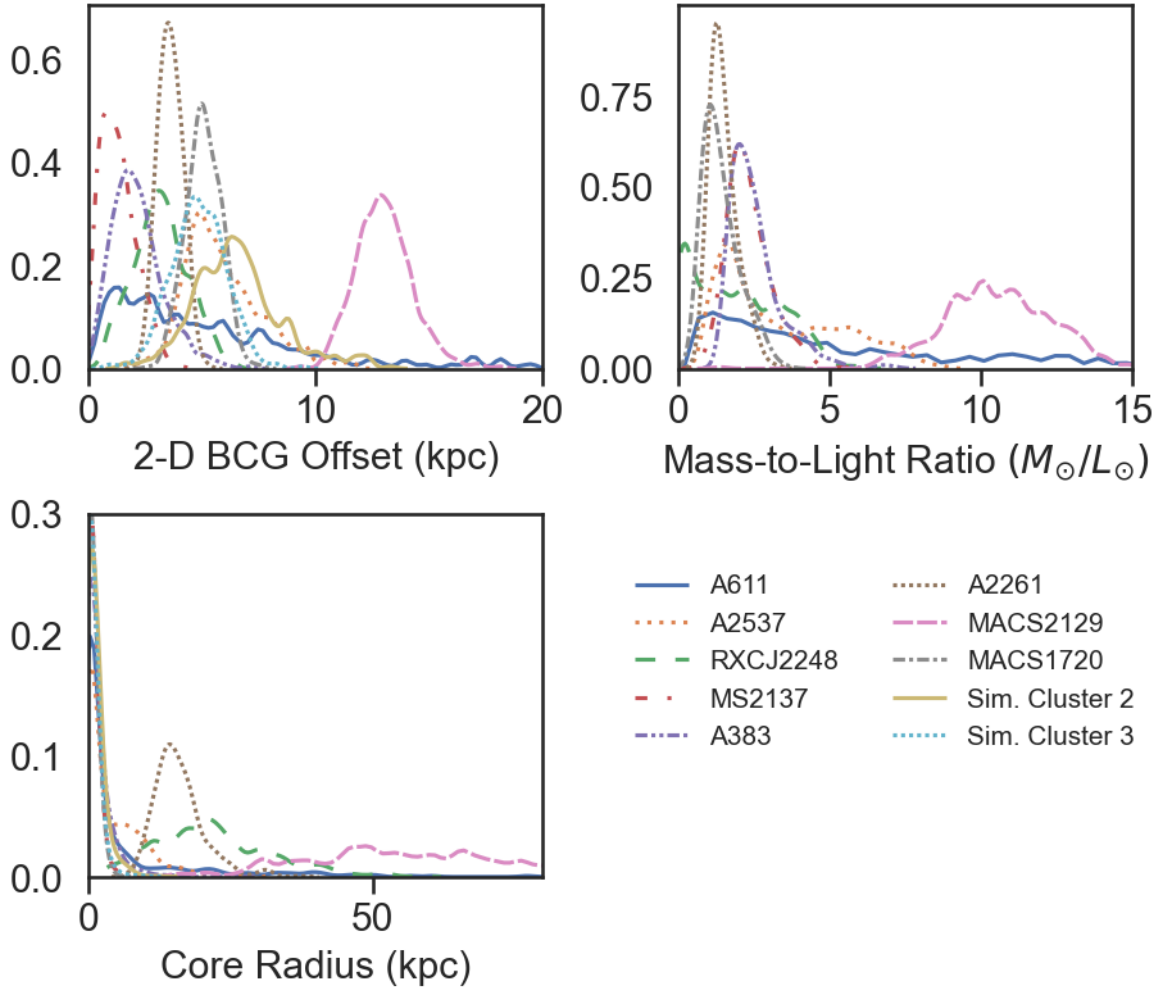
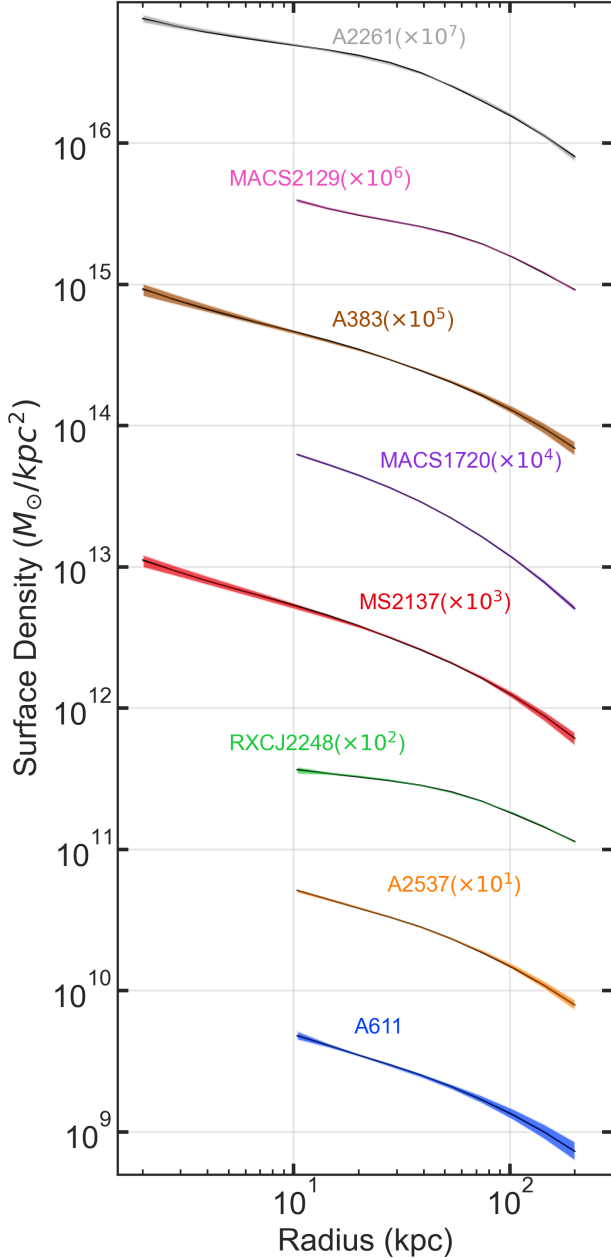


**Table 3.** Strong lensing results summary. Where confidence intervals are given, the 14th- and 86th-percentile values are indicated. The parameter  $r_c$  is the cNFW core radius. The BCG luminosity is measured using the closest HST filter to the rest frame wavelength, so as to be approximately comparable to V-band. Measurement uncertainties in luminosity are  $<2\%$ . The halo offset from the BCG is the inferred projected offset in the plane of the sky.

Cluster Name	RMS Pos.			Halo Mass ( $10^{14} M_\odot$ )	Halo Concen- tration	BCG Mass ( $10^{12} M_\odot$ )	BCG Lum. ( $10^{11} L_\odot$ )	2-D Halo	
	Img. Plane $\chi^2$ [red.]	Error (arcsec)	$r_c$ (kpc)					BCG M/L ( $M_\odot/L_\odot$ )	Offset from BCG (kpc)
Abell 611	20.7 [0.36]	0.32	$0.52^{+6.48}_{-0.48}$	$8.77^{+3.34}_{-2.30}$	$6.20^{+1.17}_{-1.05}$	$1.21^{+2.74}_{-0.88}$	3.25	$3.72^{+8.43}_{-2.71}$	$4.18^{+5.75}_{-2.80}$
Abell 2537	22.0 [1.57]	0.59	$1.18^{+6.76}_{-1.12}$	$9.42^{+1.77}_{-1.42}$	$6.77^{+0.90}_{-0.76}$	$0.93^{+1.09}_{-0.48}$	3.32	$2.79^{+3.28}_{-1.43}$	$5.44^{+1.18}_{-1.10}$
RXC J2248.7-4431	116.8 [1.98]	0.73	$19.83^{+13.03}_{-9.41}$	$18.39^{+1.49}_{-1.30}$	$5.39^{+0.71}_{-0.59}$	$0.82^{+0.88}_{-0.74}$	4.80	$1.70^{+1.84}_{-1.54}$	$3.11^{+1.27}_{-1.17}$
MS 2137.3-2353	39.0 [0.64]	0.44	$0.10^{+0.52}_{-0.08}$	$5.85^{+1.22}_{-0.96}$	$7.91^{+1.13}_{-0.99}$	$0.72^{+0.88}_{-0.19}$	3.26	$2.22^{+0.75}_{-0.59}$	$1.22^{+0.96}_{-0.69}$
Abell 383	24.9 [1.08]	0.48	$0.39^{+2.61}_{-0.36}$	$7.79^{+1.92}_{-1.38}$	$6.71^{+1.01}_{-0.89}$	$1.05^{+0.40}_{-0.33}$	3.22	$3.29^{+1.25}_{-1.02}$	$2.53^{+1.63}_{-1.13}$
Abell 2261	83.5 [3.34]	0.83	$15.53^{+4.43}_{-3.28}$	$8.23^{+0.98}_{-0.82}$	$10.10^{+1.08}_{-0.99}$	$0.77^{+0.30}_{-0.16}$	5.64	$1.36^{+0.53}_{-0.28}$	$3.54^{+4.22}_{-1.24}$
MACS 2129.4-0741	75.6 [2.44]	0.79	$54.80^{+22.98}_{-17.57}$	$10.70^{+0.74}_{-0.64}$	$7.23^{+1.13}_{-0.99}$	$2.13^{+0.38}_{-0.36}$	2.03	$10.49^{+1.89}_{-1.75}$	$12.99^{+1.30}_{-1.18}$
MACS 1720.3+3536	86.8 [5.79]	1.07	$0.04^{+0.24}_{-0.04}$	$4.28^{+0.31}_{-0.27}$	$10.83^{+0.65}_{-0.66}$	$0.38^{+0.25}_{-0.14}$	3.01	$1.27^{+0.84}_{-0.46}$	$5.06^{+0.82}_{-0.83}$



**Figure 6.** Surface density inferred from strong lensing ("data", in color) and the corresponding median SIDM modeled surface density ("model", in black) versus radius for each real cluster. The area shown for each is the 68% confidence interval. The clusters are offset by one decade each for display purposes.



## 5.2 Abell 2537

For this cluster we infer a central DM halo mass of  $9.42^{+1.77}_{-1.42} \times 10^{14} M_{\odot}$ . In [Newman et al. \(2013a\)](#) they infer a somewhat higher value of  $13.1^{+1.3}_{-1.2} \times 10^{14} M_{\odot}$  using a purely NFW profile and combining strong and weak lensing. In [Cerny et al. \(2018\)](#), they employ a model with two dPIE DM halos with different center coordinates, and find a mass within 400 kpc of the BCG of  $2.6 \pm 0.5 \times 10^{14} M_{\odot}$ . Our inferred value for mass within that radius is nearly the same, with a median value of  $2.5 \times 10^{14} M_{\odot}$ .

Our inference for the BCG mass is  $0.93^{+1.09}_{-0.48} \times 10^{12} M_{\odot}$ . Other authors do not specify their inferred BCG masses, but we note that

in [Newman et al. \(2013a\)](#) they measure a luminosity of  $5.86 \times 10^{11} M_{\odot}$ , and in [Cerny et al. \(2018\)](#) they measure a luminosity of  $5.27 \times 10^{11} M_{\odot}$ , each of which when combined with our inferred mass results in a reasonable mass-to-light ratio of approximately 1.6 to 1.8.

For Abell 2537, we infer a modest core radius of  $1.18^{+6.76}_{-1.12}$  kpc. This is in tension with the inference of [Newman et al. \(2013b\)](#) of  $46.8^{+34.5}_{-19.2}$  kpc. We are unsure of the reason for the discrepancy, but note that the measured half-light radius of the BCG is 15.7 kpc, which goes beyond the DM core radius, increasing the possibility for degenerate solutions between the two. Examination of the posterior plot (Figure F2) shows a mild bimodality in the BCG mass, possibly also admitting a larger core size. Note also that this cluster has the fewest images in the sample (16), and the fewest source points (4). The image position data is the same as that used in [Newman et al. \(2013a\)](#). A small data set could potentially limit the ability of the model to accurately constrain the mass profile.

## 5.3 RXC J2248.7-4431

For this cluster we infer a central DM halo mass of  $18.39^{+1.49}_{-1.30} \times 10^{14} M_{\odot}$ . In [Caminha et al. \(2016\)](#), in their reference case 2 they find a mass of  $2.90 \pm 0.02 \times 10^{14} M_{\odot}$  within an aperture of 250 kpc. The corresponding median value for our inference would be very similar;  $2.88 \times 10^{14} M_{\odot}$ . In [Bonamigo et al. \(2018\)](#), they infer an  $m_{200}$  of  $20.3 \pm 6.7 \times 10^{14} M_{\odot}$ , in good agreement with our inference. We infer a BCG mass for RXCJ2248 of  $0.82^{+0.88}_{-0.74} \times 10^{12} M_{\odot}$ . We were unable to find comparable inferences from other authors. We infer a core radius of  $19.83^{+13.03}_{-9.41}$  kpc, and we were not able to find comparable cNFW core size inferences from other authors.

## 5.4 MS 2137.3-2353

We infer a central DM halo mass of  $5.85^{+1.22}_{-0.96} \times 10^{14} M_{\odot}$  for this cluster. In [Donnarumma et al. \(2009\)](#), they found an  $m_{200}$  of  $4.4^{+0.6}_{-0.5} \times 10^{14} M_{\odot}$  using a strong lensing model, and [Newman et al. \(2013a\)](#) found an  $m_{200}$  of  $3.63^{+1.26}_{-0.81} \times 10^{14} M_{\odot}$  using a combination of strong and weak lensing. Both of these figures are consistent with our inference.

While we infer a BCG mass of  $0.72^{+0.88}_{-0.19} \times 10^{12} M_{\odot}$ , other authors do not report their BCG masses. However, we note that our measured BCG luminosity of  $3.26 \times 10^{11} L_{\odot}$  and that measured in [Newman et al. \(2013a\)](#) of  $3.20 \times 10^{11} L_{\odot}$  are similar, and result in reasonable mass-to-light ratios of approximately 2.2.

We infer a very small core radius of  $0.10^{+0.52}_{-0.08}$  kpc, as does [Newman et al. \(2013b\)](#), at  $2.82^{+3.01}_{-2.39}$  kpc.

## 5.5 Abell 383

For this cluster we infer a central DM halo mass of  $7.79^{+1.92}_{-1.38} \times 10^{14} M_{\odot}$ . In [Zitrin et al. \(2011\)](#) they find a similar mass of  $7.67 \times 10^{14} M_{\odot}$  from a generalized NFW profile. In addition, we find the 2D projected mass on the halo within 50 kpc, the distance to the large tangential arc of systems 1 and 2, is  $2 \times 10^{13} M_{\odot}$ . This value is consistent with  $1.7 \times 10^{13} M_{\odot}$ ,  $2.2 \times 10^{13} M_{\odot}$ , and  $2 \times 10^{13} M_{\odot}$  from [Monna et al. \(2015\)](#), [Newman et al. \(2011\)](#), and [Zitrin et al. \(2011\)](#) respectively.

We infer a core radius of  $6.66^{+6.89}_{-4.20}$  kpc for the DM halo. We were not able to find comparable cNFW core size inferences from other authors. Our inferred BCG mass is  $1.05^{+0.40}_{-0.33} \times 10^{12} M_{\odot}$  which

is lower than the results [Monna et al. \(2015\)](#) of  $6.05 \times 10^{12} M_{\odot}$  or  $6.13 \times 10^{12} M_{\odot}$ , depending if they included or did not include velocity dispersion measurements. We note that our measured luminosity of  $3.22 \times 10^{11} L_{\odot}$  when coupled with our inferred BCG mass results in a reasonable mass-to-light ratio of  $\sim 3.3$ .

### 5.6 Abell 2261

For cluster Abell 2261, we infer a central DM halo mass of  $8.23^{+0.98}_{-0.82} \times 10^{14} M_{\odot}$ . In [Coe et al. \(2012\)](#), they found  $m_{200}$  of  $9.54^{+0.84}_{-0.84} \times 10^{14} M_{\odot}$  by using a combination of weak lensing and strong lensing when assuming a spherical NFW profile halo, which is consistent with our inference.

We inferred a BCG mass of  $0.77^{+0.30}_{-0.16} \times 10^{12} M_{\odot}$ , and a core radius of  $15.53^{+4.43}_{-3.28}$  kpc. We were unable to find inferences from other authors for these parameters.

### 5.7 MACS 2129.4-0741

For this cluster we infer a central DM halo mass of  $10.70^{+0.74}_{-0.64} \times 10^{14} M_{\odot}$ . In [Monna et al. \(2017\)](#), they specify the mass enclosed within the Einstein Parameter,  $\Theta_E$ , given as  $29 \pm 4''$ . Within this radius, they find a mass of  $8.6 \pm 0.6 \times 10^{13} M_{\odot}$ . Using our model, we find a corresponding median value of  $17.5 \times 10^{13} M_{\odot}$  within that same radius.

Similarly, our model infers a median BCG mass within  $\Theta_E = 29''$  of  $2.03 \times 10^{12} M_{\odot}$ , whereas [Monna et al. \(2017\)](#) finds  $8.4 \pm 2 \times 10^{12} M_{\odot}$ .

This cluster has the largest inferred core size in our sample, at  $54.8^{+23.0}_{-17.6}$  kpc. In [Monna et al. \(2017\)](#) they find an even larger core radius of  $101^{+13}_{-11}$  kpc. However, as noted in [Monna et al. \(2017\)](#), the DM halo core radius correlates with the BCG mass profile, thus they speculate that the core radius may be large because of an overestimate of the BCG mass.

### 5.8 MACS 1720.3+3536

For this cluster we infer a central DM halo mass of  $4.28^{+0.31}_{-0.27} \times 10^{14} M_{\odot}$ . In [Zitrin et al. \(2015\)](#) they use strong lensing to specify the mass enclosed within  $136''$  of the center. They find a value of  $3.35 \times 10^{14} M_{\odot}$  for their NFW model. The corresponding median value for our model is a similar  $3.57 \times 10^{14} M_{\odot}$ . Note that our model is very close to NFW, as the inferred core radius is quite small at  $0.04^{+0.24}_{-0.04}$  kpc, the smallest in our sample. We can find no other works that present estimates of the core radius or BCG mass for this cluster.

### 5.9 Halo and BCG masses

The primary results of the strong lensing models are the surface density profiles, which are shown as the colored bands in Figure 6. These profiles are used as data for the SIDM profile matching described in Section 6. The black lines in Figure 6 are the surface density profiles as modeled by the SIDM halo matching. The match is better than 0.1 dex for all clusters.

The posterior distributions of halo core radius, halo mass and BCG mass are shown in Table 3. (Note that these inferences are not used for the SIDM halo analysis.) Our DM halo core inferences range from essentially zero (i.e., MS2137, MACS1720) to more

than 50 kpc (MACS2129). Core size is an important characteristic in this analysis, as a small core rules out strong self-interactions.

We infer DM halo masses in the range of  $4 \times 10^{14} M_{\odot}$  to  $1.8 \times 10^{15} M_{\odot}$ . These are broadly consistent with those found by other authors. We infer BCG masses in the range of  $7 \times 10^{11} M_{\odot}$  to  $2.1 \times 10^{12} M_{\odot}$ . These are generally consistent with those found for these objects by other authors, with the exceptions of A383 (where our inference is lower than that of [Monna et al. \(2015\)](#)) and MACS2129 (where our inference is lower than that of [Monna et al. \(2017\)](#), however, those authors speculate that their BCG mass may be an overestimate).

A potential degeneracy can occur in lens models between BCG mass and halo mass, especially if the BCG is closely co-centered with the DM halo, since the mass is a free parameter in both profiles and both deflect image positions similarly. In a similar way, degeneracy can occur between BCG mass and core size. As a sanity check for the inferred BCG masses, we calculate the mass-to-light ratio for each, using the closest HST filter to V-band in the rest frame. The luminosities were measured in Gaia/Source Extractor and corrected for galactic extinction.

[Newman et al. \(2013a\)](#) used a stellar population synthesis model and assumed a Chabrier initial mass function (IMF) ([Chabrier 2003](#)) to arrive at a mass-to-light ratio  $Y_V = M_*/L_V$  for 7 giant elliptical BCGs, finding a range of 1.80 to 2.32 in V-band, with low scatter. The assumption of a Salpeter IMF ([Salpeter 1955](#)) increases the ratio by a factor of 1.78, resulting in an upper value of 4.13. In [Andrade et al. \(2019\)](#), they note the possibility of a super-Salpeter IMF in Abell 611, which would further increase the upper limit. Our results are consistent with those expected values, with the exception of MACS2129, for which we find  $Y_V = 10.49^{+1.89}_{-1.75}$ . We do not know the reason for this outlier, but we speculate that it may be caused by difficulty in separating the BCG light from three other bright objects within the half-light radius of the BCG (approximately 17 kpc). As a test, we made a separate strong lens model for MACS2129 with  $Y_V$  constrained to a value of 4. The resulting fit was inferior to the original, with  $\chi^2$  increasing from 77 to 187, RMS position error increasing from  $0''.79$  to  $1''.30$ , and only 28 out of 31 images matched. The inferred core size from that run was smaller than the original run, decreasing to a median posterior value of 39.4 kpc from the original 54.8 kpc, which would cause a decrease in the inferred SIDM cross section for that cluster.

### 5.10 Halo Concentrations

We infer halo concentrations with median posterior values ranging from  $5.39^{+0.71}_{-0.59}$  (RXCJ2248) to  $10.83^{+0.65}_{-0.66}$  (MACS1720), with a median value of 7.0 (see Table 3). For comparison, the concentration-mass relation of [Diemer & Joyce \(2019\)](#) predicts median concentrations  $\simeq 4.0$  for halos at redshifts of 0.2 to 0.6 and in the mass range of  $10^{14} M_{\odot}$  to  $10^{15} M_{\odot}$ . Also, [Merten et al. \(2015\)](#) observed concentrations of  $3.7 \pm 0.65$  for 19 X-ray clusters in the CLASH sample. As we discuss in Appendix C, this discrepancy can potentially be explained if the lines of sight to lensing clusters are preferentially oriented along the major axis of the clusters. The concentrations for prolate halos can be biased upward by up to 60%. (The concentration parameter *per se* is not used in the subsequent SIDM analysis; rather, the entire radial halo profile is used, as described in Section 6.) In addition, [Fielder et al. \(2020\)](#) showed that concentration will be significantly higher for a DM halo when mass from its associated subhalos are excluded from the calculation. Our models do account for some subhalo mass separately (for the larger perturbers), making their results at least partially applicable here.

### 5.11 BCG Offsets from DM Halo Centers

An observable consequence of cored SIDM halos would be oscillations of BCG about the center of the halo after mergers, which would persist for several Gyr (Kim et al. 2017). In Harvey et al. (2019), they used simulations to examine the effect of DM self-interaction on BCG offsets, and concluded that the distribution of such offsets from an ensemble of clusters would exhibit a median value of  $3.8 \pm 0.7$  kpc for a CDM scenario (i.e.,  $\sigma/m = 0 \text{ cm}^2/\text{g}$ ), and  $8.6 \pm 0.7$  kpc in a scenario where  $\sigma/m = 1 \text{ cm}^2/\text{g}$ . The right-most column of Table 3 and the first histogram in Figure 5 show our inferred 2-dimensional offset of the DM halo centers for each cluster, which range from approximately 1 kpc to 10 kpc, with a median of approximately 4 kpc, except for MACS2129, which is an outlier at 10 kpc to 15 kpc. Since these are 2-dimensional offsets, we can estimate that the corresponding 3-dimensional offsets would be larger by a factor of approximately  $\sqrt{3/2} = 1.23$ , although the precise value would depend on the distribution of the offsets. Using this factor results in a corresponding median value of approximately 5 kpc for our data, which would imply  $\sigma/m \ll 1 \text{ cm}^2/\text{g}$  in light of the findings of Harvey et al. (2019).

## 6 SIDM HALO ANALYSIS

It has been argued from observations of groups and clusters of galaxies, that the cross section must be velocity-dependent to have a significant effect for less massive galaxies (Kaplinghat et al. 2016). This velocity dependence can occur in several ways: resonant self-interaction of dark matter (Chu et al. 2019), light mediator models with either elastic or inelastic collisions (Feng et al. 2010; Loeb & Weiner 2011; Tulin et al. 2013a; Tulin & Yu 2018; Alvarez & Yu 2020; Boddy et al. 2016; Vogelsberger et al. 2019), bound states (Braaten et al. 2018), and strongly interacting massive particles (Hochberg et al. 2015; Choi et al. 2017). See Chu et al. (2020) for a review of these models in addition to a model-independent approach for approximating velocity dependence using effective range theory. As the range of particle velocities in our cluster sample is relatively narrow, we opt for a constant velocity analysis here.

### 6.1 SIDM Halo Model

For the SIDM halo model, we following the procedure in Kaplinghat et al. (2016) and write the full profile as an inner isothermal profile and an outer NFW profile, with the two profiles matched in mass and density at a radius  $r_1$ , which is determined by the cross section. The idea here is to get a smooth density profile that interpolates between an isothermal core and a collisionless outer envelope well enough to capture the halo profiles inferred from SIDM simulations. The characteristic radius  $r_1$  dividing the inner and outer regions can be approximated by setting the average scattering rate per particle times the age of the halo to unity:

$$\text{rate} \times \text{time} \approx \frac{\langle \sigma v \rangle}{m} \rho(r_1) t_{\text{age}} = 1, \quad (5)$$

where  $\sigma$  is the scattering transfer cross section,  $v$  is the relative velocity between DM particles,  $\rho(r_1)$  is the density of DM at the characteristic radius,  $t_{\text{age}}$  is the age of the halo, and  $\langle \dots \rangle$  denotes averaging over the velocity distribution. This is a simplification of the time-dependent process of halo assembly, but it compares well to numerical simulations (Kaplinghat et al. 2016; Robertson et al. 2020) because of the approach to equilibrium.

For the age of each halo, we adopt a value equal to the time

elapsed since the redshift of the halo, as shown in Table 2. The average relative velocity of SIDM particles, assuming a Maxwellian velocity distribution, can be shown to be  $\frac{4}{\sqrt{\pi}} \sigma_0$ , where  $\sigma_0$  is the central velocity dispersion. Assuming a constant cross section  $\sigma$  over the range of velocities accessible in the cluster, we have  $\langle \sigma v \rangle = \sigma \langle v \rangle = \frac{4}{\sqrt{\pi}} \sigma \sigma_0$ . For a model with a sharp velocity dependence,  $\sigma$  should be interpreted as the velocity averaged transfer cross section (Tulin et al. 2013b; Robertson et al. 2017b; Kahlhoefer et al. 2014; Boddy et al. 2016).

Considering the two regions, one which is thermalized by self-interactions and one which remains largely non-interacting, the complete profile can be written as

$$\rho(r) = \begin{cases} \rho_{\text{iso}}(r), & r < r_1 \\ \rho_{\text{NFW}}(r), & r \geq r_1 \end{cases} \quad (6)$$

where  $\rho_{\text{iso}}(r)$  is a cored isothermal profile (Kaplinghat et al. 2014), and  $\rho_{\text{NFW}}(r)$  is the NFW profile (see Equation 1, but with  $r_c \rightarrow 1$ ). For the region interior to  $r_1$ , interactions are common and we consider the DM particles to behave as an ideal gas, characterized by a pressure ( $p$ ), density ( $\rho$ ) and (one-dimensional) velocity dispersion ( $\sigma_0$ ) that obey an equation of state  $p = \rho \sigma_0^2$ . Assuming that the DM particles in the central region achieve hydrostatic equilibrium, we have

$$\nabla p = -\rho \nabla \Phi_{\text{tot}} \quad (7)$$

where  $\Phi_{\text{tot}}$  is the total gravitational potential from both DM and baryons. In this analysis, we use the fitted BCG from strong lensing with a dPIE profile (Equation 2) for the baryonic mass. The gravitational potential must satisfy the Poisson equation

$$\nabla^2 \phi_{\text{tot}} = 4\pi G (\rho_{\text{DM}} + \rho_{\text{BCG}}) \quad (8)$$

where  $G$  is Newton's gravitational constant,  $\rho_{\text{DM}}$  is the mass density of DM and  $\rho_{\text{BCG}}$  is the mass density of the BCG. Thus the SIDM density profile explicitly depends on the stellar distribution (Kaplinghat et al. 2014). The solution to two equations above gives  $\rho_{\text{iso}}(r)$  for the interior region.

We assume that the isothermal solution is a cored profile at small radii with central density  $\rho_0$  and central dispersion  $\sigma_0$ . For concreteness, we impose this boundary condition at 1% of the stellar core radius ( $r_{\text{core}}$  in the dPIE profile). We then evolve the isothermal Jeans equation outwards stopping at the radius  $r_1$  when the SIDM density  $\rho(r_1)$  satisfies Eq. 5. By matching the mass and density of  $\rho_{\text{iso}}$  to a NFW profile, we can find the NFW parameters  $\rho_s$  and  $r_s$  from  $\rho_0$  and  $\sigma_0$ . Note that we do not search for a second solution at larger  $r_1$  (Kaplinghat et al. 2016; Robertson et al. 2020), which could be just as good a fit. This second solution with the same  $\rho_0$  is reminiscent of the core collapse phase (Balberg et al. 2002; Elbert et al. 2015; Essig et al. 2019; Nishikawa et al. 2020), but it is not clear if this connection holds up in detail.

There are two pitfalls that impede seamless parameter space exploration. First is that when we scan over  $\rho_0$  and  $\sigma_0$ , there is no guarantee that  $r_1$  can be found. To insure against this failure, we change our variable from  $\rho_0$  to  $R_0 = \rho_0 (\sigma/m) (4/\sqrt{\pi}) \sigma_0 t_{\text{age}}$  and put a prior on  $R_0$  that is larger than unity (Ren et al. 2019; Robertson et al. 2020). Since the density falls with increasing radius, we are guaranteed to get a solution for  $r_1$ . For the present study we have adopted the following priors on the four parameters that are varied to find the SIDM solutions:  $5 < R_0 < 500$ ,  $400 < \sigma_0 < 1400$ ,  $0.01 < \sigma/m < 0.5$ ,  $10^{11} M_{\odot} < M_{\text{BCG}} < 10^{13} M_{\odot}$ . With the exception of the lower limit of  $\sigma/m$ , our prior boundaries do not impact the inferred posteriors.

The second issue is that for a given  $r_1$  and  $\rho_{\text{iso}}(r)$ , it may not be possible to find a matching NFW profile (see also, Robertson et al. (2020)). The procedure to find the matching NFW profile proceeds by first matching  $\gamma_M(r) = M(r)/(4\pi r^3 \rho(r))$  where  $M(r)$  is the dark matter halo mass enclosed within radius  $r$ . Since for the NFW profile  $\gamma_M(r)$  is only a function of  $r/r_s$ , we get  $r_1/r_s$  and therefore  $r_s$ . Then we can match the isothermal and NFW  $M(r)$  at  $r_1$  to infer  $\rho_s$ . However, the first step can fail if  $\gamma_M(r_1) < 0.5$  for the isothermal profile, because  $\gamma_M(r) \geq 0.5$  for the NFW profile. However, these cases are rare and they are not physically interesting, as it requires a core unlike that seen in simulations with  $\rho(r_1) \simeq \rho_0$ . With these checks in place, it is possible to find unique NFW matches for all  $\rho_{\text{iso}}(r)$  profiles generated by the likelihood sampler. Once we have the full density profile, then we can compute the 2D density profiles to compare to the data.

Before we discuss the results from the SIDM halo matching process discussed above, it is worth noting this analytic model (described in Kaplinghat et al. (2016)) has been remarkably successful in capturing the density profiles in simulations from dwarf galaxies to clusters of galaxies (Kaplinghat et al. 2016; Robertson et al. 2017a; Sokolenko et al. 2018; Robles et al. 2019; Ren et al. 2019; Robertson et al. 2020). The study in Sokolenko et al. (2018) specifically focused on clusters and investigated different ways of matching the isothermal and NFW solutions. They found that the model of Kaplinghat et al. (2016) can reproduce the core density of the halos, as shown in the left panel of Figure 22 of their paper. The inferred core is recovered at the 10-20% level for cross sections below  $1 \text{ cm}^2/\text{g}$ , which are relevant for our study. Remarkably, the analytic model provides an unbiased description over almost two orders of magnitude in cross section from  $0.1$  to  $10 \text{ cm}^2/\text{g}$ . There seems to be a bias creeping in at  $\sigma/m = 0.1 \text{ cm}^2/\text{g}$ ; if this trend continues to lower cross sections, this would imply that our inferred cross sections are biased somewhat high.

The right panel of the same figure from Sokolenko et al. (2018) shows that the kinetic energy inferred from the central dispersion is systematically lower than the average kinetic energy within  $r_1$ . This bias is important for us since we need both the cross section and the average relative velocity of DM particles to extract constraints on SIDM models. The results from Sokolenko et al. (2018) indicate that we should not use the inferred dispersion  $\sigma_0$  to estimate the average relative velocity since it can be biased low by about 20%. While this seems like a small effect, it can be an important systematic if we are constraining a cross section model with a sharp velocity dependence. Since most models predict cross sections falling with relative velocity, a conservative way of constraining SIDM models is to use the largest possible average relative velocity for each cluster. We can estimate this maximum average relative velocity as  $1.4v_{\text{max}}$  using the fact that the maximum RMS velocity of DM particles is very close  $v_{\text{max}}$  (Rocha et al. 2013b).

## 6.2 SIDM Halo Matching Inference Results

We employ an MCMC fitting code to implement the second stage of our analysis, using as input the strong lensing posterior for the DM surface density profile for each cluster. By using the entire surface density profile, the model can appropriately match the halo density profile, and accommodate multiple possible modes in the strong lensing solution set. We used the Dynesty sampler (Speagle 2020; Higson et al. 2019) to generate the MCMC posterior chain for this stage. The key posterior parameters are: cross section,  $r_1$  (the characteristic radius), average particle speed, and BCG mass, as noted in Figure 1. From this we infer the central density ( $\rho_0$ )

and the matched NFW halo parameters ( $M_{\text{vir}}$  and  $c_{\text{vir}}$ ). We fit cross sections at constant velocity, noting that the median maximum circular velocities (a rough proxy for relative particle speed) for the clusters in the sample are in the range of 1,400 km/s to 2,000 km/s, with most around 1,500 km/s.

As shown schematically in Figure 1, surface density posteriors at radii ranging from 2 kpc to 200 kpc are generated by the strong lensing model and were first decomposed into principal components using the Principal Component Analysis (PCA) in the Scikit-Learn software package (Pedregosa et al. 2011), which typically yielded 3 or 4 components for any given cluster. We found that supplying 10 logarithmically spaced radial data points ranging from 10 kpc to 200 kpc enabled good surface density profile reproduction for most clusters, but three clusters (A383, A2261 and MS2137) required that an additional 5 bins extend farther inward, to 2 kpc, to ensure that the model made a good match to the shape of the surface density profile inferred from strong lensing.

A Gaussian Mixture Model (GMM) was used to model the likelihood using the principal components of the surface density profiles. We calculated the Bayesian Information Criteria (BIC) for each cluster while varying the number of GMM components, and found that having more than four components in the GMM did not improve the BIC significantly. We therefore used four components in the GMM.

In addition to the surface density profiles, the SIDM model also requires the parameters of the BCG density profile as described above. We use the BCG scale radius as measured from photometry for this purpose. However, we do not use the BCG mass posterior from strong lensing. By varying the BCG mass independently, we are able to explore the degeneracy between the BCG mass and cross section; see Figure 8 for a comparison of the BCG mass inferred from the SIDM and cNFW fits, and the associated discussion in Section 6.2. Inference of the BCG mass is often multimodal, with larger BCG masses being associated with larger cross sections (lower DM core densities).

The surface density models produced by the SIDM halo matching model reproduced the data to within 0.1 dex or better. Plots of the matches for each cluster are shown in the Appendix in Figure E1. Note that the model relies on surface density profile rather than direct inferences of parameters such as BCG mass, halo mass, concentration, etc. This allows multimodal solutions in those parameters to be accurately incorporated into the model.

The tabulated results of the SIDM parameter inference are summarized in Table 4. Our inferred cross sections per unit mass versus mean particle speed are shown in Figure 7. Cross sections for the simulated clusters are inferred to be  $0.014^{+0.006}_{-0.003} \text{ cm}^2/\text{g}$  and  $0.023^{+0.023}_{-0.009} \text{ cm}^2/\text{g}$  for Sim. Clusters 2 and 3, respectively, at the 68% confidence level.

Cross sections for the observed clusters are inferred to be  $\sigma/m < 0.10 \text{ cm}^2/\text{g}$  for all clusters except MACS2129, which is an outlier between 0.10 and  $0.14 \text{ cm}^2/\text{g}$ . The maximum circular velocities,  $v_{\text{max}}$ , for the clusters (which is closely related to the relative particle speeds within them) ranges from approximately 1,400 km/s for low cross-sections and up to 2,000 km/s for high cross-sections, as can be seen in Figure 7 and Table 4. To constrain velocity-dependent models in a conservative manner, we recommend using the maximum average relative velocity  $\approx 1.4v_{\text{max}}$ . The central relative velocity estimate  $4\sigma_0/\sqrt{\pi}$  could be biased low by up to 20%, as discussed in the previous section. Note that the trend when the results from all the clusters are put together is that higher cross section inferences go with higher  $\sigma_0$ . This is expected because



**Figure 7.** Posteriors for DM halo  $v_{\max}$  (horizontal axes, in km/s) versus SIDM cross section (vertical axes, in  $\text{cm}^2/\text{g}$ ) from the SIDM halo matching model. The smaller boxes are for the clusters individually, and the larger box at the bottom is the composite of all 10 clusters. The 68% confidence interval is shown in a darker shade.

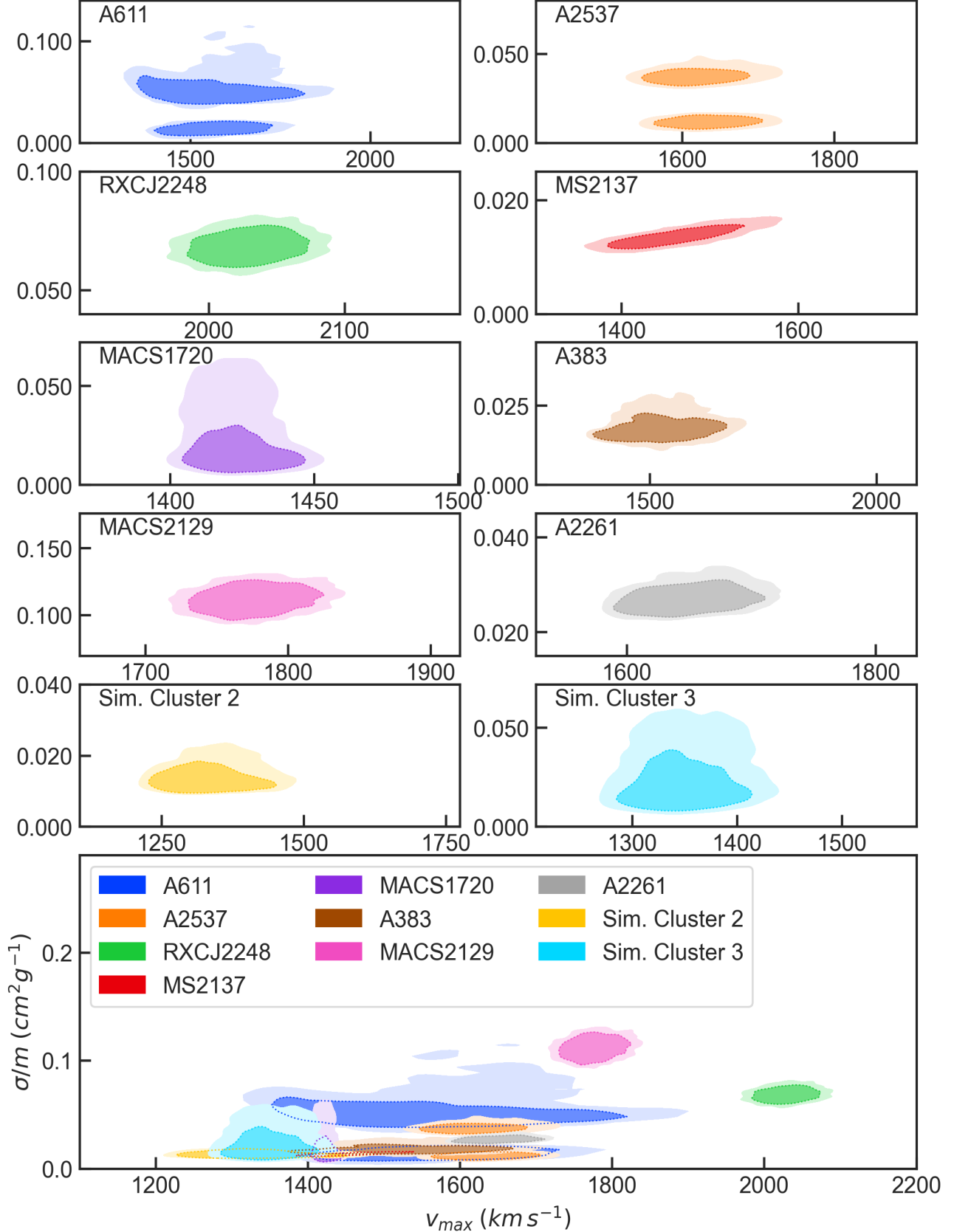
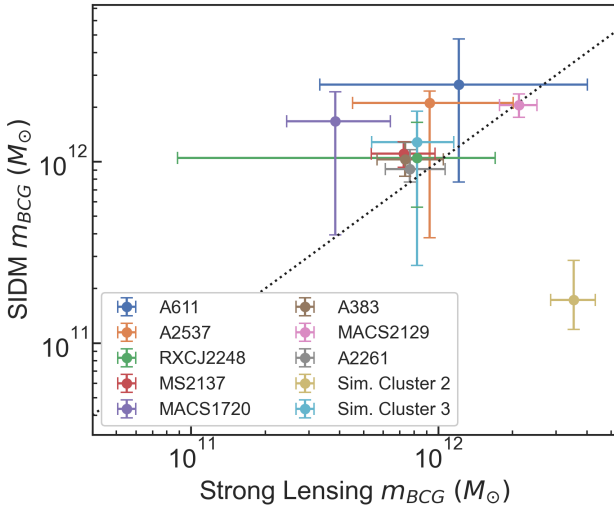


**Table 4.** SIDM parameter posterior summary. The columns are: (1) cluster name, (2) SIDM cross section per unit mass, (3)  $\log_{10}$ (cross section per unit mass) (4) transition radius, (5) central density, (6) central velocity dispersion, (7) halo maximum circular velocity, (8) BCG mass, (9) virial mass, and (10) concentration. Where values with  $\pm$  are shown, the values are the mean and standard deviation. Where upper and lower interval values are given, the median value is used and the indicated ranges are the 68% confidence intervals.

Cluster Name	$\sigma/m$ ( $\text{cm}^2\text{g}^{-1}$ )	$\log_{10}(\frac{\sigma/m}{\text{cm}^2\text{g}^{-1}})$	$r_1$ (kpc)	$\rho_0$ ( $10^6 M_\odot \text{kpc}^{-3}$ )	$\sigma_0$ ( $\text{km s}^{-1}$ )	$v_{\text{max}}$ ( $\text{km s}^{-1}$ )	$m_{\text{BCG}}$ ( $10^{12} M_\odot$ )	$m_{\text{vir}}$ ( $10^{14} M_\odot$ )	$c_{\text{vir}}$
A611	$0.060 \pm 0.055$	$-1.345 \pm 0.329$	$84.8^{+41.7}_{-60.5}$	$166.7^{+120.9}_{-49.7}$	$845^{+79}_{-278}$	$1562^{+131}_{-104}$	$2.65^{+2.10}_{-1.88}$	$10.01^{+3.93}_{-2.54}$	$7.11^{+1.27}_{-1.24}$
A2537	$0.030 \pm 0.015$	$-1.595 \pm 0.262$	$75.1^{+14.0}_{-52.8}$	$182.5^{+34.7}_{-27.3}$	$856^{+35}_{-300}$	$1630^{+70}_{-53}$	$2.11^{+0.34}_{-1.72}$	$10.73^{+2.14}_{-1.52}$	$7.80^{+0.73}_{-0.79}$
RXCJ2248	$0.069 \pm 0.007$	$-1.163 \pm 0.043$	$119.1^{+11.8}_{-10.5}$	$24.5^{+5.5}_{-3.9}$	$911^{+33}_{-32}$	$2030^{+33}_{-32}$	$1.05^{+0.60}_{-0.48}$	$25.26^{+1.63}_{-1.58}$	$4.76^{+0.20}_{-0.19}$
MS2137	$0.014 \pm 0.002$	$-1.860 \pm 0.060$	$30.4^{+2.1}_{-1.6}$	$289.2^{+44.8}_{-42.2}$	$679^{+28}_{-25}$	$1462^{+53}_{-47}$	$1.11^{+0.18}_{-0.17}$	$6.80^{+1.35}_{-1.11}$	$9.34^{+1.19}_{-1.03}$
MACS1720	$0.029 \pm 0.018$	$-1.622 \pm 0.271$	$58.4^{+36.9}_{-26.4}$	$901.7^{+599.9}_{-628.1}$	$868^{+61}_{-155}$	$1423^{+15}_{-13}$	$1.67^{+0.75}_{-1.28}$	$4.76^{+0.35}_{-0.28}$	$12.71^{+0.67}_{-0.69}$
A383	$0.020 \pm 0.006$	$-1.721 \pm 0.115$	$34.9^{+13.1}_{-4.2}$	$184.7^{+40.7}_{-55.3}$	$655^{+52}_{-35}$	$1525^{+84}_{-72}$	$1.03^{+0.25}_{-0.20}$	$9.30^{+2.43}_{-1.80}$	$8.08^{+0.98}_{-0.92}$
MACS2129	$0.112 \pm 0.010$	$-0.953 \pm 0.040$	$139.2^{+9.4}_{-9.6}$	$50.9^{+9.0}_{-7.8}$	$931^{+16}_{-17}$	$1776^{+32}_{-29}$	$2.05^{+0.32}_{-0.29}$	$14.04^{+1.09}_{-0.94}$	$4.66^{+0.26}_{-0.26}$
A2261	$0.028 \pm 0.003$	$-1.558 \pm 0.050$	$68.7^{+7.4}_{-5.3}$	$66.6^{+6.3}_{-5.7}$	$831^{+25}_{-21}$	$1652^{+42}_{-38}$	$0.91^{+0.25}_{-0.14}$	$10.63^{+1.40}_{-1.25}$	$9.31^{+0.78}_{-0.71}$
Sim. Cluster 2	$0.016 \pm 0.005$	$-1.825 \pm 0.119$	$27.7^{+9.8}_{-5.1}$	$1153.1^{+2460.3}_{-592.4}$	$594^{+45}_{-39}$	$1340^{+88}_{-67}$	$0.17^{+0.11}_{-0.05}$	$5.00^{+1.50}_{-0.97}$	$10.15^{+1.22}_{-1.17}$
Sim. Cluster 3	$0.028 \pm 0.015$	$-1.612 \pm 0.227$	$46.3^{+31.9}_{-19.8}$	$915.6^{+780.8}_{-680.3}$	$759^{+71}_{-170}$	$1349^{+46}_{-37}$	$1.28^{+0.62}_{-1.01}$	$5.29^{+0.96}_{-0.71}$	$9.68^{+0.95}_{-0.93}$

**Figure 8.** Comparison of the BCG mass inferred from strong lensing and from the SIDM model. The error bars indicate the 68% confidence interval. The diagonal line represents equality.



a higher cross-section will result in a larger interaction rate and, in turn, a larger  $r_1$  (characteristic radius) and greater average particle speed within  $r_1$ .

The cross section posteriors for the observed clusters are clearly not consistent with one another, due to errors in the modeling. For this reason, we do not simply average the results, but seek to disentangle the modeling error in Section 6.3.

Each stage of the model has potential sources of modeling error. For the lensing model, these include variations of the radial profile and shape away from our cored elliptical NFW profile model, and variations of subhalo mass profile away from the scaling relations used to model them. For the SIDM model, the potential sources of error are related to the ability of the spherical analytic model to fit SIDM halos when the cross section is small. These are all factors that can be tested with simulated halos in future work.

Figure 8 shows the BCG masses for each cluster inferred from

strong lensing compared to the inference results from the SIDM model. The correlation between the two models is good, with the notable exception of Sim. Cluster 2. We reran the SIDM analysis for that cluster with a strong Gaussian prior on BCG mass:  $\log(m_{\text{BCG}}/M_\odot) = 12.54 \pm 0.1$  (i.e., the value inferred from the strong lensing analysis of that cluster). Our results were robust under that test, showing a only very small increase in cross section.

We also compared the inferences for concentration,  $c_{\text{vir}}$ , and the virial mass of the DM halo,  $m_{\text{vir}}$ , from the strong lensing fits and the SIDM halo matching results. For the strong lensing cNFW fits, we defined  $c_{\text{vir}} = r_s/r_{\text{vir}}$ , which should be comparable to the NFW  $c_{\text{vir}}$  when the cNFW core radius  $r_c \ll r_s$ . Our results quoted in Tables 3 and 4 show that the two estimates are largely consistent with one another at the 10% level. The exceptions include the two highest mass systems, RXCJ2248 and MACS2129, that had virial masses inferred from the SIDM halo matching procedure that were about 30% higher than those from the cNFW fit to the strong lensing data. There is a systematic trend for the SIDM halo matching procedure to prefer slightly higher halo virial masses and concentrations, but mostly within individual error bars. MACS2129 is also an outlier in this regard with its inferred concentration in the SIDM halo matching procedure being lower, which could be related to its preference for larger cNFW core sizes.

### 6.3 Cross Section Upper Limit

After having obtained posterior chains that include cross section per unit mass ( $sm = \sigma/m$ ) for the simulated and observed clusters, we turn to estimating the true underlying cross section. One option is to average the cross sections obtained for the observed clusters. However, this would not be appropriate given that the inferred cross sections are not statistically consistent with each other. In some cases, the inferred error on the cross section may be smaller than the uncertainty arising from the fact that the analytic model is an approximate description of the SIDM density profile, as we have discussed. Therefore, we should include a source of “modeling” error in estimating the underlying true cross section. For this purpose, we recall that the work of Sokolenko et al. (2018) showed a spread of about 10-20% in the inferred core sizes for small cross sections

( $\sigma/m < 1 \text{ cm}^2/\text{g}$ ). We expect that this will translate into roughly constant error in  $\log(\sigma/m)$ .

For the observed clusters, we denote the means and standard deviations for the posteriors of  $\log_{10}((\sigma/m)/(\text{cm}^2/\text{g}))$  from the SIDM analysis as  $\mu_i$  and  $\epsilon_i$ , with  $i = 1, \dots, 8$ . For the two simulated clusters, we use the index  $k = 1, 2$ , so that the observed values are  $\mu_k$  and  $\epsilon_k$ . We assume that the observed and simulated cluster values are drawn from a normal distribution with means  $\mu_{\text{true}}$  and  $\mu_{\text{sim}}$  for the observed and simulated clusters, respectively. The standard deviation of the normal distribution represents the modeling error discussed above (common to both simulated and observed clusters) and we denote it by  $\epsilon_{\text{model}}$ . Thus, there are three parameters  $\mu_{\text{true}}$ ,  $\mu_{\text{sim}}$  and  $\epsilon_{\text{model}}$  that we wish to infer.

Our "data" for this third analysis stage consists of the cross section posterior means and standard deviations for each cluster from the SIDM halo matching stage. We also tested a model that used the entire output chains from the SIDM model rather than just the means and standard deviations, and found its results very similar. We therefore opted to use this simpler approach. For each observed cluster  $i$ , the mean and standard deviation of the cross section inferred by the SIDM analysis are  $\mu_i$  and  $\epsilon_i$ , respectively. The likelihood of observing  $\mu_i$  and  $\sigma_i$  can be written as

$$L = \prod_i N(\mu_i | \mu_{\text{true}}, \sqrt{\epsilon_i^2 + \epsilon_{\text{model}}^2}) \times \prod_k N(\mu_k | -2, \sqrt{\epsilon_k^2 + \epsilon_{\text{model}}^2}) \quad (9)$$

where  $N(x | \text{mean}, \text{standard deviation})$  denotes the PDF of a normal distribution with specified mean and standard deviation. We adopt uniform priors between  $-2$  and  $0$  for  $\mu_{\text{true}}$  (which means the true cross section is between  $0.01$  and  $1 \text{ cm}^2/\text{g}$ ) and a uniform prior between  $0$  and  $2$  for  $\epsilon_{\text{model}}$ . We have set the mean for the simulated CDM clusters to  $-2$  (which corresponds to a cross section of  $0.01 \text{ cm}^2/\text{g}$ ) because that is the lowest cross section allowed in the SIDM halo matching procedure. Note that the simulated clusters are both consistent with  $0.01 \text{ cm}^2/\text{g}$  in Table 7.

We infer that the true SIDM cross section ( $= 10^{\mu_{\text{true}}}$ ) is  $0.035^{+0.015}_{-0.010} \text{ cm}^2/\text{g}$  (68% C.L.), and is less than  $0.065 \text{ cm}^2/\text{g}$  at the 95% confidence level.

We repeated our analysis using means and standard deviations for  $\sigma/m$  rather than  $\log_{10}(\sigma/m)$ , and normal distribution about the true underlying cross section. We also did the analysis with a normal distribution truncated below  $0$ . They both yielded results consistent with those obtained above. To ascertain the impact of the non-Gaussian features in the posteriors, we also did a check with a 4-component GMM to model the posterior for  $\log_{10}(\sigma/m)$  of each cluster. In this case, our likelihood for the observed clusters is modified to  $L = \prod_i \sum_{\alpha} w_{i\alpha} N(\mu_{i\alpha} | \mu_{\text{true}}, \sigma_{i\alpha}) \times \prod_k \sum_{\alpha} w_{k\alpha} N(\mu_{k\alpha} | -2, \sigma_{k\alpha})$ , where  $\sigma_{i\alpha}^2 = \epsilon_{i\alpha}^2 + \epsilon_{\text{model}}^2$ . In the preceding equation,  $w_{i\alpha}$  are the weights for the GMM components (labeled by  $\alpha$ ), and the corresponding means and standard deviations are  $\mu_{i\alpha}$  and  $\epsilon_{i\alpha}$  for each cluster  $i$ , and the same for the simulated cluster with index  $k$ . The result from the likelihood using the GMM components is that  $\sigma/m < 0.062 \text{ cm}^2/\text{g}$  at 95% C.L., consistent with what we found previously.

In comparison, a constraint on SIDM  $\sigma/m$  of  $0.10^{+0.03}_{-0.02} \text{ cm}^2/\text{g}$  for galaxy clusters was reported in Kaplinghat et al. (2016). This was based on data from 6 clusters from Newman et al. (2013a,b), which employed strong lensing, weak lensing and stellar kinematic approaches to determine the cluster profiles. In Sa-

gunski et al. (2020), they use a Jeans analysis technique and find  $\sigma/m < 0.35 \text{ cm}^2/\text{g}$  (95% C.L.) for galaxy clusters. Cluster mergers can also put constraints on SIDM cross section, as collisionless DM would not be slowed in a cluster merger. In Randall et al. (2008) they analyze the collision in the Bullet Cluster (galaxy cluster 1E 0657-56) and find  $\sigma/m < 1.25 \text{ cm}^2/\text{g}$  at the 68% confidence level. In Robertson et al. (2017a), they use simulations on the same cluster and find a more relaxed constraint of  $2 \text{ cm}^2/\text{g}$  in their fiducial model. Harvey et al. (2015) analyzed an ensemble of 72 clusters to find  $\sigma/m < 0.47 \text{ cm}^2/\text{g}$  at the 95% confidence level. Analyses of other cluster collisions that put an upper constraint on SIDM cross section include  $\sigma/m < 4 \text{ cm}^2/\text{g}$  in MACS J0025.4-1222 (Bradač et al. 2008),  $\sigma/m < 3 \text{ cm}^2/\text{g}$  in Abell 2744 (Merten et al. 2011) and  $\sigma/m < 7 \text{ cm}^2/\text{g}$  in cluster DLSCL J0916.2+2951 (Dawson et al. 2012).

The limits we have obtained are very stringent, as the comparison above shows. Unlike previous work, our dedicated SIDM analysis used the full radial surface density profile, allowing for stronger constraints. The fact that we selected clusters with masses close to  $10^{15} M_{\odot}$  and with images over a wide range of radii also likely played a part in this. We can test this hypothesis with more heterogeneous cluster data sets in the future. One may worry that our reliance on the analytic model down to such low cross sections is leading to overly stringent constraints. As we discussed previously, the model has only been validated for cross sections of  $0.1 \text{ cm}^2/\text{g}$  and higher by Sokolenko et al. (2018). However, the cNFW fits to the strong lensing data recovered uniformly high surface densities at  $10 \text{ kpc}$  for the clusters, close to that inferred for the simulated clusters, and the least dense among the observed clusters (MACS2129 and RXCJ2248) are the ones that prefer larger cross sections. These high surface densities lead to the strong constraints on the cross section. A related issue is that the analytic model may not be capturing the effects of BCG stellar distribution on the SIDM density profile well enough at low cross sections because the inner halo is not close to isothermal. However, it is not clear why there would be a bias to lower cross sections in this case. Note that the inferred  $r_1$ , despite the small cross sections, is in the range of  $30$  to  $140 \text{ kpc}$ , where the cluster is dark matter dominated. This is again related to the high dark matter densities required to model the strong lensing images. It is also useful to keep in mind that the impact of the baryons on the SIDM density profile of these  $\sim 10^{15} M_{\odot}$  clusters is much smaller than for  $10^{14} M_{\odot}$  and lower mass clusters. Nevertheless, we cannot rule out that systematic errors of order  $0.1 \text{ cm}^2/\text{g}$  are introduced by the method, and this needs to be investigated using simulations.

#### 6.4 Outliers

Besides having the highest inferred SIDM cross section, Cluster MACS2129 is unusual in several regards. It has the highest redshift in our sample ( $0.589$ ), and consequently the lowest  $t_{\text{age}}$ , at  $7.8 \text{ Gyr}$ . A lower value of  $t_{\text{age}}$  will cause a higher cross section inference, as can be seen by inspecting Equation 5. It was the only cluster for which our lens model was unable to reproduce one of the data images. MACS2129 also has the largest DM halo core inferred from strong lensing, at  $54.8^{+23.0}_{-17.6} \text{ kpc}$ , which will also drive the inferred cross section to be higher, as a core allows for a larger thermalized region. In addition, this cluster's mass-to-light ratio is an outlier, at  $Y_V = 10.49^{+1.89}_{-1.75}$ , while the inference for the other 7 clusters is for  $1 < Y_V < 4$ . As discussed in Section 5, we investigated the impact of constraining  $Y_V$  to a value of  $4$  for MACS2129, and it would indeed result in a smaller core size (a median of  $39.4 \text{ kpc}$  compared to the original  $54.8 \text{ kpc}$ ) but the fit of the model was significantly

inferior to the original. A smaller core would lead to a lower inferred SIDM cross section for that cluster.

Additionally, it is worth noting that cluster A2261 is an outlier in one regard: the inferred core radius is approximately 15 kpc (see Table 3), which is at the higher end of the range for the observed clusters, but the inferred median SIDM cross section is only  $0.027 \text{ cm}^2/\text{g}$  (Table 4). This is in contrast to the other clusters, which show a strong positive correlation between core radius and cross section. This can be partially explained by the relatively high  $t_{\text{age}}$  of 10.8 Gyr for A2261, the second highest in our sample, which implies a smaller cross section because we can only constrain  $\text{age} \times \sigma/m$ .

## 7 CONCLUSIONS

With the aim of constraining the self-interaction cross section of DM particles, we have constructed strong lensing models of 8 observed clusters (see Figure 2). The models include DM subhalos for the perturbing galaxies, to more accurately model the perturber mass distribution. We model SIDM halos using a well-tested analytic model, in which the outer region follows an NFW profile and the inner region is isothermal due to DM self-interactions, with the transition radius being set by the self-interaction cross section. The inferred strong lensing surface density is used to infer the self-interaction cross section. We then construct a model to infer the true underlying SIDM cross section, allowing for systematic offsets due to mismodeling. We have tested our inference pipeline on two mock data sets obtained from the Illustris-TNG simulation. Our key findings are summarized below.

Using strong lensing alone we were able to reproduce the image positions in our cluster sample with RMS image position errors ranging from  $0''.32$  to  $1''.07$ . Our methodology includes separate lens model components for the member galaxy's baryonic and DM components, allowing for more flexible characterization of each galaxy's matter distribution. The models reproduced all data images, with the exception of one image in the outlier MACS2129.

We find that the inference for concentration was biased high for the two simulated relaxed clusters (see Table 1) compared to the cosmological expectation for spherically-averaged halos. For the observed clusters we find a median concentration of 7.0, which is also higher than would be expected from the concentration-mass relation, and higher than that found in X-ray observations of CLASH clusters. As discussed in Appendix C, this can be expected in situations where the line of sight is preferentially oriented along the major axis of halos, which boosts strong lensing probability. In the common case of prolate halos with their major axis oriented along the line of sight, halo concentration can be biased by up to  $\sim 60\%$ . Previous works (e.g., Newman et al. 2013a) have also noted that observed concentrations for a sample of clusters similar to ours are indeed higher than what is predicted from mass-concentration relations in CDM simulations.

We found that the BCGs centers in our models are either coincident with the DM halo centers or offset by few to 10 kpc (Figure 5). The median offset is about 4 kpc, as measured in the plane of the sky, which would correspond to approximately 5 kpc in the distance assuming isotropy. Harvey et al. (2019) used simulations to conclude that the distribution of offsets from an ensemble of clusters would exhibit a median value of  $3.8 \pm 0.7$  kpc for a CDM scenario (i.e.,  $\sigma/m = 0$ ), and  $8.6 \pm 0.7$  kpc in a scenario where  $\sigma/m = 1 \text{ cm}^2/\text{g}$ . Comparing to Harvey et al. (2019), the median value we obtained is consistent with  $\sigma/m \ll 1 \text{ cm}^2/\text{g}$ .

Using the SIDM halo model, the cross section per unit mass for

all observed clusters had median values in the range of  $0.02 \text{ cm}^2/\text{g}$  to  $0.07 \text{ cm}^2/\text{g}$  (Figure 7), with the exception of outlier MACS2129 at  $0.11 \text{ cm}^2/\text{g}$ . We combined these individual measurements allowing for an unknown modeling error, and inferred an upper limit of  $0.065 \text{ cm}^2/\text{g}$  at the 95% C.L. (see Sections 6.3). This is the most stringent upper limit on self-interaction cross section yet reported. In comparison, a constraint on SIDM  $\sigma/m$  of  $0.10^{+0.03}_{-0.02} \text{ cm}^2/\text{g}$  for galaxy clusters was reported in Kaplinghat et al. (2016), using a simple SIDM halo model calibrated to N-body simulations. Sagunski et al. (2020) found  $\sigma/m < 0.35 \text{ cm}^2/\text{g}$  (95% C.L.) for galaxy clusters using Jeans analysis. The most restrictive upper limit from cluster mergers puts  $\sigma/m < 0.47 \text{ cm}^2/\text{g}$  at 95% C.L. (Harvey et al. 2015).

Our results for the DM self-interaction applies to clusters with median maximum circular velocities in the range of approximately 1,400 km/s to 2,000 km/s. Since relative particle speeds are much lower in galaxies, the cross sections for dark matter interactions can be larger in galaxies, as many concrete particle physics models predict Tulin & Yu (2018).

The systematic error of the inference of cross section could be reduced if data were available for these clusters with more images and more complete spectroscopy, as this would in turn yield more accurate DM profiles. Cluster MACS 2129.4-0741 was an outlier in our results with regard to several characteristics (as was RXC J2248.7-4431, but to a lesser extent). More data and analysis of these clusters would be useful to help explain or mitigate those differences.

## ACKNOWLEDGEMENTS

We gratefully acknowledge a grant of computer time from XSEDE allocation TG-AST130007. QM was supported by NSF grant AST-1615306 and MK was supported by NSF grant PHY-1620638.

## REFERENCES

- Alvarez G., Yu H.-B., 2020, *Phys. Rev. D*, **101**, 043002
- Andrade K. E., Minor Q., Nierenberg A., Kaplinghat M., 2019, *Monthly Notices of the Royal Astronomical Society*, **487**, 1905
- Annunziatella M., et al., 2017, *The Astrophysical Journal*, **851**, 81
- Balberg S., Shapiro S. L., Inagaki S., 2002, *Astrophys. J.*, **568**, 475
- Belli S., Jones T., Ellis R. S., Richard J., 2013, *The Astrophysical Journal*, **772**, 141
- Bertin E., Arnouts S., 1996, *Astronomy and Astrophysics Supplement Series*, **117**, 393
- Boddy K. K., Kaplinghat M., Kwa A., Peter A. H., 2016, *Physical Review D*, **94**, 123017
- Bonamigo M., Despali G., Limousin M., Angulo R., Giocoli C., Soucail G., 2015, *Monthly Notices of the Royal Astronomical Society*, **449**, 3171
- Bonamigo M., et al., 2018, *The Astrophysical Journal*, **864**, 98
- Braaten E., Kang D., Laha R., 2018, *Journal of High Energy Physics*, **2018**, 84
- Bradač M., Allen S. W., Treu T., Ebeling H., Massey R., Morris R. G., von der Linden A., Applegate D., 2008, *The Astrophysical Journal*, **687**, 959
- Broadhurst T., Takada M., Umetsu K., Kong X., Arimoto N., Chiba M., Futamase T., 2005, *ApJ*, **619**, L143
- Caminha G. B., et al., 2016, *Astronomy and Astrophysics*, **587**
- Cerny C., et al., 2018, *The Astrophysical Journal*, **859**, 159
- Chabrier G., 2003, *Publications of the Astronomical Society of the Pacific*, **115**, 763
- Choi S.-M., Lee H. M., Seo M.-S., 2017, *Journal of High Energy Physics*, **2017**, 154
- Chu X., Garcia-Cely C., Murayama H., 2019, *Phys. Rev. Lett.*, **122**, 071103



- Chu X., Garcia-Cely C., Murayama H., 2020, *J. Cosmology Astropart. Phys.*, **2020**, 043
- Coe D., et al., 2012, *The Astrophysical Journal*, **757**, 22
- Currie M. J., Berry D. S., Jenness T., Gibb A. G., Bell G. S., Draper P. W., 2014, *Starlink Software in 2013*. p. 391
- Davis P. J., Rabinowitz P., 2007, *Methods of Numerical Integration: Second Edition* (Dover Books on Mathematics). Dover Publications
- Dawson W. A., et al., 2012, *Astrophysical Journal Letters*, **747**, 42
- Del Popolo A., 2012, *Monthly Notices of the Royal Astronomical Society*, **424**, 38
- Del Popolo A., 2014, *Journal of Cosmology and Astroparticle Physics*, **2014**, 019
- Desai V., 2004, PhD thesis, UNIVERSITY OF WASHINGTON
- Diemer B., 2018, *ApJS*, **239**, 35
- Diemer B., Joyce M., 2019, *The Astrophysical Journal*, **871**, 168
- Donnarumma A., Ettori S., Meneghetti M., Moscardini L., 2009, *Monthly Notices of the Royal Astronomical Society*, **398**, 438
- Donnarumma A., et al., 2011, *Astronomy & Astrophysics*, **528**, A73
- Dubois Y., Devriendt J., Slyz A., Teyssier R., 2010, *Monthly Notices of the Royal Astronomical Society*, **409**, 985
- Ebeling H., Barrett E., Donovan D., Ma C. J., Edge A. C., van Speybroeck L., 2007, *ApJ*, **661**, L33
- Elbert O. D., Bullock J. S., Garrison-Kimmel S., Rocha M., Oñorbe J., Peter A. H., 2015, *Monthly Notices of the Royal Astronomical Society*, **453**, 29
- Elíasdóttir A., et al., 2007, Technical report, Where is the Matter in the Merging Cluster Abell 2218? ([arXiv:0710.5636v1](https://arxiv.org/abs/0710.5636v1))
- Essig R., McDermott S. D., Yu H.-B., Zhong Y.-M., 2019, *Phys. Rev. Lett.*, **123**, 121102
- Feng J. L., Kaplinghat M., Yu H.-B., 2010, *Phys. Rev. D*, **82**, 083525
- Feroz F., Hobson M. P., Bridges M., 2009, *Monthly Notices of the Royal Astronomical Society*, **398**, 1601
- Fielder C. E., Mao Y.-Y., Zentner A. R., Newman J. A., Wu H.-Y., Wechsler R. H., 2020, *Monthly Notices of the Royal Astronomical Society*, **499**, 2426–2444
- Gao L., Navarro J. F., Frenk C. S., Jenkins A., Springel V., White S. D. M., 2012, *Monthly Notices of the Royal Astronomical Society*, **425**, 2169
- Golse G., Kneib J.-P. J.-P., 2002, *A&A*, **390**, 821
- Harvey D., Massey R., Kitching T., Taylor A., Tittle E., 2015, *Science*, **347**, 1462
- Harvey D., Robertson A., Massey R., McCarthy I. G., 2019, *Monthly Notices of the Royal Astronomical Society*, **488**, 1572
- He Q., et al., 2020, *Monthly Notices of the Royal Astronomical Society*, **496**, 4717
- Higson E., Handley W., Hobson M., Lasenby A., 2019, *Statistics and Computing*, **29**, 891
- Hochberg Y., Kuflik E., Murayama H., Volansky T., Wacker J. G., 2015, *Phys. Rev. Lett.*, **115**, 021301
- Kahlhoefer F., Schmidt-Hoberg K., Frandsen M. T., Sarkar S., 2014, *Monthly Notices of the Royal Astronomical Society*, **437**, 2865
- Kaplinghat M., Keeley R. E., Linden T., Yu H. B., 2014, *Physical Review Letters*, **113**
- Kaplinghat M., Tulin S., Yu H. B., 2016, *Physical Review Letters*, **116**, 041302
- Keeton C. R., 2001, Technical report, A Catalog of Mass Models for Gravitational Lensing, <http://arxiv.org/abs/astro-ph/0102341>. ([arXiv:0102341](https://arxiv.org/abs/0102341)), <http://arxiv.org/abs/astro-ph/0102341>
- Kim S. Y., Peter A. H., Wittman D., 2017, *Monthly Notices of the Royal Astronomical Society*, **469**, 1414
- Kneib J.-P., et al., 2003, *ApJ*, **598**, 804
- Limousin M., Kneib J.-P. P., Natarajan P., 2004, *Mon. Not. R. Astron. Soc.*, **000**, 1
- Limousin M., Kneib J. P., Bardeau S., Natarajan P., Czoske O., Smail I., Ebeling H., Smith G. P., 2007a, *Astronomy & Astrophysics*, **461**, 881
- Limousin M., et al., 2007b, *The Astrophysical Journal*, **668**, 643
- Loeb A., Weiner N., 2011, *Physics Review Letters*, **106**, 171302
- Mandelbaum R., Seljak U., Cool R. J., Blanton M., Hirata C. M., Brinkmann J., 2006, *MNRAS*, **372**, 758
- Mann A. W., Ebeling H., 2012, *Monthly Notices of the Royal Astronomical Society*, **420**, 2120
- Marinacci F., et al., 2018, *Monthly Notices of the Royal Astronomical Society*
- Martizzi D., Teyssier R., Moore B., Wentz T., 2012, *Monthly Notices of the Royal Astronomical Society*, **422**, 3081
- Martizzi D., Teyssier R., Moore B., 2013, *MNRAS*, **432**, 1947
- Meneghetti M., Fedeli C., Pace F., Gottlöber S., Yepes G., 2010, *Astronomy and Astrophysics*, **519**, A90
- Merten J., et al., 2011, *Monthly Notices of the Royal Astronomical Society*, **417**, 333
- Merten J., et al., 2015, *ApJ*, **806**, 4
- Miralda-Escude J., 1995, *ApJ*, **438**, 514
- Monna A., et al., 2015, *Monthly Notices of the Royal Astronomical Society*, **447**, 1224
- Monna A., et al., 2017, *Monthly Notices of the Royal Astronomical Society*, **466**, 4094
- Naiman J. P., et al., 2018, *Monthly Notices of the Royal Astronomical Society*, **477**, 1206–1224
- Natarajan P., Kneib J.-P., 1996, *MNRAS*, **283**, 1031
- Navarro J. F., Frenk C. S., White S. D. M., 1996, *The Astrophysical Journal*, **462**, 563
- Nelson D., et al., 2017, *Monthly Notices of the Royal Astronomical Society*, **475**, 624–647
- Nelson D., et al., 2018, The IllustrisTNG Simulations: Public Data Release ([arXiv:1812.05609](https://arxiv.org/abs/1812.05609))
- Newman A. B., Treu T., Ellis R. S., Sand D. J., Richard J., Marshall P. J., Capak P., Miyazaki S., 2009, *The Astrophysical Journal*, **706**, 1078
- Newman A. B., Treu T., Ellis R. S., Sand D. J., 2011, *The Astrophysical Journal Letters*, **728**, 39
- Newman A. B., Treu T., Ellis R. S., Sand D. J., Nipoti C., Richard J., Jullo E., 2013a, *The Astrophysical Journal*, **765**, 24
- Newman A. B., Treu T., Ellis R. S., Sand D. J., 2013b, *The Astrophysical Journal*, **765**, 25
- Niemiec A., et al., 2017, *Monthly Notices of the Royal Astronomical Society*, **471**, 1153–1166
- Nishikawa H., Boddy K. K., Kaplinghat M., 2020, *Phys. Rev. D*, **101**, 063009
- Okabe N., Takada M., Umetsu K., Futamase T., Smith G. P., 2010, *PASJ*, **62**, 811
- Pedregosa F., et al., 2011, *Journal of Machine Learning Research*, **12**, 2825
- Peirani S., et al., 2017, *Monthly Notices of the Royal Astronomical Society*, **472**, 2153–2169
- Peñarrubia J., Pontzen A., Walker M., Koposov S., 2012, *The Astrophysical Journal*, **759**, L42
- Pillepich A., et al., 2017, *Monthly Notices of the Royal Astronomical Society*, **475**, 648–675
- Pontzen A., Governato F., 2012, *Monthly Notices of the Royal Astronomical Society*, **421**, 3464
- Postman M., et al., 2012, *The Astrophysical Journal Supplement Series*, **199**, 25
- Ragone-Figueroa C., Granato G. L., Abadi M. G., 2012, *Monthly Notices of the Royal Astronomical Society*, **423**, 3243
- Randall S. W., Markevitch M., Clowe D., Gonzalez A. H., Bradač M., 2008, *The Astrophysical Journal*, **679**, 1173
- Ren T., Kwa A., Kaplinghat M., Yu H. B., 2019, *Physical Review X*, **9**
- Richard J., et al., 2010, *Monthly Notices of the Royal Astronomical Society*, **404**, 325
- Robertson A., Massey R., Eke V., 2017a, *Monthly Notices of the Royal Astronomical Society*, **465**, 569
- Robertson A., Massey R., Eke V., 2017b, *Monthly Notices of the Royal Astronomical Society*, **467**, 4719
- Robertson A., Massey R., Eke V., Schaye J., Theuns T., 2020, *arXiv e-prints*, [p. arXiv:2009.07844](https://arxiv.org/abs/2009.07844)
- Robles V. H., Kelley T., Bullock J. S., Kaplinghat M., 2019, *MNRAS*, **490**, 2117
- Rocha M., Peter A. H., Bullock J. S., Kaplinghat M., Garrison-kimmel S., Oñorbe J., Moustakas L. A., 2013a, *Monthly Notices of the Royal*

- Astronomical Society*, 430, 81
- Rocha M., Peter A. H., Bullock J. S., Kaplinghat M., Garrison-kimmel S., Oñorbe J., Moustakas L. A., 2013b, *Monthly Notices of the Royal Astronomical Society*, 430, 81
- Sagunski L., Gad-Nasr S., Colquhoun B., Robertson A., Tulin S., 2020, Velocity-dependent Self-interacting Dark Matter from Groups and Clusters of Galaxies ([arXiv:2006.12515](#))
- Salpeter E. E., 1955, *The Astrophysical Journal*, 121, 161
- Sand D., Treu T., Ellis R., 2002, in American Astronomical Society Meeting Abstracts. p. 58.07
- Sand D. J., Treu T., Smith G. P., Ellis R. S., 2004, *The Astrophysical Journal*, 604, 88
- Sand D. J., Treu T., Ellis R. S., Smith G. P., Kneib J., 2008, *The Astrophysical Journal*, 674, 711
- Schaller M., et al., 2015, *Monthly Notices of the Royal Astronomical Society*, 452, 343
- Schaye J., et al., 2015, *MNRAS*, 446, 521
- Schmidt R. W., Allen S. W., 2007, *Monthly Notices of the Royal Astronomical Society*, 379, 209
- Schramm T., 1990, *Jap*, 231, 19
- Sereno M., Giocoli C., Ettori S., Moscardini L., 2015, *Monthly Notices of the Royal Astronomical Society*, 449, 2024–2039
- Sokolenko A., Bondarenko K., Brinckmann T., Zavala J., Vogelsberger M., Bringmann T., Boyarsky A., 2018, *JCAP*, 12, 038
- Speagle J. S., 2020, *Monthly Notices of the Royal Astronomical Society*, 493, 3132
- Spergel D. N., Steinhardt P. J., 2000, *Physical Review Letters*, 84, 3760
- Springel V., et al., 2018, *MNRAS*, 475, 676
- Tempel E., Libeskind N. I., 2013, *Astrophysical Journal Letters*, 775, 42
- Teyssier R., Moore B., Martizzi D., Dubois Y., Mayer L., 2011, *Monthly Notices of the Royal Astronomical Society*, 414, 195
- Tulin S., Yu H. B., 2018, Dark matter self-interactions and small scale structure ([arXiv:1705.02358](#)), doi:10.1016/j.physrep.2017.11.004
- Tulin S., Yu H. B., Zurek K. M., 2013a, *Physical Review D - Particles, Fields, Gravitation and Cosmology*, 87
- Tulin S., Yu H. B., Zurek K. M., 2013b, *Physical Review D - Particles, Fields, Gravitation and Cosmology*, 87, 115007
- Umetsu K., Broadhurst T., Zitrin A., Medezinski E., Hsu L.-Y., 2011, *The Astrophysical Journal*, 729, 127
- Vogelsberger M., Zavala J., Loeb A., 2012, *Monthly Notices of the Royal Astronomical Society*, 423, 3740
- Vogelsberger M., et al., 2014, *Nature*, 509, 177
- Vogelsberger M., Zavala J., Schutz K., Slatyer T. R., 2019, *Monthly Notices of the Royal Astronomical Society*, 484, 5437
- Voigt L. M., Bridle S. L., 2010, *Monthly Notices of the Royal Astronomical Society*, 404, 458
- Zavala J., Vogelsberger M., Walker M., 2013, *Monthly Notices of the Royal Astronomical Society*, 431, L20
- Zitrin A., et al., 2011, *ApJ*, 742, 117
- Zitrin A., Menanteau F., Hughes J. P., Coe D., Barrientos L. F., Infante L., Mandelbaum R., 2013, *The Astrophysical Journal*, 770, L15
- Zitrin A., et al., 2015, *The Astrophysical Journal*, 801, 44

## APPENDIX A: RELEVANT LENSING FORMULAS FOR THE CNFW HALO MODEL

The cNFW (cNFW) model is defined by modifying the NFW profile as follows:

$$\rho = \frac{\rho_s r_s^3}{(r_c + r)(r_s + r)^2}. \quad (\text{A1})$$

Defining  $x = r/r_s$  and  $\beta = r_c/r_s$ , by integrating the density

profile along the line of sight we find an analytic expression for the projected density profile,

$$\kappa(x) = \frac{2\kappa_s}{(\beta-1)^2} \left\{ \frac{1}{x^2-1} \left[ 1 - \beta - (1-x^2\beta)\mathcal{F}(x) \right] - \mathcal{F}\left(\frac{x}{\beta}\right) \right\} \quad (\text{A2})$$

, where we have defined  $\kappa_s = \rho_s r_s / \Sigma_{cr}$ , and

$$\mathcal{F}(x) = \begin{cases} \frac{1}{\sqrt{x^2-1}} \tan^{-1} \sqrt{x^2-1} & (x > 1) \\ \frac{1}{\sqrt{1-x^2}} \tanh^{-1} \sqrt{1-x^2} & (x < 1) \\ 1 & (x = 1) \end{cases} \quad (\text{A3})$$

When using the pseudo-elliptical approximation, it is useful to have an analytic formula for the deflection angle generated by a spherical cNFW lens. By integrating Equation A2, we obtain

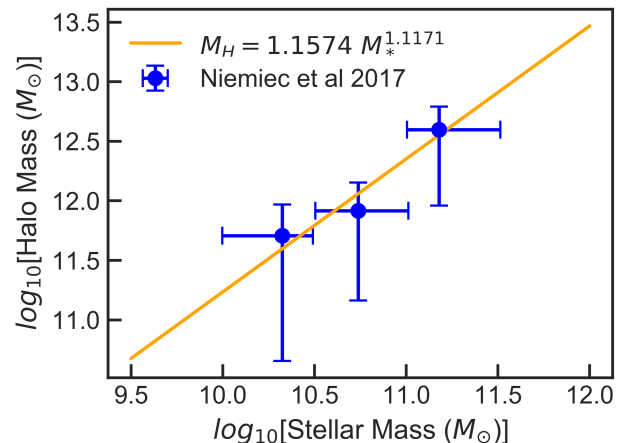
$$\alpha(x) = \frac{2\kappa_s r_s}{(1-\beta)^2 x} \left\{ (1-\beta)^2 \ln\left(\frac{x^2}{4}\right) - \beta^2 \ln \beta^2 + 2(\beta^2 - x^2)\mathcal{F}\left(\frac{x}{\beta}\right) + 2[1 + \beta(x^2 - 2)]\mathcal{F}(x) \right\}. \quad (\text{A5})$$

It can be easily verified that in the limit  $\beta \rightarrow 0$ , these formulae reduce to the usual analytic formulas for an NFW profile (Golse & Kneib 2002). Numerical convergence of these formulae becomes difficult in the neighborhood of either  $x \approx \beta$ ,  $x \approx 1$  or  $\beta \approx 1$ ; in each of these cases, series expansions can be used for greater accuracy, all of which have been implemented and tested in the *QLens* code.

## APPENDIX B: STELLAR MASS–HALO MASS RELATION

Niemiec et al. (2017) examined the stellar mass–halo mass relation for cluster galaxies. A power law fit to their data is shown in Figure B1. The resulting power law is  $M_{\text{halo}} = 1.1574 M_*^{1.1171}$ .

**Figure B1.** Stellar mass–halo mass data from Niemiec et al. (2017), and the best fit power law which was used to determine the mass for DM subhalos in the lens models.



### APPENDIX C: CONCENTRATION BIAS IN TRIAXIAL HALOS

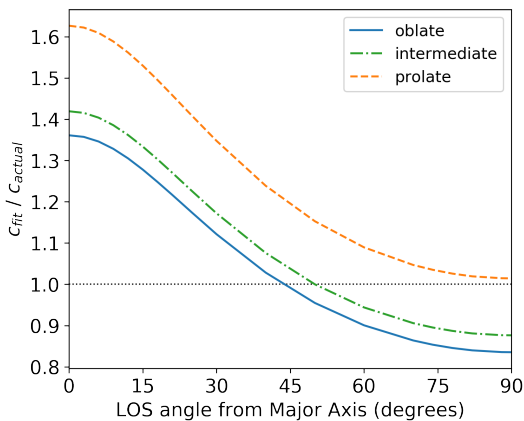
Since strong lensing analysis is based on 2-D projections of 3-D bodies, effectively hiding one dimension from direct measurement, biases can arise in model parameters such as concentration and scale radius. Halo elongation parallel (perpendicular) to the line of sight can increase (decrease) the strength of the lensing. Moreover, alignment of the major axis with the line of sight has shown to increase as lensing cross section increases, and leads to an upward bias in concentration (Meneghetti et al. 2010).

Galaxies and galaxy clusters are thought to form along filaments of the cosmic web. The major axis of elliptical galaxies tend to be parallel to the direction of the host filament (Tempel & Libeskind 2013). In cosmological N-body simulations, prolate halos are more common than oblate ones, especially so for massive halos (Bonamigo et al. 2015). We therefore expect the preponderance of our sample to be prolate halos with their major axis oriented preferentially along the line of sight, creating significant upward bias in concentration. To quantify the effect of concentration bias in our modeling pipeline, we created simulated triaxial halos, projected them in various orientations, and fitted the resulting 2D shapes with our fitting code. The simulated halos were NFW ellipsoids, with triaxiality introduced by scaling the x, y and z axes by factors a, b and c. The triaxiality is thus defined by the ellipsoid with form

$$\frac{x^2}{a^2} + \frac{y^2}{b^2} + \frac{z^2}{c^2} = 1. \quad (C1)$$

For the oblate case, we chose  $a = 0.5$ ,  $b = c = 1.0$ . For the intermediate case,  $a = 0.5$ ,  $b = 0.75$ ,  $c = 1.0$ . The prolate case used  $a = b = 0.5$ ,  $c = 1.0$ . Thus the z-axis is the major axis in all cases. Figure C1 shows the results of that analysis. Biases in concentration range from approximately +60% to -20%. The strongest bias of  $\sim +60\%$  occurs in the common case of prolate halos with major axis orientation nearly along the line of sight. We therefore expect that our modeled concentrations are often biased high by as much as 60%.

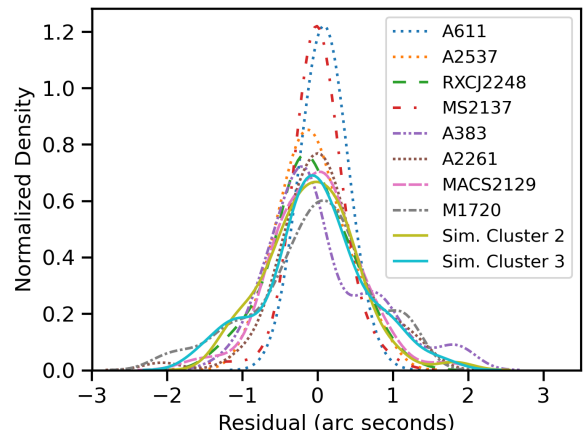
**Figure C1.** Bias in concentration when fitting 2-D projections of triaxial halos. The bias is  $\sim +60\%$  for prolate halos oriented along the LOS.



### APPENDIX D: STRONG LENSING ERROR RESIDUALS

In the Figure D1 we show the distribution of residual errors in image locations from the strong lensing analysis. For the simulated clusters, random Gaussian error of  $0''.50$  was added to each of the x and y components, resulting in a total position error of  $0''.71$ . In the strong lensing  $\chi^2$ , we have again assumed image position errors of  $0''.50$  for each of the x and y components. The figure demonstrates that the image position errors are distributed in a Gaussian shape, as would be expected for measurement errors.

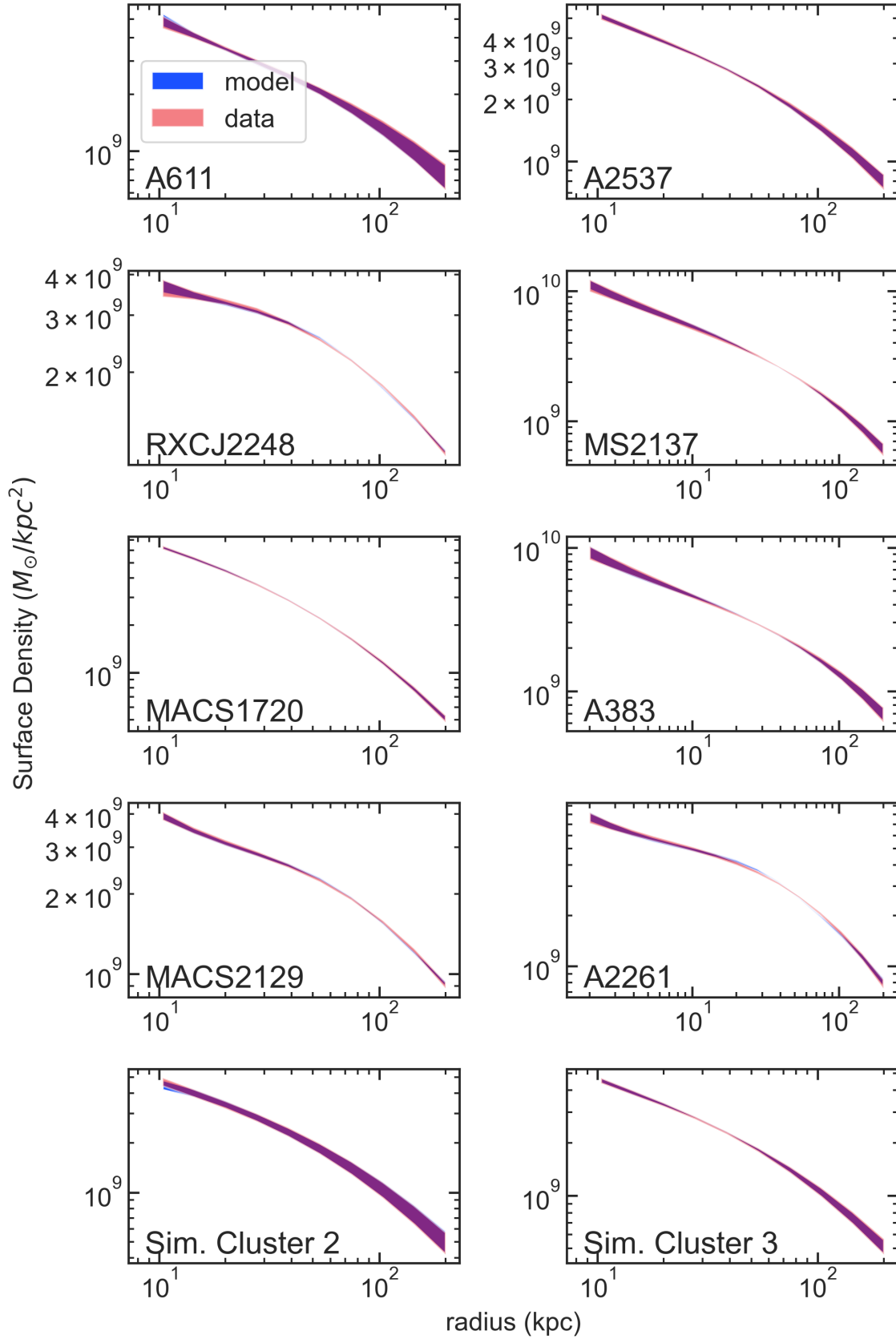
**Figure D1.** Residual position errors in image locations from strong lensing. Both the x and y error components are included; positive residuals mean errors in the westerly direction for x-components and the northerly direction for y-components.



**APPENDIX E: SURFACE DENSITY MATCH BETWEEN  
STRONG LENSING AND SIDM MODELS**

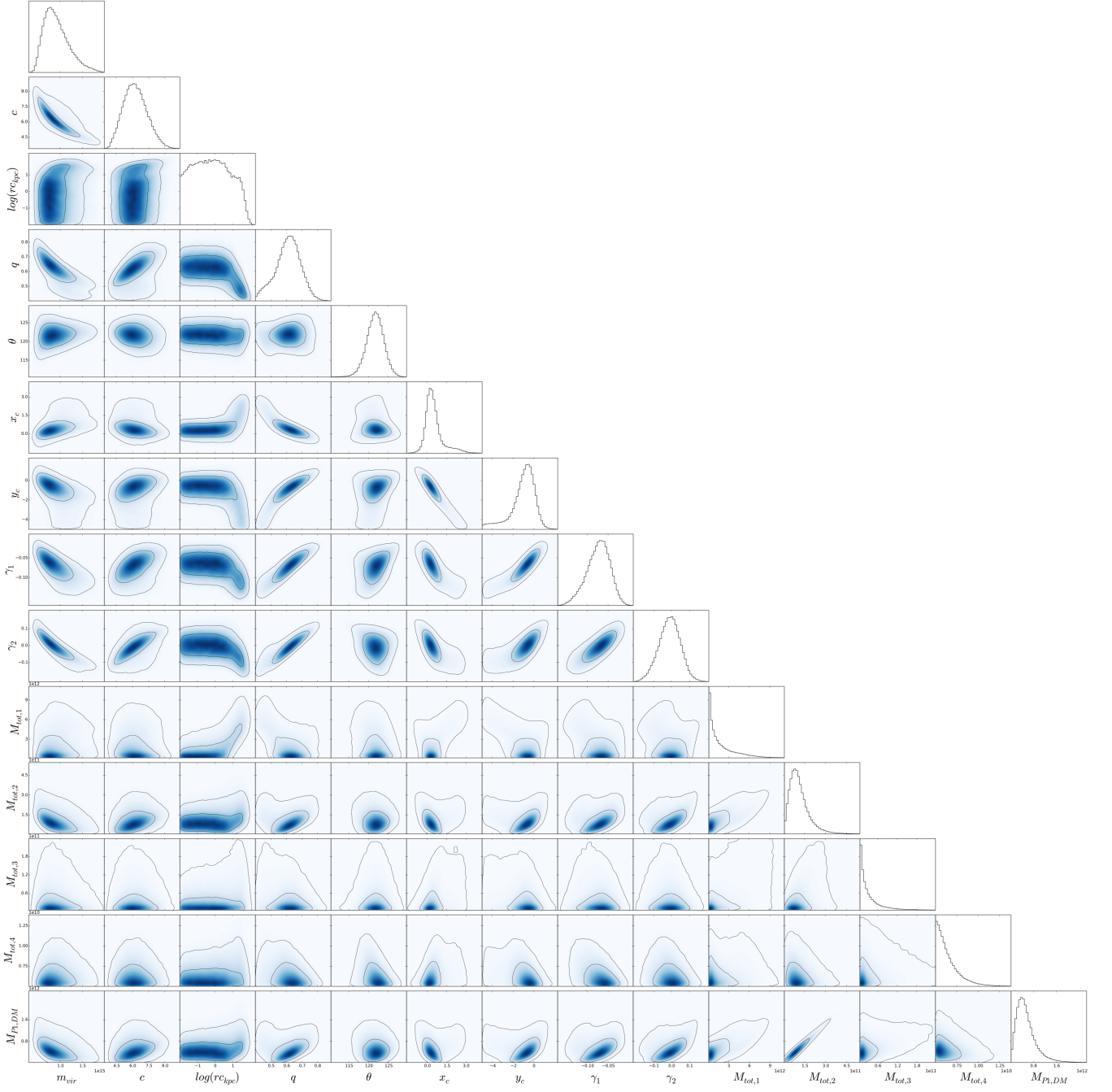


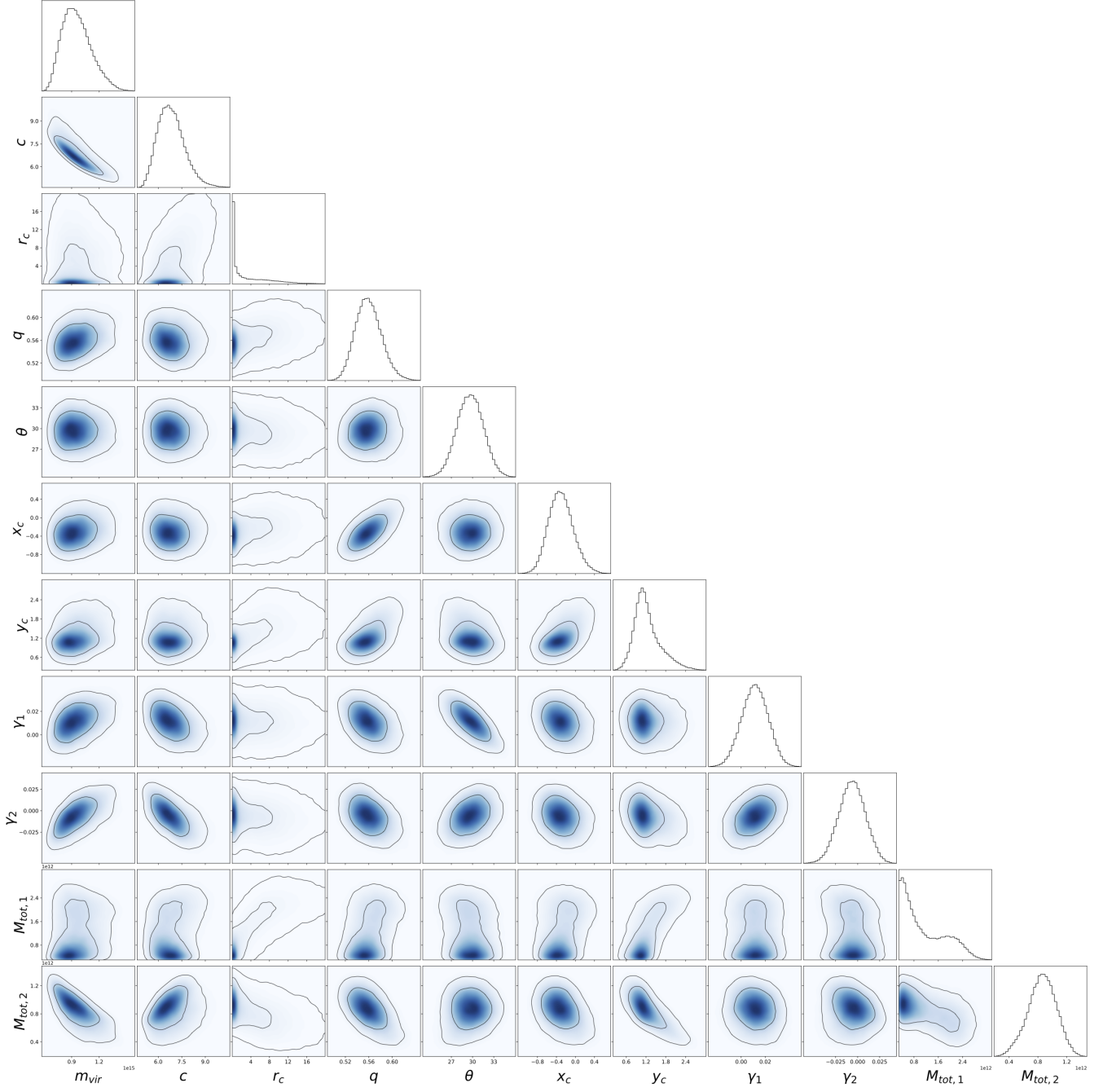
**Figure E1.** Plots of the 68% confidence intervals for strong lensing ("data") and SIDM ("model") surface densities for each cluster. The model is shown in blue and the data in red, and the regions appear purple where they overlap.



**APPENDIX F: POSTERIOR DISTRIBUTIONS FOR  
STRONG LENSING**

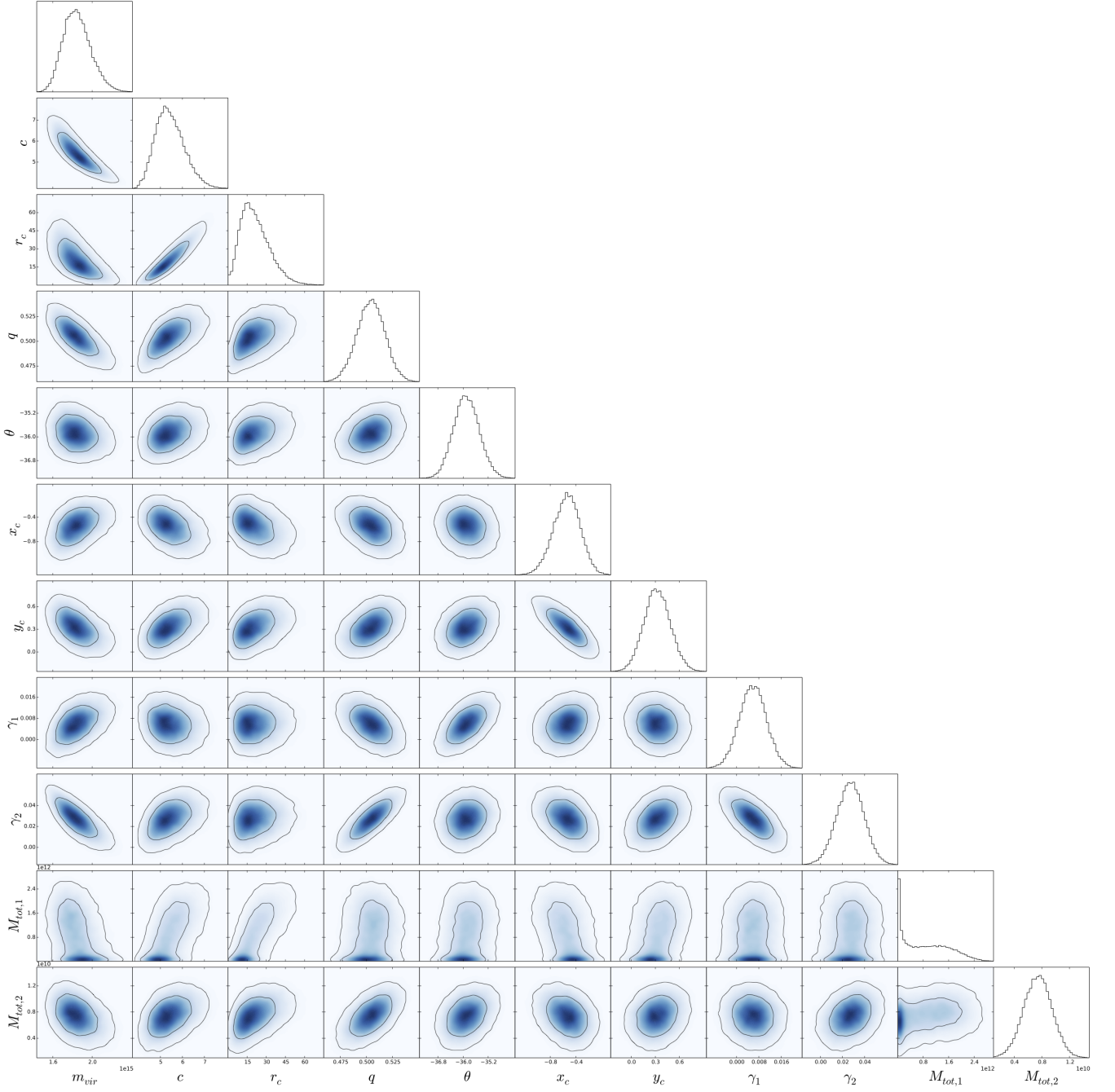
**Figure F1.** Abell 611 strong lensing posteriors.

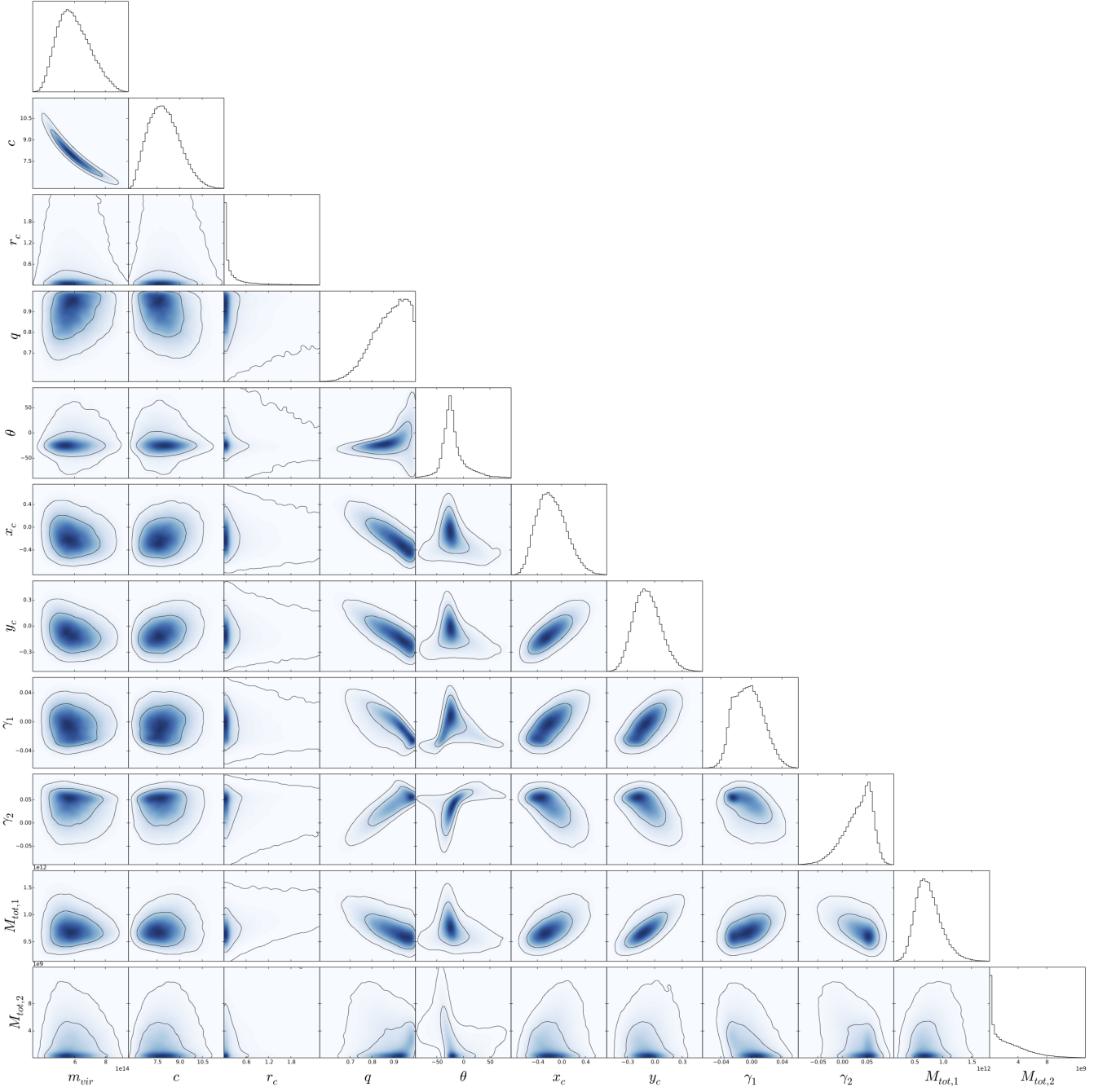


**Figure F2.** Abell 2537 strong lensing posteriors.

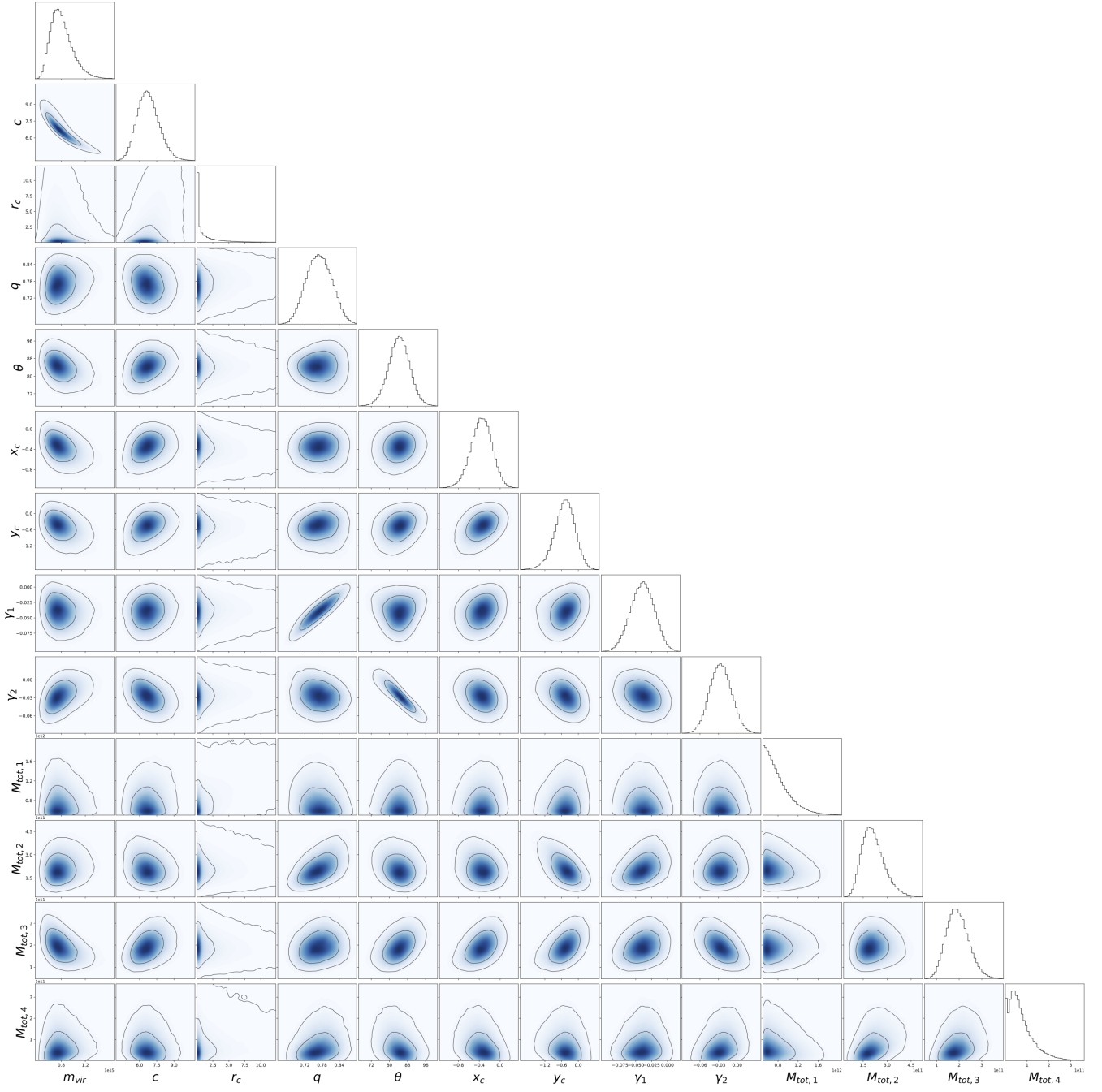


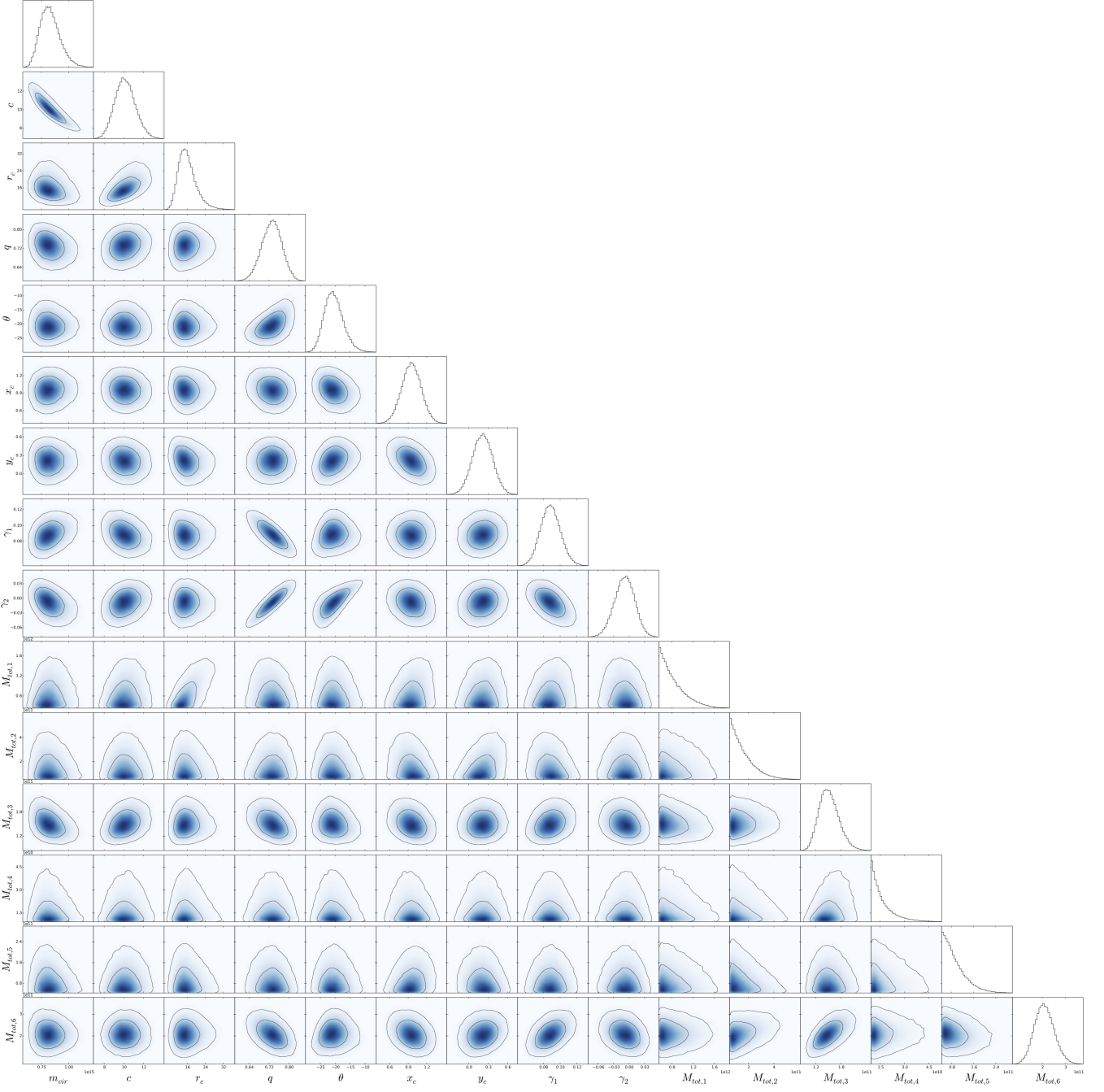
**Figure F3.** RXCJ2248 strong lensing posteriors.



**Figure F4.** MS2137 strong lensing posteriors.

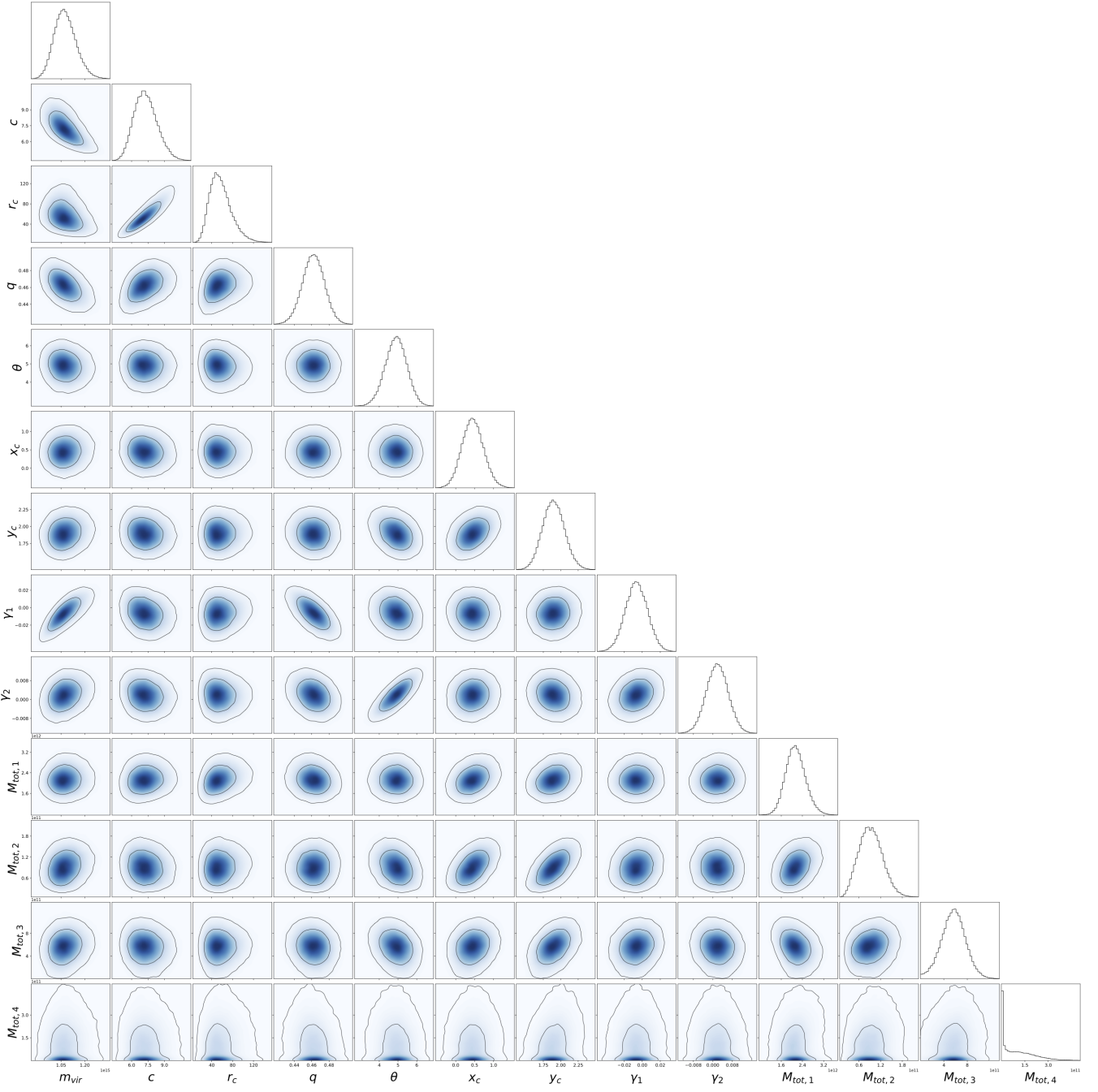
**Figure F5.** Abell 383 strong lensing posteriors.

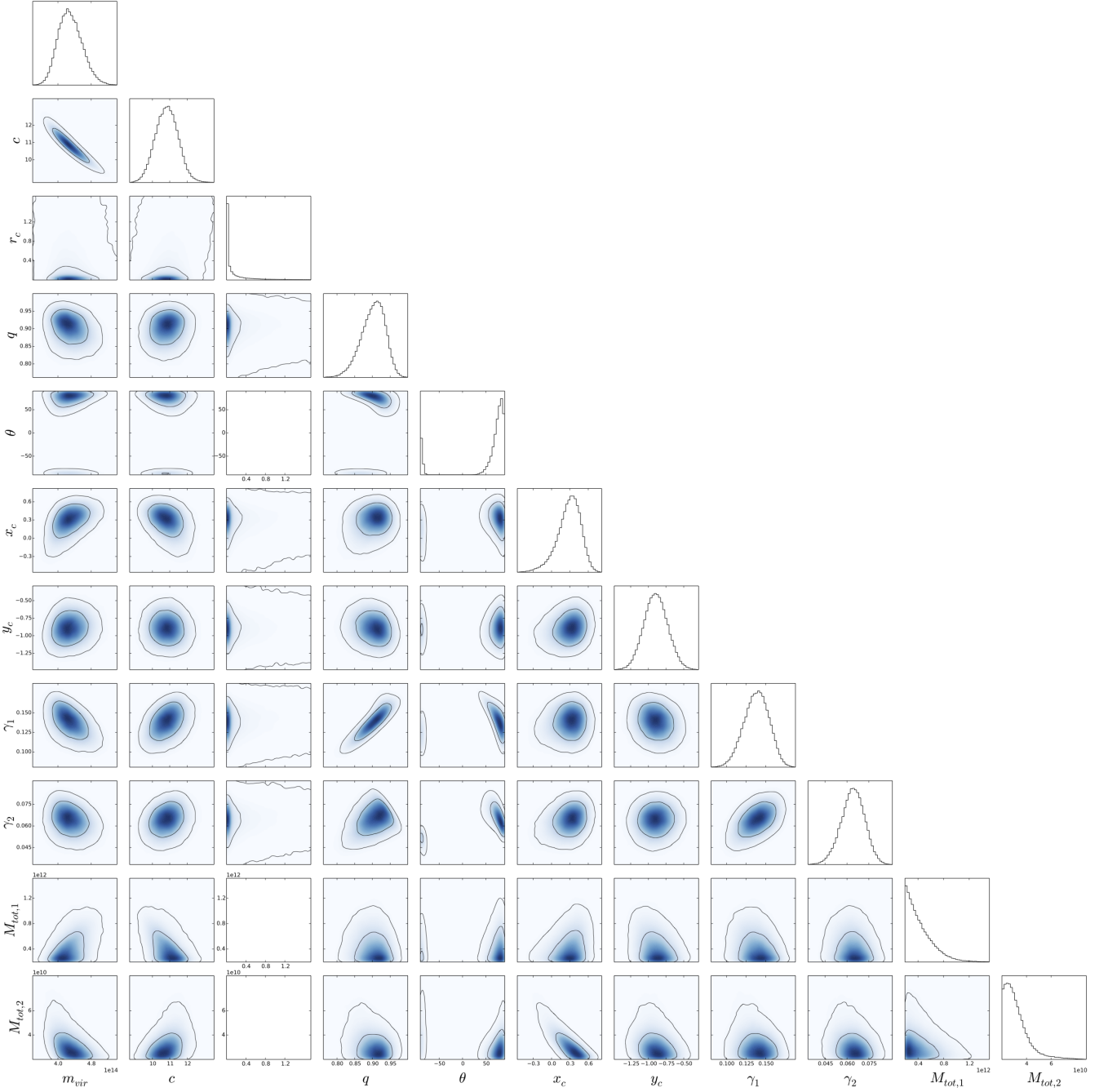


**Figure F6.** Abell 2261 strong lensing posteriors.

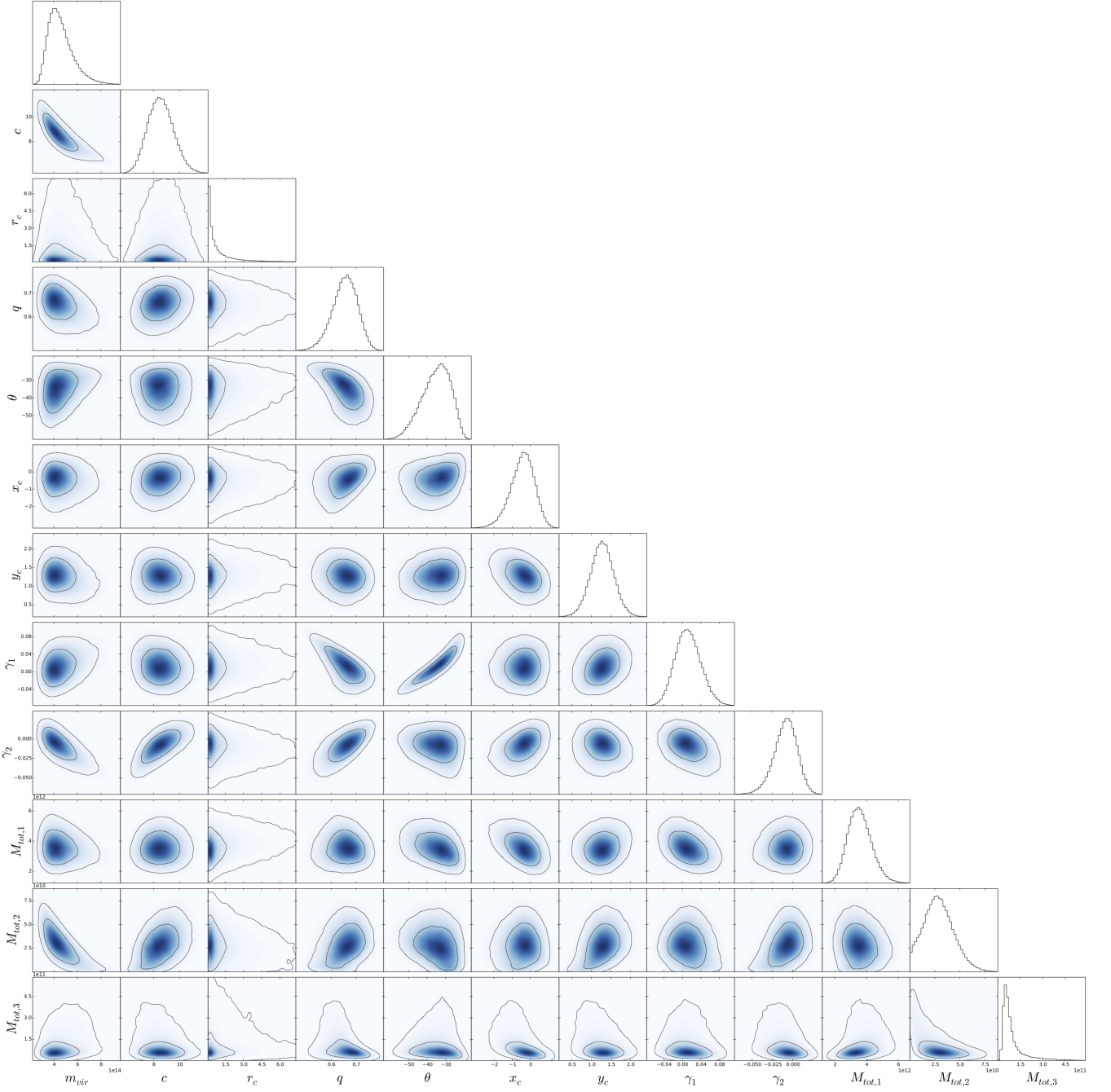


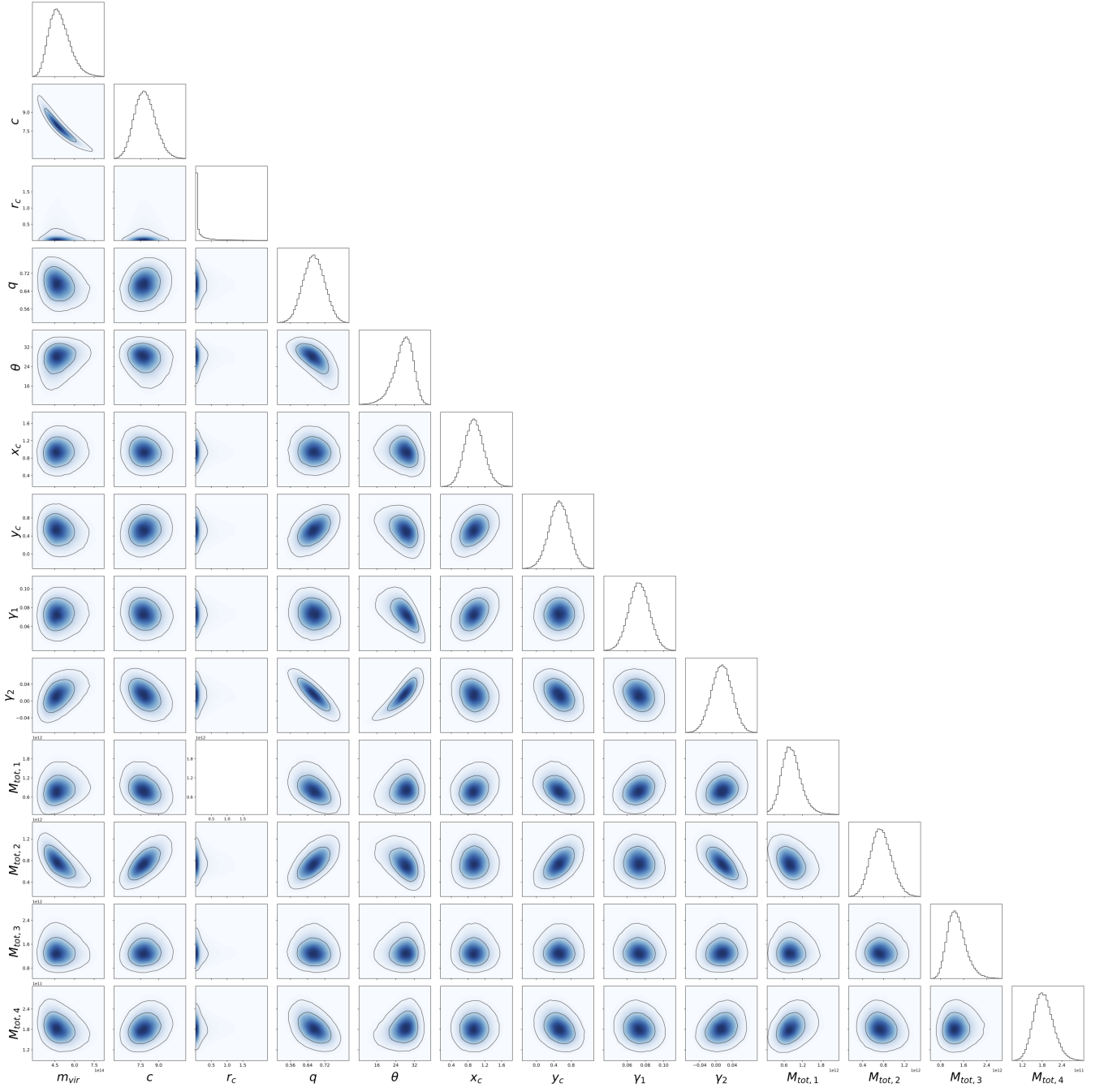
**Figure F7.** MACS2129 strong lensing posteriors.



**Figure F8.** MACS1720 strong lensing posteriors.

**Figure F9.** Sim. Cluster 2 strong lensing posteriors.



**Figure F10.** Sim. Cluster 3 strong lensing posteriors.

**APPENDIX G: POSTERIOR DISTRIBUTIONS FOR THE  
SIDM HALO MATCHING MODEL**



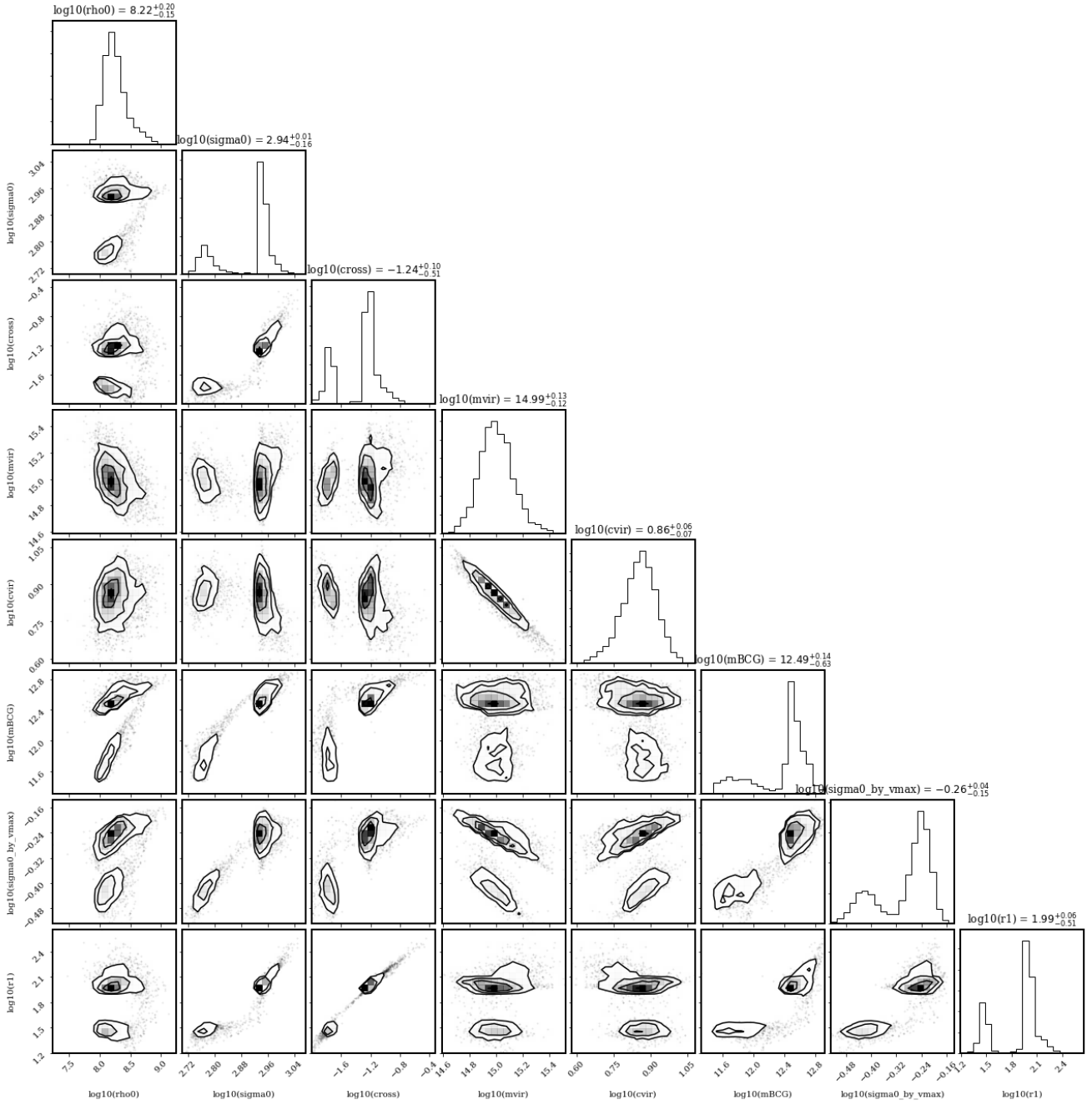
**Figure G1.** Abell 611 SIDM Halo Matching posteriors.

Figure G2. Abell 2537 SIDM Halo Matching posteriors.

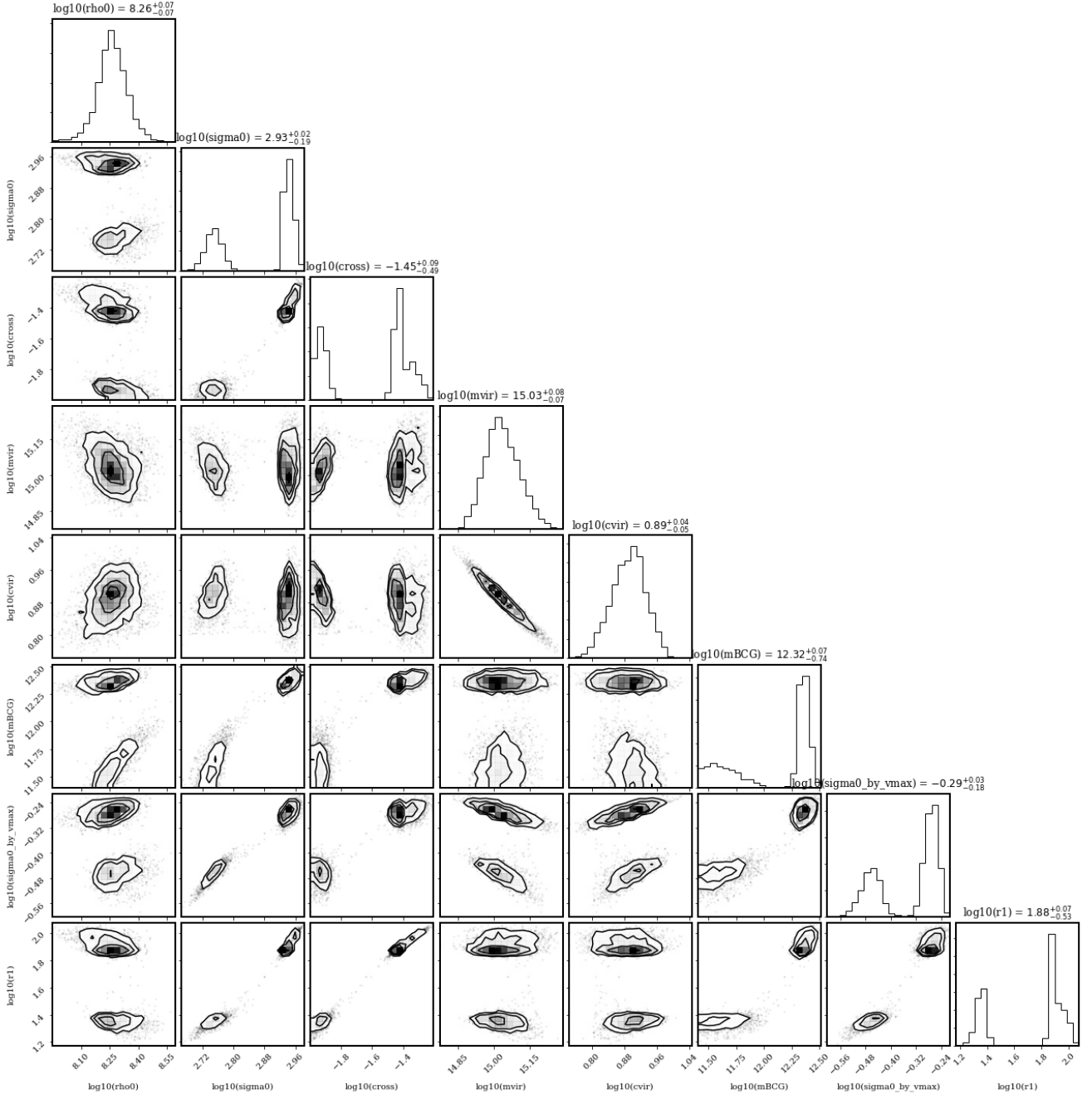


Figure G3. RXCJ2248 SIDM Halo Matching posteriors.

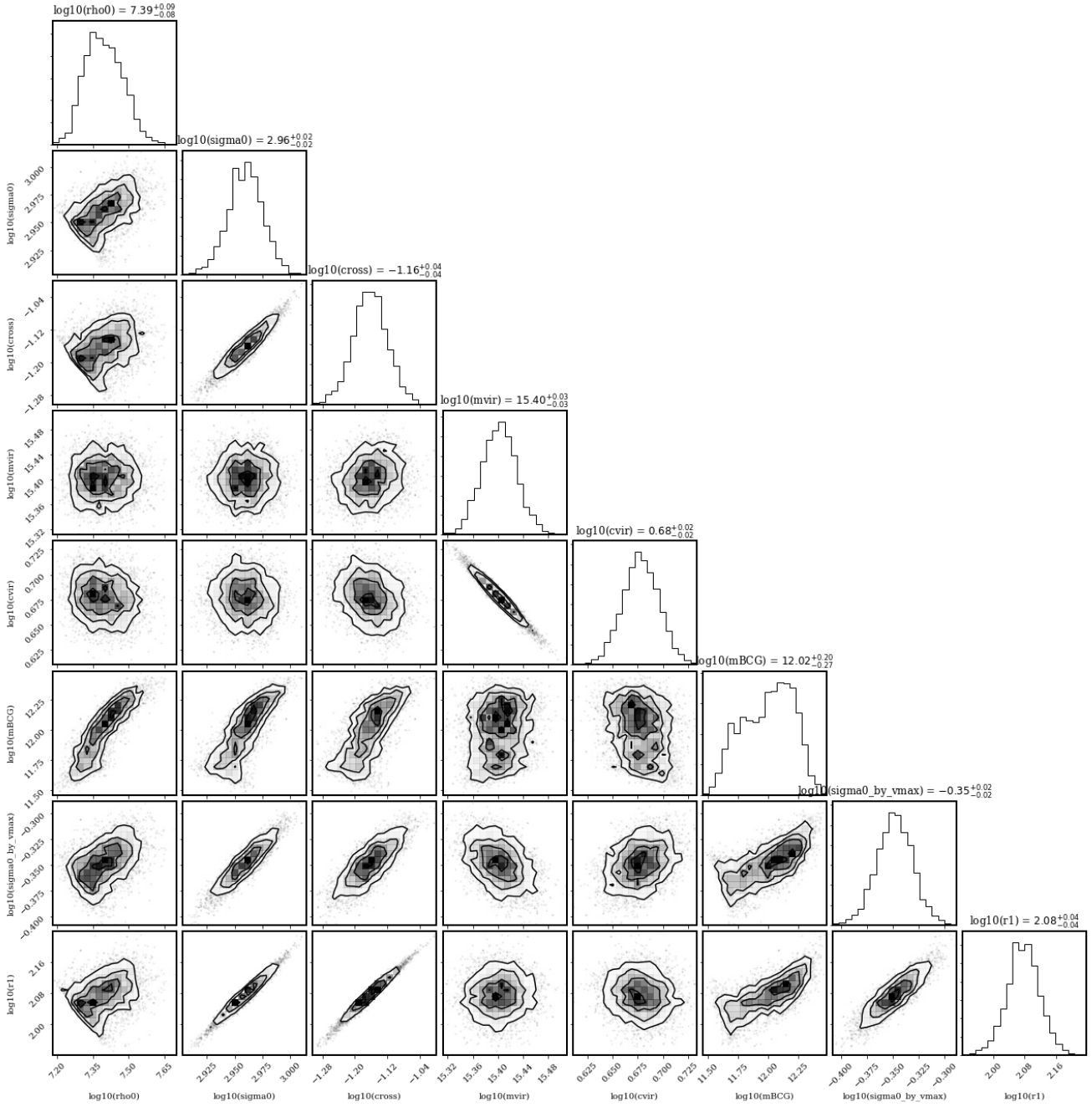
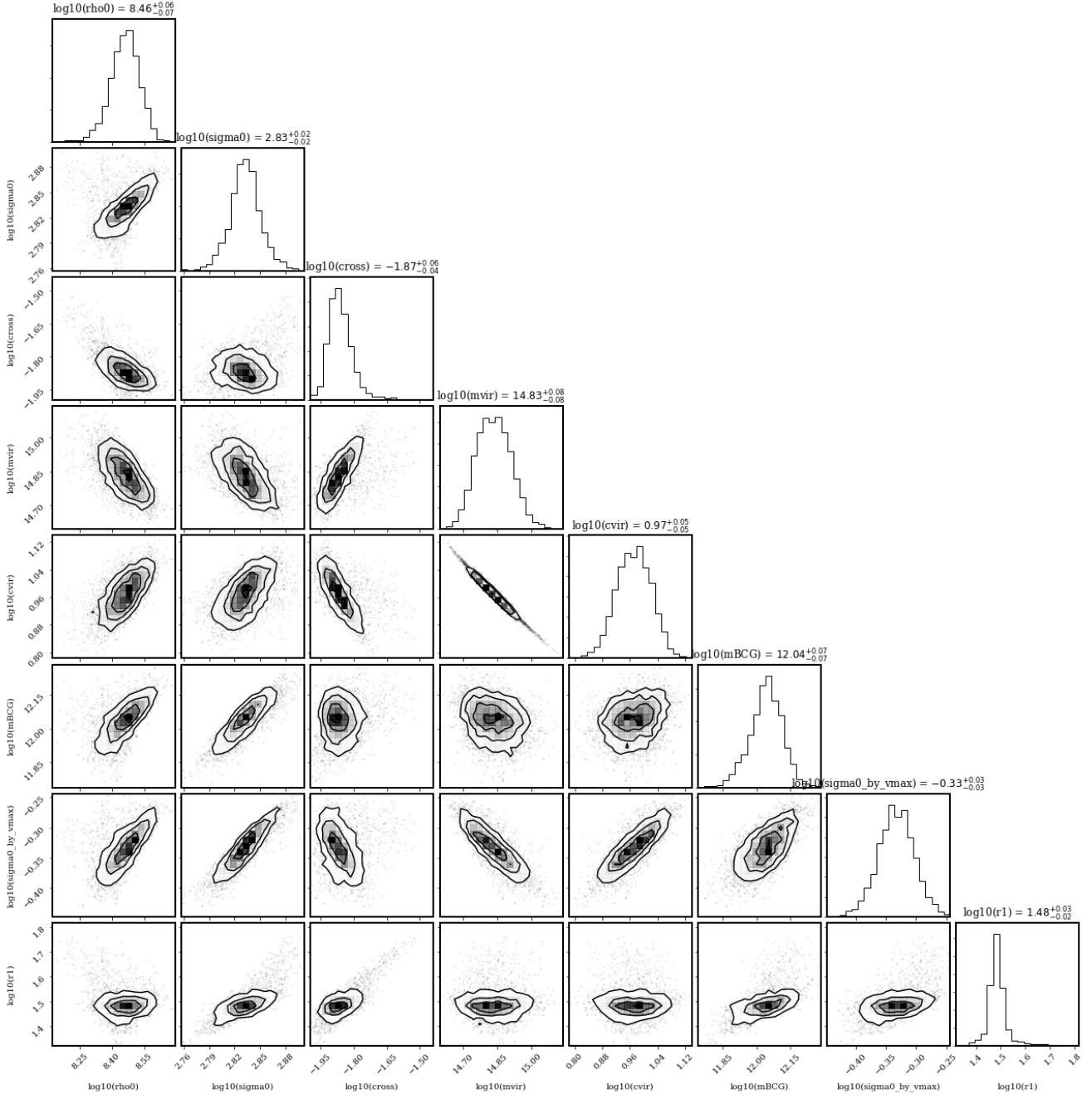


Figure G4. MS2137 SIDM Halo Matching posteriors.



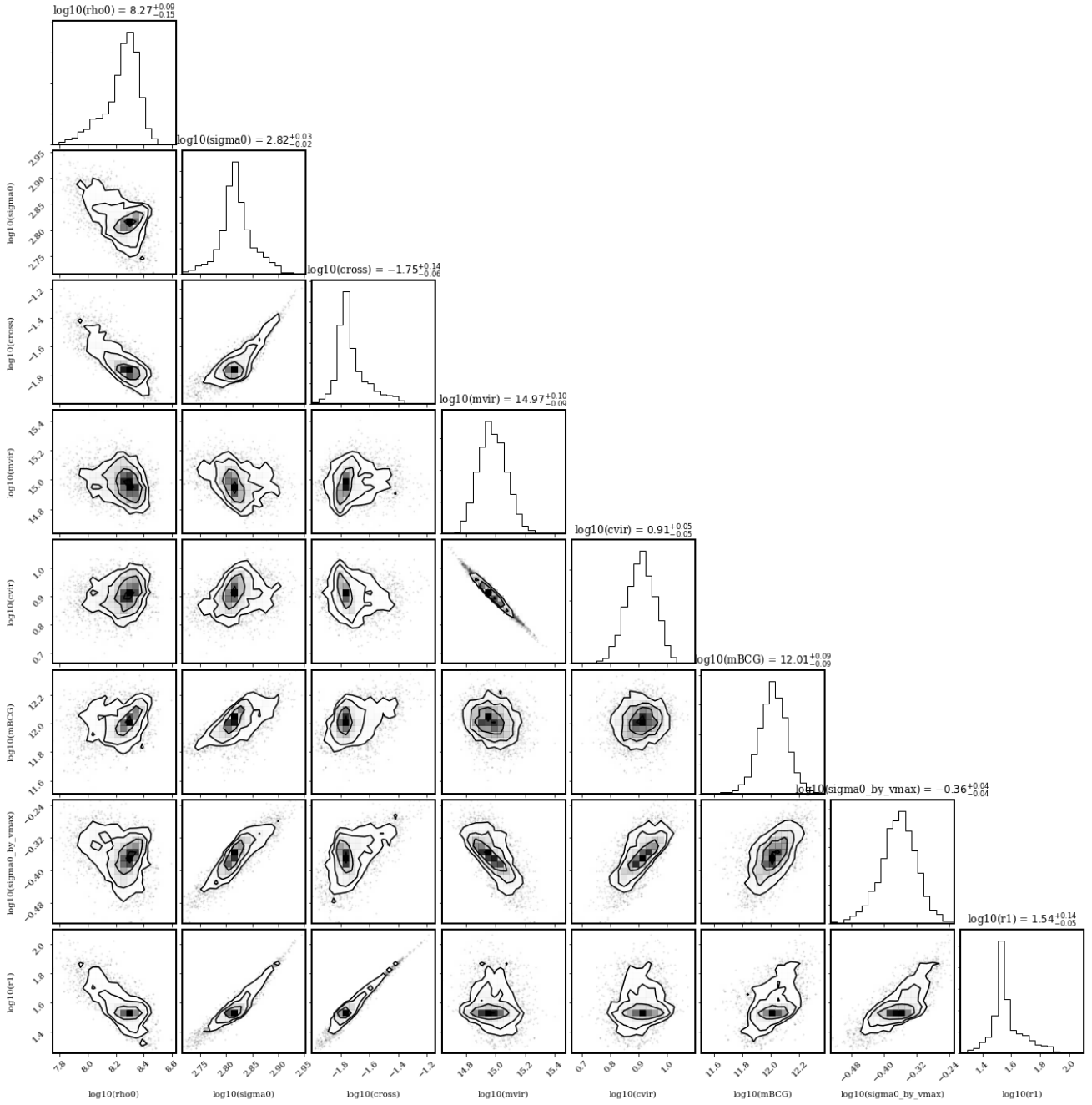
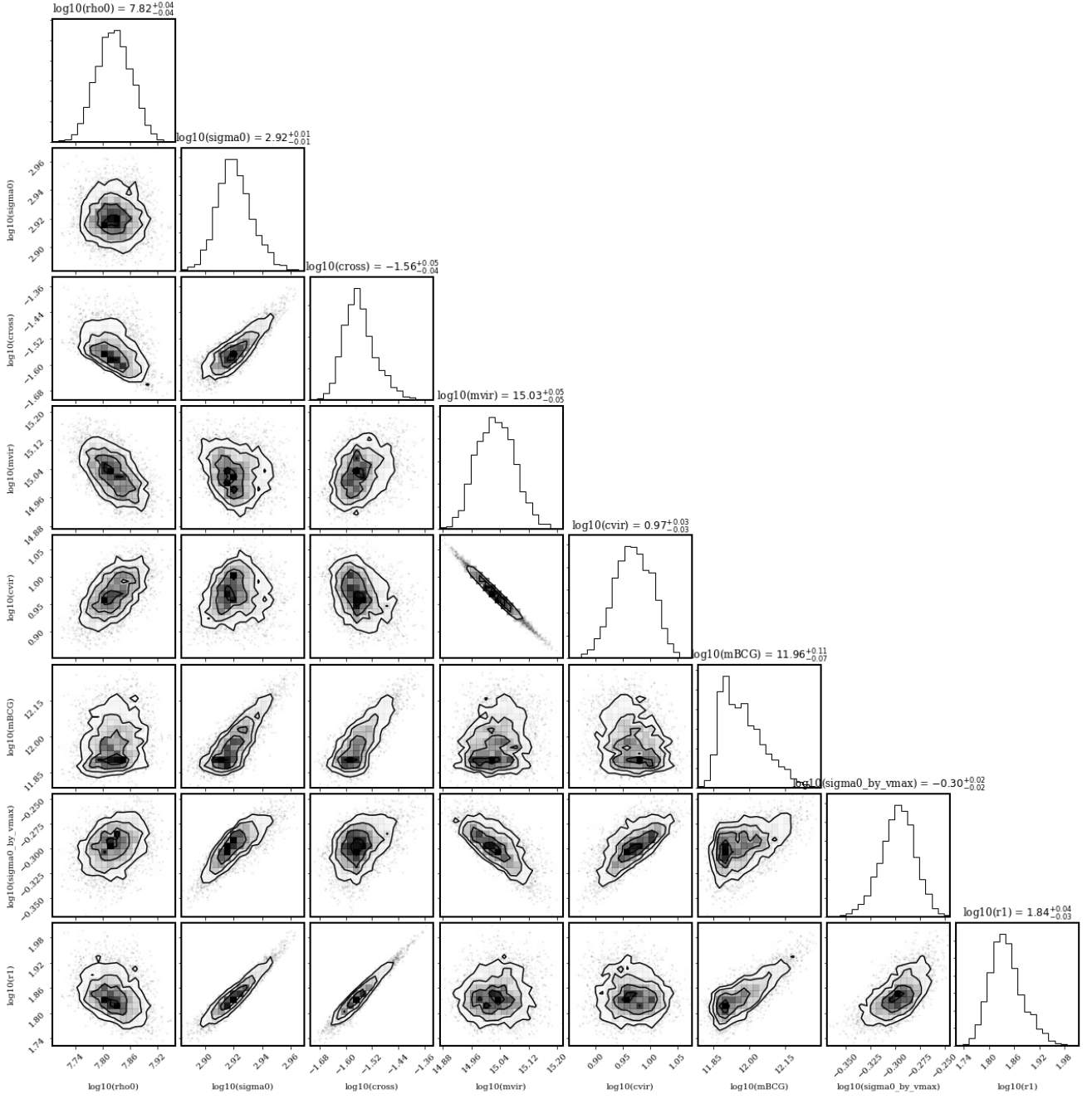
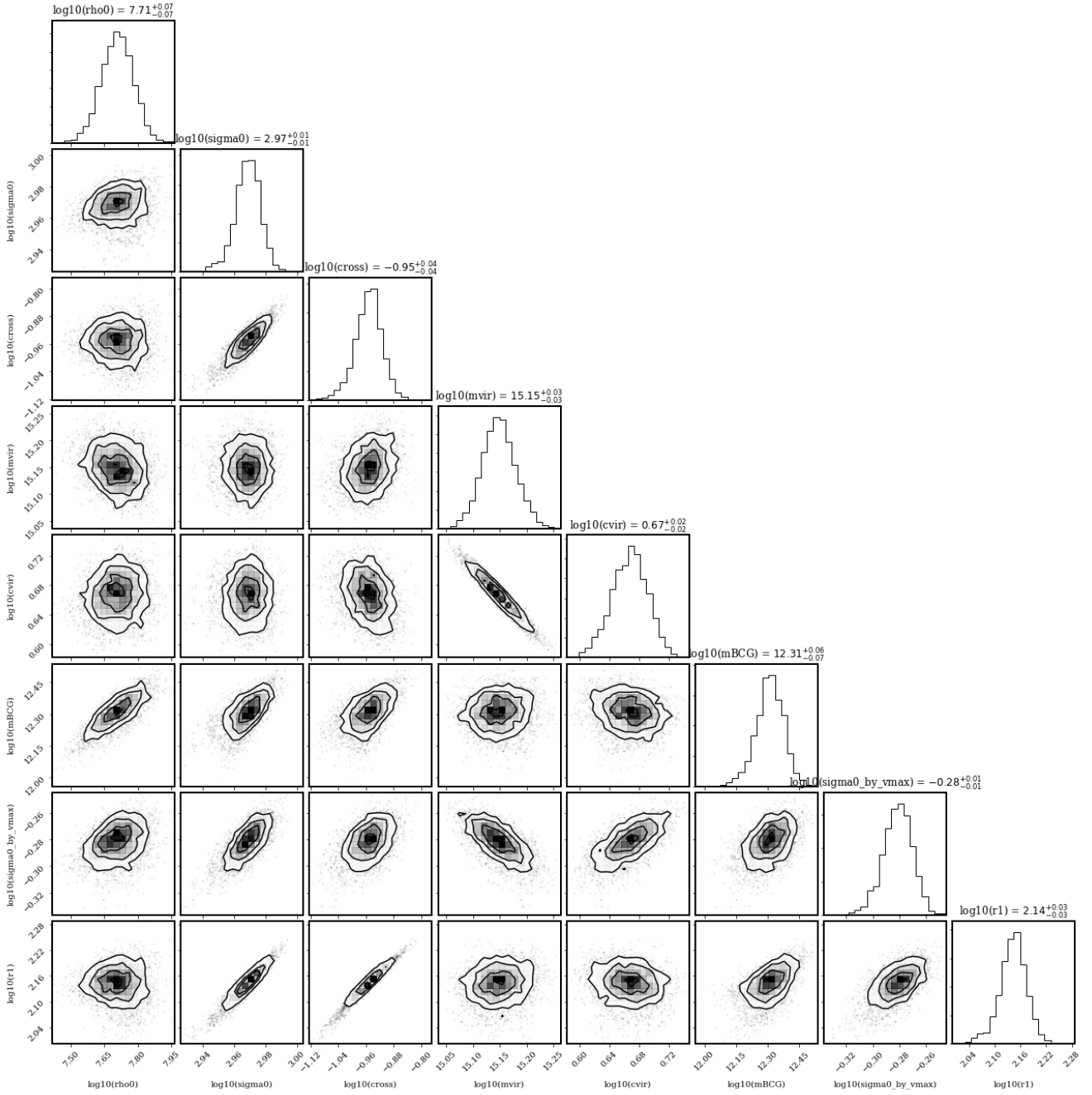
**Figure G5.** Abell 383 SIDM Halo Matching posteriors.

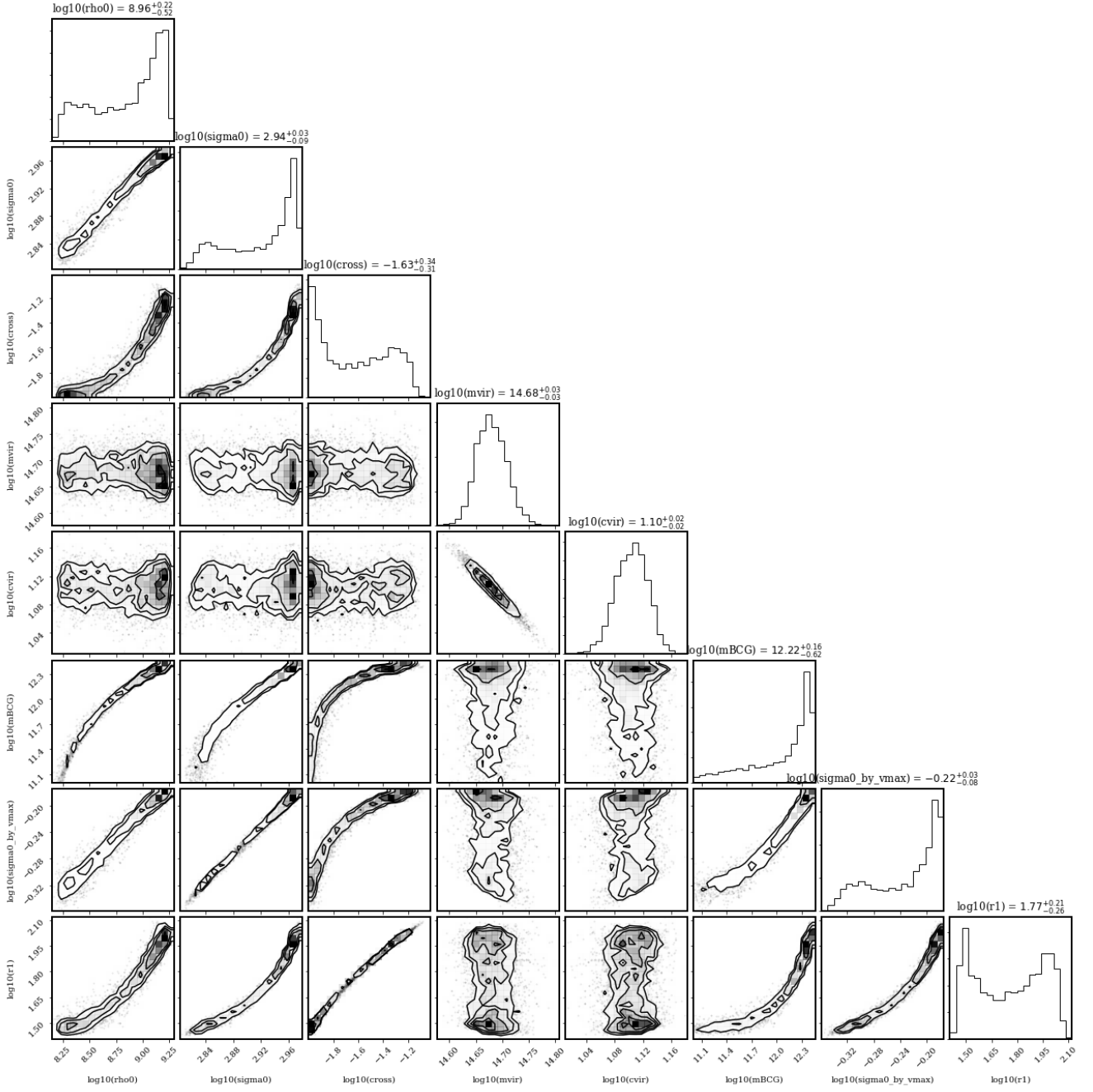


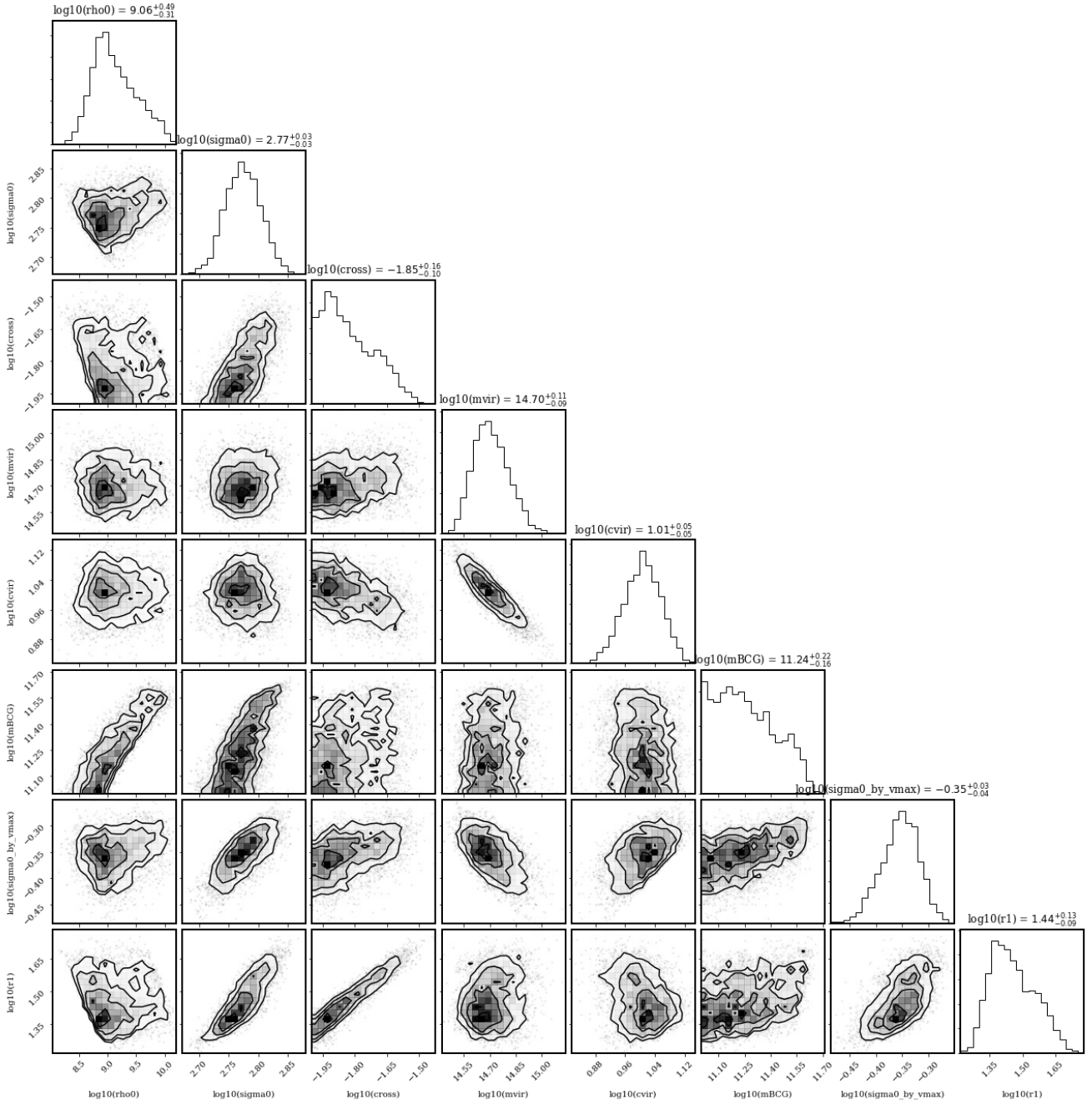
Figure G6. Abell 2261 SIDM Halo Matching posteriors.



**Figure G7.** MACS2129 SIDM Halo Matching posteriors.

**Figure G8.** MACS1720 SIDM Halo Matching posteriors.



**Figure G9.** Sim. Cluster 2 SIDM Halo Matching posteriors.

**Figure G10.** Sim. Cluster 3 SIDM Halo Matching posteriors.

